

Experimental and Numerical Investigations of Optimized High-Turning Supercritical Compressor Blades

by

Bo Song

Dissertation submitted to the Faculty of the
Virginia Polytechnic Institute and State University
in partial fulfillment of the requirements for the degree of

Doctor of Philosophy
in
Mechanical Engineering

Approved:

Dr. Wing F. Ng (Chair)
Dr. Clint L. Dancey
Dr. Joseph A. Schetz
Dr. Ricardo A. Burdisso
Dr. Thomas E. Diller
Dr. Walter F. O'Brien

November 2003
Blacksburg, Virginia

Key Words: Compressor, Optimized Blade, Controlled Diffusion Airfoil, Stator,
Cascade Testing, High-Turning, Supercritical Flow Condition,
Flow physics, Boundary Layer, Separation, Shock, Losses

Copyright by Bo Song 2003

Abstract

Experimental and Numerical Investigations of Optimized High-Turning Supercritical Compressor Blades

Bo Song
Mechanical Engineering Department
Virginia Tech

Cascade testing and flow analysis of three high-turning supercritical compressor blades were conducted. The blades were designed at an inlet Mach number (M_1) of 0.87 and inlet flow angle of 48.4° , with high camber angles of about 55° . The baseline blade was a conventional Controlled Diffusion Airfoil (CDA) design and the other two were optimized blades. The blades were tested for an inlet Mach number range from 0.61 to 0.95 and an inlet flow angle range from 44.4° to 50.4° , at high Reynolds numbers ($1.2\text{--}1.9 \times 10^6$ based on the blade chord). The test results have shown lower losses and better incidence robustness for the optimized blades at higher supercritical flow conditions ($M_1 > 0.83$). At the design condition, 30% loss reduction was achieved. The blade-to-blade flow was computed by solving the two-dimensional steady Navier-Stokes equations. Experimental results, in conjunction with the CFD flowfield characterization, revealed the loss reduction mechanism: severe boundary layer separation occurred on the suction surface of the baseline blade while no separation occurred for the optimized blades. Furthermore, whether the boundary layer was separated or not was found due to different shock patterns, different shock-boundary layer interactions and different pressure distributions on the blades. For the baseline blade, the strong passage shock coincided with the adverse pressure gradient due to the high blade front camber at 20% chord, leading to the flow separation. For the optimized blades, the high blade camber shifted to more downstream (30-40% chord), resulting in stronger flow leading edge acceleration, less strength of the passage shock near the blade surface, favorable pressure gradient right after the passage shock, thus no flow separation occurred. The flow understanding obtained by the current research can be used to guide the design of high-turning compressor blades at higher supercritical flow conditions.

Acknowledgements

First I would like to thank Dr. Wing F. Ng for being an excellent advisor through my academic and research efforts over the past four and a half years. His guidance and support helped me immensely towards the completion of this research. In addition, his professionalism has given me much stimulation that is helpful for my continuing career development. I would also like to thank Dr. Clint Dancey, Dr. Joseph Schetz, Dr. Ricardo Burdisso, Dr. Thomas Diller, and Dr. Walter O'Brien for serving on my advisory committee and their valuable advice on my thesis work. This project was sponsored by Honda R&D. Co. Cooperating with Dr. Toyotaka Sonada and Dr. Toshiyuki Arima at Honda in this project was fruitful. Their expertise and constructive comments on the research helped me further dig into the depth of the flow mechanisms. Their contribution of 3-D CFD investigation is also greatly appreciated.

It was my fortune working in a wonderful research group led by Dr. Ng. Since the first day I joined this group, I have obtained tremendous help from my colleagues and have enjoyed the team spirit. All the colleagues in the group deserve my gratitude. The important contributions made by Shiming Li, Justin Douglas, Xingmin Gui and Hans Raven in the preparation of the experimental setup and in the experiments expedited the completion of the experimental work. Besides his help in my research, I especially thank Todd Bailie for his mentoring and generosity during my incessant pursuit of better understanding American culture and refining my English. His integrity and gentlemanly behavior have earned my lifetime friendship. The help and friendship from other fellow graduate students are also appreciated: Andrew Nix, Austin Smith, Angie Rabe, Jason Anderson, Caser Carter, Jeff Kozak, Jinwei Feng, and Nikhil Rao. The friendship and support from the exemplary Chinese community of Blacksburg also made my study and life here much more enjoyable.

I received a lot of help directly and indirectly from the excellent researchers and engineers at Techsburg, Inc. Working with them was always a pleasure. During the wind tunnel facility modification, Stephen Guillot, Troy Jones and Greg Dudding made important contributions. The discussion with Stephen helped me not only in troubleshooting of the experiments, but also for establishing efficient engineering judgement. Sarah Stitzel helped me a lot in the CFD work by generating the computational grids for

me and teaching me how to use the CFD code and the post-processing software. Greg's expertise in precision machining made the fabrication of the angle probe possible, leading to the success of my design. All the help from these Techsburg folks are gratefully acknowledged.

A lot of machining work was required throughout this project, and most of the time it was needed in a hurry. With the great support from the technicians in the Mechanical Engineering and Aerospace and Ocean Engineering Machine Shops (Johnny Cox, Bill Songer, James Dowdy, Timothy Kessinger and Bruce Stanger), I always came out with everything ready in time. Their cooperation and help are appreciated. I would also like to thank Gary Stafford and Steve Edwards for maintaining the tunnel facility and helping me out when I had trouble with the tunnel operation. Thanks to Ben Poe and Jamie Archual for their excellent computer support and smiling faces.

The love from my family is an important motivation to me. My grandmother poured her boundless love into me until I was nine. She would have the broadest smile in heaven if she knew my present readiness for my degree. My love of science and engineering and sense of honor were instilled in childhood by my parents. I especially appreciate how well my mother understands me all the time. The cheering from my brothers for my every step of academic progress always encouraged me.

Finally, I would like to thank my wife, Hongxia Chen. Without her endless love, understanding, and support, I could not make my academic pursuit this far. In particular, while the birth of our first child brought me tremendous happiness and motivation, I did not have to reduce dedication to my research because Hongxia took care of the baby so well. My gratitude to my wife is truly beyond words.

Bo Song

*Virginia Polytechnic Institute and State University
November 2003*

Table of Contents

Abstract	ii
Acknowledgements	iii
Table of Contents.....	v
List of Figures	viii
List of Tables.....	xi
Nomenclature	xii
1. Introduction	1
1.1 Background	1
1.1.1 <i>Classification of Cascade Flows and Compressor Blades</i>	3
1.1.2 <i>Current Trend of Compressor Blades</i>	4
1.1.3 <i>Outline of the Current Project</i>	6
1.2 Previous Research	8
1.2.1 <i>Blade Optimization Techniques</i>	9
1.2.2 <i>Two Blade Development Programs for Optimized Blades</i>	12
1.2.3 <i>Cascade Testing and Cascade Flow Study</i>	14
1.2.4 <i>Controlled Diffusion Airfoil</i>	19
1.3 Objectives of the Current Work	22
2. Experimental and Numerical Methods	24
2.1 Cascade Wind Tunnel	24
2.1.1 <i>Flow Periodicity</i>	25
2.1.2 <i>AVDR Control</i>	28
2.2 Cascade Geometry	30
2.3 Instrumentation and Measurements.....	32
2.4 CFD Code	38
2.4.1 <i>Solution Procedure Sequence</i>	38
2.4.2 <i>Numerical Algorithms</i>	40
2.4.3 <i>Governing Equations</i>	44
2.5 CFD Procedure of the Current Work	45
2.5.1 <i>Computational Domain</i>	45

2.5.2 Code Input File	48
2.5.3 Code Boundary Data File	52
3. Results and Discussion	54
3.1 Cascade Performance and Flow Physics at the Design Condition	54
3.1.1 Experimental Results of Losses	54
3.1.2 Experimental Results of Pressure Ratio and Exit Flow Angle	55
3.1.3. Flow Mechanisms for the Loss Reduction.....	57
3.2 Cascade Performance and Flow Physics at the Design Inlet Flow Angle	71
3.2.1 Losses	71
3.2.2 Effect of Reynolds Number	74
3.2.3 Pressure Ratio and Exit Flow Angle.....	76
3.2.4 Blade Surface Mach Number and CFD Flowfield Contour.....	78
3.2.5 Double Shock Flow Phenomenon	92
3.3 Loss Robustness and Flow Structures at Off-Design Inlet Flow Angles	95
3.3.1 Loss Robustness.....	95
3.3.2 Blade Surface Mach Number at $\beta_1=45.4^\circ$	98
3.3.3 Flow Structures at Selected Off-Design Conditions	101
4. Conclusions	109
4.1 Cascade Performance Confirmation and Design Tool Validation	109
4.2 Flow Physics for High-Turning Supercritical Compressor Cascades	110
4.3 Design Philosophy for High-Turning Supercritical Compressor Cascades	110
4.4 Recommendations for Future Work	111
Appendix A Effect of AVDR	112
A.1 Introduction	112
A.1.1 Review of Previous Research.....	113
A.1.2 Motivations of the Study.....	115
A.2 Experimental and Numerical Methods	116
A.3 Results Discussion.....	116
A.3.1 Solid Sidewall Test.....	117
A.3.2 Slotted Sidewall Tests.....	118
A.3.3 Flow Behavior with the AVDR Effect.....	119
A.3.4 Blade Surface Mach Number.....	124
A.3.5 Summary with Additional Notes	127

A.4 Closure.....	131
Appendix B Angle Probe Design and Calibration	132
Appendix C Uncertainty Analysis.....	140
References	146
Vita	155

List of Figures

Figure 1	Compressor blade development trend.....	3
Figure 2	Flow patterns in modern compressor cascades	5
Figure 3	Outline of the current blade development program.....	7
Figure 4	Two new blade profiles optimized from the baseline	7
Figure 5	CDA aerodynamic design criteria	20
Figure 6	The Virginia Tech High Speed Cascade Wind Tunnel.....	25
Figure 7	Test section with measures to ensure flow periodicity.....	27
Figure 8	Cascade flow contraction and AVDR control	28
Figure 9	Cascade sidewall air bleed to control AVDR	29
Figure 10	Cascade geometry and nomenclature	31
Figure 11	Blade shape comparison	31
Figure 12	Side view of the cascade test section.....	32
Figure 13	Aerodynamic measurements for the cascade.....	33
Figure 14	Experimental investigation of loss mechanisms	35
Figure 15	Instrumented blades for surface pressure measurement	36
Figure 16	Experiments of blade surface oil flow visualization.....	37
Figure 17	Sequence of tasks of an ADPAC analysis	39
Figure 18	ADPAC single-block and multiple-block.....	41
Figure 19	H-O-H grid system and computational domain communication.....	42
Figure 20	Multi-grid mesh coarsening.....	43
Figure 21	The H-O-H grid system used in the current CFD work	46
Figure 22	The finer grid compared to the normal grid.....	47
Figure 23	Experimental losses at the design condition.....	55
Figure 24	Experimental static pressure ratios at the design condition.....	56
Figure 25	Experimental exit flow angles at the design condition	57
Figure 26	Experimental wake profiles at the design condition.....	58
Figure 27	Blade suction surface flow visualization at the design condition.....	59
Figure 28	CFD flowfield characterization at the design condition - ORG.....	61
Figure 29	CFD flowfield characterization at the design condition - ES	62
Figure 30	CFD flowfield characterization at the design condition - MOGA.....	63
Figure 31	Shock pattern at the design condition - ORG	65
Figure 32	Shock pattern at the design condition - ES.....	66

Figure 33 Shock pattern at the design condition - MOGA.....	67
Figure 34 CFD pressure and pressure gradient magnitude on the blade suction surface at the design condition	70
Figure 35 Loss development with inlet Mach number at the design inlet flow angle (48.4°).....	72
Figure 36 Comparison of experimental and CFD losses at the design inlet flow angle (48.4°).....	73
Figure 37 Effect of Reynolds number on compressor cascade losses [4]	74
Figure 38 Effect of Reynolds number on losses checked by CFD (48.4°).....	75
Figure 39 Static pressure ratio at the design inlet flow angle (48.4°).....	76
Figure 40 Exit flow angle at the design inlet flow angle (48.4°).....	77
Figure 41 Blade surface Mach number at design inlet flow angle - ORG	79
Figure 42 CFD flowfield characterization at design inlet flow angle (ORG $M_1=0.75$).....	80
Figure 43 CFD flowfield characterization at design inlet flow angle (ORG $M_1=0.84$).....	81
Figure 44 CFD flowfield characterization at design inlet flow angle (ORG $M_1=0.91$).....	82
Figure 45 Blade surface Mach number at design inlet flow angle - ES.....	84
Figure 46 Blade surface Mach number at design inlet flow angle - MOGA	85
Figure 47 CFD flowfield characterization at design inlet flow angle (ES $M_1=0.75$)	86
Figure 48 CFD flowfield characterization at design inlet flow angle (ES $M_1=0.91$)	87
Figure 49 CFD flowfield characterization at design inlet flow angle (ES $M_1=0.94$)	88
Figure 50 CFD flowfield characterization at design inlet flow angle (MOGA $M_1=0.68$) ..	89
Figure 51 CFD flowfield characterization at design inlet flow angle (MOGA $M_1=0.84$) ..	90
Figure 52 CFD flowfield characterization at design inlet flow angle (MOGA $M_1=0.95$) ..	91
Figure 53 Double shock phenomenon of ES – wake profile	93
Figure 54 Double shock phenomenon of ES – loss mechanism.....	93
Figure 55 Double shock phenomenon of ES – pressure gradient	94
Figure 56 Loss variation with inlet Flow Angle	96
Figure 57 Blade surface Mach number at $\beta_1=45.4^\circ$ - ORG.....	99
Figure 58 Blade surface Mach number at $\beta_1=45.4^\circ$ - ES	100
Figure 59 Blade surface Mach number at $\beta_1=45.4^\circ$ - MOGA	101
Figure 60 CFD flow structure at choke condition (ORG: $M_1=0.86$, $\beta_1=44.4^\circ$)	103
Figure 61 CFD flow structure at stall condition (ORG: $M_1=0.87$, $\beta_1=52.4^\circ$).....	104
Figure 62 CFD flow structure at choke condition (ES: $M_1=0.86$, $\beta_1=44.4^\circ$).....	105

Figure 63	CFD flow structure at stall condition (ES: $M_1=0.87$, $\beta_1=52.4^\circ$)	106
Figure 64	CFD flow structure at choke condition (MOGA: $M_1=0.83$, $\beta_1=44.4^\circ$).....	107
Figure 65	CFD flow structure at stall condition (MOGA: $M_1=0.87$, $\beta_1=52.4^\circ$).....	108
Figure A1	Flow contraction and AVDR control in cascade testing	112
Figure A2	Loss and AVDR development with inlet Mach number at the design inlet flow angle (48.4°).....	117
Figure A3	Loss variation with AVDR at the design condition	119
Figure A4	Blade suction surface flow visualization at the design condition	120
Figure A5	3-D CFD flow visualization at the design condition	121
Figure A6	Mach number contours at the design condition.....	122
Figure A7	Shadowgraphs at the design condition.....	123
Figure A8	Blade surface Mach number at design condition.....	125
Figure A9	Blade surface Mach number at lower inlet Mach number	129
Figure B1	Angle probe calibration setup	132
Figure B2	Conical angle probe design for outlet traverse measurement	133
Figure B3	Correlations for the prism probe	136
Figure B4	Correlations for the conical probe.....	137

List of Tables

Table 1	Classification of compressor blades/cascades	4
Table 2	Cascade Geometry	30
Table 3	Test Conditions and Experimental Uncertainty	35
Table 4	One Input File Used in the Numerical Study	49
Table 5	One Convergence File obtained in the Numerical Study	51
Table 6	One Boundary Data File Used in the Numerical Study	53
Table 7	Summary of incidence robustness	97
Table 8	Achieved inlet Mach numbers at the choke flow conditions	98
Table C1	Uncertainty of instruments and equipments	140
Table C2	Instrumentation uncertainty range	144
Table C3	Aperiodicity uncertainty range	144

Nomenclature

AVDR	Axial velocity density ratio
C	Blade chord
CDA	Controlled diffusion airfoil
ES	Name of the first optimized blade (profile generated by evolutionary strategy)
I	Incidence angle
M	Mach number
MOGA	Name of the second optimized blade (profile generated by multi-objective genetic algorithm)
ORG	Name of the baseline blade (original blade profile)
P.S.	Pressure surface
P _s	Static pressure
P _t	Total pressure
R	Gas constant
S.S.	Suction surface
S	Cascade pitch
T _t	Total temperature
T _u	Free stream turbulence intensity
V	Flow velocity
X	Distance in axial direction
β	Flow angle with respect to the axial direction
δ	Uncertainty deviation
ε	Isotropic turbulent kinetic energy dissipation rate
κ	Turbulent energy
γ	Cascade stagger angle
φ	Blade camber angle
ρ	Density
$\sigma = C/S$	Cascade solidity
ω	Total pressure loss coefficient

ΔP_t (P_{td}) Total pressure difference = $P_{t1} - P_{t2}$

Subscript

1 Cascade inlet
2 Cascade outlet
amb Ambient
is Isentropic process
s Blade surface

1. Introduction

Section 1.1 of this chapter describes the background for the current work, including the classification and development trend of compressor blades, followed by the outline of the research project. Previous research is reviewed in Section 1.2. The objectives of the current work are described in Section 1.3.

1.1 Background

Gas turbine engine manufacturers are constantly competing to produce more efficient, higher thrust, and lighter engines. Correspondingly, the research and development of the turbomachinery components is directed for higher efficiency, higher power output and less weight. To achieve these goals, improvement in compressor blade design is essential. Generating qualified blade profiles is a prerequisite to developing high-performance compressors.

The basic function of the blades is to turn the air to the required angle. Along this process, undesired loss (entropy generation) results. Therefore, the goal of the blade design is to achieve the desired flow turning with minimum losses, within the constraint of geometric orientation of the blade row required by the overall compressor design. Unlike an isolated airfoil for external flow application, blades of a turbomachine (including compressor and turbine) are used in a row and referred to as a “cascade” in the research. Definition for the cascade and the cascade nomenclature description can be found in the references [1, 2, 3].

The aerodynamic performance of a compressor cascade is basically determined by five quantities as listed below. For more detailed information, refers to [4].

- The shape of the blades
- Cascade stagger angle (γ)
- Cascade solidity ($\sigma = C/S$)
- Inlet flow angle (β_1)
- Inlet flow Mach number (M_1)

During the blade inverse design process, all the above quantities are chosen from the overall compressor design requirement, except for the blade shape. While it is the design goal to generate blades which meet the geometrical and flow turning requirements of the compressor, of equal importance is how much losses are generated. Unlike a turbine cascade through which the flow is accelerated, the adverse pressure gradient due to the flow diffusion in a compressor cascade imposes unfavorable force on the boundary layer. Correspondingly, it is more difficult to achieve a thinner boundary layer and/or control the boundary layer from separation, which is the major factor determining the aerodynamic losses of the blades. In particular, when the flow speed is elevated such that transonic flow is formed in the blade passage, shock loss is introduced; and the shock-boundary layer interaction makes it more difficult to control the boundary layer development. Therefore, the primary design challenge for a compressor blade is to generate a blade shape with losses as low as possible.

Along with the rapid progress of Computational Fluid Dynamics (CFD) and computer techniques, turbomachinery blade design has been developed from empirical methods to computational methods. The later methods, representative of the modern blade design, allow the blade designer to be more innovative and to design beyond the limits of experimental data. In the design process, optimization of the target pressure and velocity distribution along the blade passage is fulfilled with taking into account the required performance and loss mechanisms. After that, blade shapes are determined using numerous inverse blade design methods, ranging from two-dimensional blade cross sections to the full three-dimensional definition of blade channels. A good overview of the inverse blade design methods can be found in [5]. With the development of compressor blade design, blade performance has been increasingly improved with the blade shapes becoming more sophisticated, from the first generation Circular-Arc Profile, the second generation Controlled Diffusion Airfoil (CDA), to the current optimized blades. Figure 1 shows this blade development trend. (One of three blades in the current study is a CDA, and the other two are optimized blades.)



Figure 1 Compressor blade development trend

After the blades have been designed, their aerodynamic performances need to be tested in a cascade wind tunnel before compressor rig tests, and subsequent consideration to be used in a compressor. The important role of the two-dimensional linear cascade wind tunnel testing in turbomachinery research and development can be summarized into the following aspects:

- Experimentally evaluate blade performances
- Confirm blade design, verify design/optimization tools
- Validate flow solvers
- Study the blade-to-blade flow (flow physics)

For a newly designed blade, cascade testing provides experimental data to confirm its aerodynamic performance. The study of the associated flow physics is of significant interest as it can be used to further improve the blade design. As advocated by Denton [6] and emphasized again by Dunham [7] several years later, physical understanding of the flow, particularly the loss mechanisms, is essential for turbomachinery development. Therefore, a complete turbomachinery blade development process can be summarized as a three-step procedure: design (optimization) - cascade wind tunnel testing (validation) - flow physics study (understanding).

1.1.1 Classification of Cascade Flows and Compressor Blades

Compressor blades are developed for broad applications on turbomachines, for either rotors or stators, at different flow conditions (including flow speed and flow angle).

Thus, there is a large family of compressor blades, in service and under research. To better understand the literature in relation to the current study, the classification of compressor blades is necessary information to be provided. One way to categorize the blades is based the flow speeds at the cascade inlet and exit as well as in the blade passage. Such a classification of cascade flows, including compressor and turbine, was given by Starke and Lichtfuss [8] and Starke [9]. Accordingly, “subsonic blade”, “transonic blade”, and “supersonic blade” are frequently seen in literature. In parallel, the blades can also be called as “rotor blade” and “stator blade” depending on application to a rotors or stator, or “high-turning blade” and “low-turning blade” based on the blade camber angle/flow turning. In summary, a categorization of compressor blades can be simply made as shown in Table 1.

Table 1 Classification of compressor blades/cascades

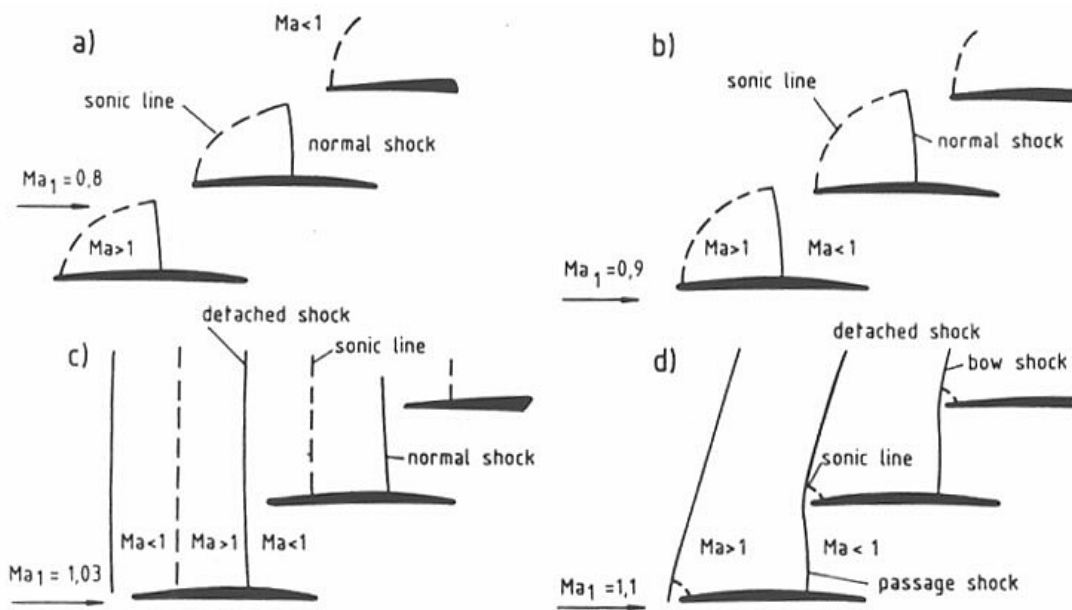
Category	Inlet	Passage	Exit	Application
I	Subsonic	Subsonic	Subsonic	Rotor, Stator
II*	Subsonic	Transonic	Subsonic	Rotor, Stator
III	Supersonic	Transonic	Subsonic	Rotor
IV	Supersonic	Transonic	Supersonic	Rotor
		Rotor	Stator	Note
Flow turning/Blade camber	Low	High	Normally, but not necessary	

* Usually referred to as supercritical flow conditions

1.1.2 Current Trend of Compressor Blades

The development trend of modern axial flow compressors is marked by higher pressure ratio and less weight, which require reducing the number of stages and increasing aerodynamic blade loading [10]. Consequently, flow velocities relative to the blades have been raised, leading to transonic and supersonic speeds for rotor blades and supercritical flow conditions for stator blades. A schematic of the flow patterns at these

conditions is shown in Figure 2 (from Dunker [11]). At supercritical flow conditions (normally $M_1=0.6-1.0$, may also be called as high-subsonic inlet flow speeds), as usually encountered on compressor stator blades (Figure 2: a and b), local flow in the blade passage accelerates beyond sonic speed although inlet flow remains within the subsonic range. The supersonic patch occurring in the blade front portion is usually terminated by a normal passage shock. Besides the elevated flow speed, the other design requirement for modern stator blades is high flow turning.



Note: (a) and (b) are supercritical flow conditions

Figure 2 Flow patterns in modern compressor cascades

Therefore, realizing high flow turning at supercritical flow conditions, while keeping losses as low as possible, becomes the design challenge for modern stator blades. The desired design is straightforward when one considers the origin of the blade profile losses, namely the viscous losses (including the loss generated in the boundary layer and in the downstream wake) and shock loss. Thus, the key is to control the boundary layer to be as thin as possible and free of separation whenever possible, while avoiding shock generation or at least lessening shock strength and shock/boundary layer interaction. As will be reviewed later, this key idea was well substantiated by the development of CDA,

but only proved to be working well for inlet Mach numbers up to 0.8. Above this Mach number (referred to as “higher supercritical flow conditions” in the thesis), losses increased abruptly. The reason is: with increasing flow speeds and flow turning, the boundary layer separation seems inevitable. Even at an intermediate inlet Mach number of 0.79, a high solidity ($\sigma=2.2$) compressor cascade (designed by US Air Force) had boundary layer separated due to the high flow turning (the blade had a high camber angle of 69°), thus necessitating additional flow control techniques to reduce losses and increase flow turning [12]. Therefore, to achieve high flow turning at higher supercritical flow conditions turns out to be a great challenge for the stator blade design.

1.1.3 Outline of the Current Project

Under the above mentioned background, a joint research program was initiated with the cooperation between Honda R&D. Co. Ltd. and Virginia Tech to develop advanced compressor blades for application to a stator hub section. The design condition is listed as below:

- Inlet Mach number $M_1=0.87$
- Inlet flow angle $\beta_1=48.4^\circ$
- Flow turning $\Delta\beta=(\beta_2-\beta_1)=48.4^\circ$
- Cascade solidity $\sigma=2$

To achieve the high flow turning while maintaining low losses at this critical design condition is a challenge for the blade design. As demonstrated and will be shown later in the thesis, a 2nd generation CDA cannot be used in this case. Two new blades were designed using advanced optimization methods by Honda with the CDA as the baseline. The three blades were tested in the Virginia Tech High Speed Cascade Wind Tunnel. Experimental and numerical investigations of the associated flow physics was conducted as well. Thus, a complete three-step blade development program has been completed. An outline of this joint blade development program is shown in Figure 3. The last two steps composed the current Ph.D. thesis work.

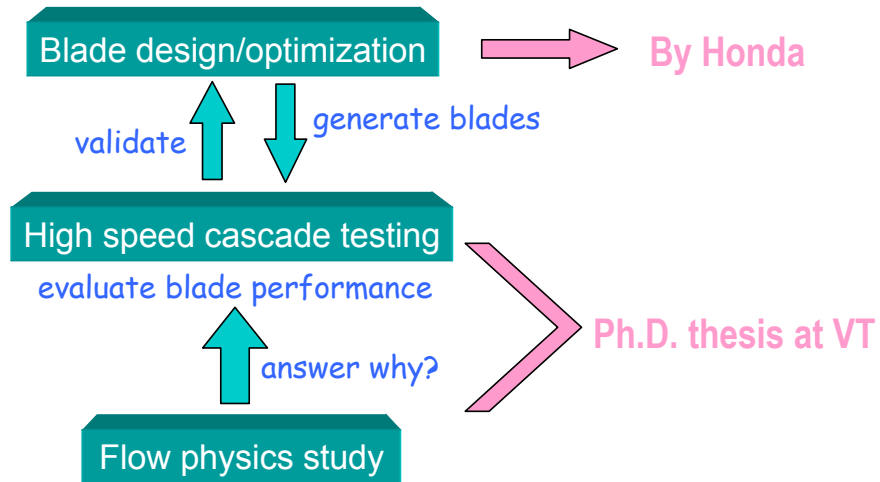


Figure 3 Outline of the current blade development program

Although it is out of the scope of the thesis work, the blade design/optimization performed by Honda was the first step of the joint three-step blade development program. As background information of the thesis work, the blade design/optimization is briefed herein. To replace an originally used CDA blade profile, two new blade profiles were generated using optimization methods of Evolution Strategy (ES) and Multi Objective Genetic Algorithm (MOGA), as shown in Figure 4. Accordingly, the three blades were named ORG, ES, and MOGA respectively in the thesis.

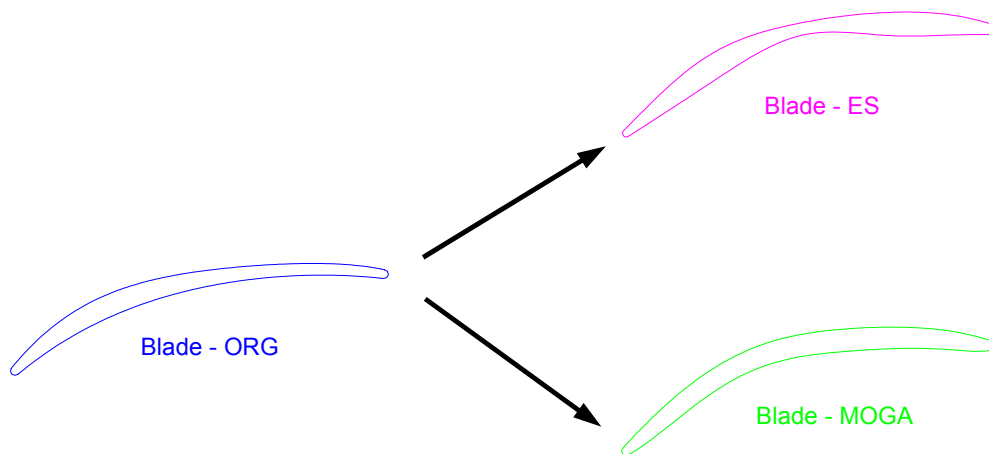


Figure 4 Two new blade profiles optimized from the baseline

The optimizing process for Blade ES involved characterizing the airfoil, applying an optimization algorithm, and solving the blade-to-blade flow. The optimization objective was set to minimize total pressure losses at the design condition with deviation angle and geometrical constraints. An evolution strategy (ES) was adopted for the optimization, with derandomized cumulative step-size adaptation to reduce the population size and to speed up convergence. Detailed information about the ES optimization methodology was provided by Olhofer et al. [13]. The blade-to-blade flowfield was computed by solving the two-dimensional steady Reynolds-Averaged Navier-Stokes (RANS) equations. The equations were normalized in a generalized curvilinear coordinate system to fit the blade surface. To complete the system of governing equations, the Reynolds stress tensor was evaluated using the Bussinesq eddy viscosity model. The governing equations were solved using an implicit time-marching finite-difference scheme to obtain a steady-state solution. In order to speed up convergence to a steady state solution, the spatially varying time-stepping technique was employed. For additional information about the Navier-Stokes solver, refer to Arima et al. [14]. Using the same flow solver, Blade MOGA was generated with Multi-Objective Genetic Algorithm. The objective functions included minimization of total pressure loss coefficient and deviation angle with taking into account the incidence-robustness. Detailed description of the blade optimization for Blade MOGA was given by Yamaguchi and Arima [15].

1.2 Previous Research

There is a large volume of literature on compressor cascade testing and the study of compressor cascade flow. However, the blades documented in the literature differed from one research to another (different blade shapes, different cascade geometry), and were designed at different flow conditions (flow speed and flow angle) for different applications (rotor or stator, mid-span section or near-hub/tip section). As such, comparing the blade performances from one research to another is inappropriate in a rigorous sense, except for those designed in one research program and intended for comparison among themselves. For example, the three cascades in the current work have

the same cascade geometry, design condition, and application. They only differ in blade shape. In that sense they are comparable in a rigorous sense.

After an extensive literature search, the author only found some previous studies which are partially related to the current work. The following review of previous research is primarily intended to show the research background and trend in the area. Whenever a previous work has some comparable aspects to the current work, the relevance is discussed, either in this section or Chapter 3 Results and Discussion.

1.2.1 Blade Optimization Techniques

Along with the maturation of computational fluid dynamics (CFD) and the advancement of optimization techniques, blade optimization seems rather promising to improve cascade performance and thus becomes very popular. A lot of work has been published in recent years, for both compressor and turbine cascades. Below just list a few to show the role and status of this blade design technique. It should be noted that these researches are not directly related to the thesis work but the first step work (by Honda). The intention of this review is to show the optimized blades studied in the thesis work represent the prevailing trend of turbomachinery blade research and development.

Benini and Toffolo [16] presented a multi-objective optimization method for designing cascade for subsonic compressors, using evolutionary algorithm and a blade-to-blade inviscid/viscous solver, with the aim to maximize the pressure ratio and to minimize the profile losses. Xu and Amano [17] proposed a blade design and optimization procedure for both compressor and turbine blade design, and showed both the airfoil shape optimization and the three-dimensional optimization could improve the performance of turbomachinery blades. Rai and Madavan [18] investigated the feasibility of applying artificial networks to the aerodynamic design of turbomachinery airfoils. The design process included defining a target pressure distribution, computing the flow, and training the neural network to find a design that is closest to the target. Yiu and Zangenech [19] successfully applied an automatic optimization algorithm to redesign two generic high speed industrial centrifugal compressors. Two methods of parameterizing the circulation distribution were examined. Both of them provided smooth loading distribution and hence were practical tools for design.

Oksuz et al. [20] developed a new methodology to find the optimal aerodynamic performance of a turbine cascade. They linked a boundary layer Euler method and a genetic algorithm within an automated optimization loop. The maximum blade loading was achieved for a higher flow turning, a wider pitch, and a thicker cascade. Manna and Tuccillo [21] applied an optimization procedure to the aero-thermal design of high performance turbomachinery cascades. The method was demonstrated to have not only the excellence of the initial design, but also the possibility of enhanced blade overall efficiency. Papila and Shyy [22] developed a methodology to improve the supersonic turbine performance. A global optimization framework combining the radial-basis neural network and polynomial response surface method was constructed. Shape optimization applied to the first vane and blade of a supersonic turbine. Dennis et al. [23] developed an aerodynamic shape-design optimization algorithm that utilized a Navier-Stokes flowfield analysis code and a constrained microgenetic optimizer and a sequential-quadratic-programming optimizer for enforcement of certain constraints, with the objective of minimizing total pressure loss. Significant reduction of the total pressure loss was achieved using this method for a supersonic axial turbine cascade.

Catalano and Dadone [24, 25] proposed a strategy for the robust and efficient inverse design of turbomachinery blades at transonic flow conditions. The proposed methodology was tested on the inverse design of two-dimensional turbine blades and a three-dimensional turbine nozzle. Shahpar [26] presented an approach to three-dimensional design of turbomachinery blades. A few heuristic and gradient-based optimizers were used in conjunction with a linear sensitivity analysis tool, to re-design a turbine nozzle guide vane. The study showed that nonlinear complicated cost functions could be reduced significantly and aerodynamic and geometrical constraints could be handled efficiently. This paper also included good literature review on aerodynamic shape optimization for both external and internal flows (wings and turbomachinery blades). Manna and Tuccillo [27] developed an optimization strategy for decelerating cascades, using a Navier-Stokes flow solver, correlation functions and a gradient-based optimization method. The objective was to determine the geometrical characteristics of the cascade of the best aerodynamic performances and to define appropriate cost function

in a more general case. The method was applied to C4 blade profiles, which demonstrated the validity and potential of the methodology.

Lee and Kim [28] presented a numerical optimization technique combined with a three-dimensional thin-layer Navier-Stokes solver, to find the optimum shape of a stator blade in an axial compressor through calculations of single stage rotor-stator flow. Li et al. [29] optimized cascade airfoils using Genetic Algorithms. For turbine cascade inverse design, they used Genetic Algorithm with single objective based on Boltzmann selection. For compressor cascade airfoil design, multiobjective Genetic Algorithm was used. The goal was to seek higher pressure rise and lower total pressure loss on the basis of Controlled Diffusion Airfoil (CDA). Horibata [30] presented a cascade airfoil design method based on Navier-Stokes equations. The design variables included camber line, thickness distribution, stagger angle and outlet static pressure. The objective function was defined to take into account the total pressure loss, outlet flow angle deviation and inlet flow Mach number deviation. Medic et al. [31] applied an optimal shape design methodology to turbomachinery flows. The methodology was characterized by an unstructured flow solver, automatic differentiation of programs for the computation of gradient and a CAD-free framework for shape and mesh deformation. Jha et al. [32] developed a multidisciplinary optimization procedure for the design of turbine profiles. Both aerodynamic and heat transfer design objectives were integrated with blade geometric constraints, to minimize total pressure and exit kinetic energy losses. Nerurkar et al. [33] presented a turbomachinery blade design method using parametric optimization techniques coupled with CFD Euler analysis. The blade geometry was sought to minimize total pressure loss and match pressure loading.

There was more work published on blade optimization. A complete review of them is neither intended nor necessary in this dissertation. But the general idea can be summarized as the following. The blade is designed using various blade optimization techniques, which are basically composed of optimization algorithms coupled with solving the equations governing the flowfield. The objective is to obtain optimum aerodynamic performance of the blades with geometric and aerodynamic constraints. The flowfield is characterized by solving Euler equations or Navier-Stokes equations, from incompressible flow to compressible flow, from two-dimensional flow to three-

dimensional flow. It is seen that modern flow solvers capable of computing complex turbomachinery flow is playing an essential role in blade optimization. It is also noticed the published blade optimization work mostly focused on the development of the blade optimization tools/procedures. Experimental confirmation of the performances of obtained optimized blades, however, has been hardly seen. Only two exemplary programs involving all the three steps were found from open literature. They are reviewed below.

1.2.2 Two Blade Development Programs for Optimized Blades

An excellent three-step program to develop high performance compressor blades was published by Köller et al. [34] and Küsters et al. [35]. The blades were designed at subsonic speeds ($M_1=0.44-0.72$) for low flow turning ($10^\circ-18^\circ$). The solidity (σ) of the test cascades was in a medium range of 1.05-1.17. The influence of high Reynolds numbers ($0.7-2.7 \times 10^6$) compared to aeroengine compressors were taken into account in this blade development program. The design process involved combined use of a geometric code for the airfoil description, a blade-to-blade solver and a numerical optimization algorithm. The optimization was aimed at a wide low loss incidence range. For some characteristic members of the new airfoil series, extensive cascade testing was conducted to confirm the design goal of low losses, and to substantiate the reliability of the design process and the flow solver. Experimental results including surface Mach number distribution, total pressure losses, flow turning, and static pressure rise for the entire incidence range were presented. Moreover, boundary layer development was investigated using surface flow visualization, which led to more insight into the flow behavior. With the experimental confirmation of the superior performances of the optimized blades and the study of the associated flow physics, this research showcased the efficiency of the automated blade design/optimization tool and the advantage of blade optimization techniques. This work is closely related the current research, in terms of the research procedure and objective, as well as the high Reynolds number range. But the current research deals with higher inlet Mach numbers and higher flow turning.

Another good example of the three-step blade development program was published recently by Sonada et al. [36] and Schreiber et al. [37]. In their program, high-turning compressor airfoils were designed using modern blade optimization methods, for

application at a low Reynolds number condition (1.3×10^5). The cascades were designed at a subsonic Mach number of 0.6 with a relatively high solidity of 1.73, to achieve a flow turning of 44° . With a CDA design as the baseline, two new blade profiles were generated using numerical optimization methods of Evolution Strategy (ES) and Multi-Objective Genetic Algorithm (MOGA). The objective of the optimization was to minimize total pressure losses and deviation angles. The optimization process included the representation of the blade geometry, the generation of a computational grid, and the blade-to-blade flow analysis solving Navier-Stokes equations. The aerodynamic performances of the two new optimized blades and the conventional CDA were extensively investigated in the cascade wind tunnel of German Aerospace Center (also known as DLR). The associated flow physics were studied by additional experimental and numerical investigations. Both experimental and numerical results confirmed that the two optimization methods were able to reduce the total pressure losses at the design condition and to increase the low loss incidence range in the positive direction by about $2-3^\circ$. Therefore, the reliability of the design/optimization tool and the applied flow solver was proved. This work also demonstrated the advantage and promise of automated blade optimization techniques.

The research by Sonada is also closely related to the current thesis work in terms of the research procedure and objective, as well as dealing with high turning blades. But due to different application of the blades, the research by Sonada dealt with lower Mach number and lower Reynolds number in comparison with the current work. Therefore, the current research will complement the three-step blade development programs with investigating high-turning optimized blades at higher supercritical flow conditions. It should be also pointed out that the optimized blades in the current work were designed using the same optimization methods (ES and MOGA) and Navier-Stokes solver as used in Sonada's research. Although the optimization tools were validated for designing high-turning compressor blades at lower speeds and Reynolds numbers [36, 37], the achieved success there showed prospect of the application of the blade optimization tools to the current blades. This will be clarified in this thesis work.

1.2.3 Cascade Testing and Cascade Flow Study

Besides the above reviewed related previous work which involved the first step or the complete three steps of a new blade development, most of the previous research found from open literature dealt with the last two steps: cascade testing and cascade flow physics study. This is directly related to the thesis work in terms of the research approach and objective (both dealt with the last two steps). However, due to the reasons pointed out at the beginning of Section 1.2, the relevance between the previous research and the thesis work is limited. This section only reviewed selected previous work, with two intentions. One is to cover the related work. The other is to show the research status and trends through scanning some typical previous work, to orient readers where the current thesis work stands in relation to the literature.

Research on Rotor Blades

In compressors, stator blades normally operate at lower flow speeds than rotor (including fan) blades; thus stator blades are usually designed at subsonic inlet Mach numbers (not into higher supercritical flow conditions) while the corresponding rotor blades have reached supercritical flow conditions, or even higher to transonic and supersonic range. At higher flow speeds, the blade design is much more challenging due to the increasing difficulty to control boundary layer and the generation of shock waves, as well as the effect of the latter on the former. As such, research interest was directed to rotor blades conventionally, leading to the great majority of published work.

Weber et al. [38] carried out numerical and experimental investigation of a compressor cascade at supercritical flow conditions. The cascade was designed for a compressor rotor section with the design inlet Mach number of 0.85 and flow turning of 20° . The code used a two-dimensional finite element method to solve the full potential equations. Viscous effect was considered by using McNally's integral boundary layer method with additional procedures for laminar and turbulent separation and shock boundary layer interaction. Cascade tests were performed over the whole incidence range. Numerical and experimental results reached reasonable agreement except the discrepancy remaining in the supersonic region. At the design incidence, no shock occurred on the blade suction surface, thus leading to very low losses. This is noticed as a good

achievement for low losses at higher supercritical flow conditions, but it was only demonstrated on low-turning blades. At both positive and negative incidences, losses were highly elevated due to the appearance of the shock and the shock-induced boundary layer separation. Thus the superior performance of this supercritical cascade is limited due to its poor incidence robustness.

Schreiber and Starcken [39] performed an intensive experimental analysis on a transonic compressor rotor cascade, in order to elucidate the flow behavior and determine the performance in the whole operating range. The design relative inlet Mach number was 1.09 and the flow turning was 12.5° . Experiments were conducted for an inlet Mach number range from 0.8 to 1.1 and inlet flow angles from choking to stalling flow condition. Axial Velocity Density Ratio (AVDR) was controlled by endwall suction during the tests. The experiments provided detailed information about shock location, shock losses, blade surface pressure distributions, and overall performance. The total pressure loss data obtained from the cascade tests agreed well with those obtained behind the corresponding blade element of the transonic compressor rotor, thus underlining the applicability of the cascade experiment in the design and flow analysis of axial flow turbomachines.

Schreiber and Starcken [40] investigated the flow phenomena and loss mechanism of a strong shock wave-turbulent boundary layer interaction in a supersonic compressor cascade. The cascade geometry was typical for a transonic fan tip section operating at a relative inlet Mach number of 1.5, a flow turning of about 3° , and a static pressure ratio of 2.15. In the cascade tests, Reynolds number based on the blade chord was as high as 2.7×10^6 . A lot of experimental results were presented, including cascade overall performance, blade surface pressure distributions, Schlieren photographs, and blade surface visualization. The results showed a strong boundary layer separation on the blade suction surface occurred due to a complicated shock pattern and its interaction with the boundary layer: a detached bow shock in front of the leading edge, a quasi-normal shock and a leading oblique shock on the suction surface interacting with the boundary layer by a lambda shock system. The research also revealed different shock boundary layer interaction from that obtained in earlier experiments on flat plates, demonstrating the

necessity of cascade flow analysis for turbomachinery flow study. More experimental results of this research were presented by Schreiber [41].

Similar experimental investigation was conducted by Tweedt et al. [42] for another supersonic compressor cascade. The cascade was derived from the near-tip section of a high-through-flow axial flow compressor rotor with a design relative inlet Mach number of 1.61. The blade had a negative camber angle of -2.89° . Cascade tests were performed for an inlet Mach number range from 1.30 to 1.71, with blade chord Reynolds number in the range 1.1×10^6 to 1.4×10^6 . Endwall boundary layer suction was used to reduce secondary flow effects and to control axial velocity density ratio (AVDR). The shock wave pattern in the entrance region was measured using a laser anemometer, which demonstrated that the unique-incidence condition was well predicted by an approximate method. The influence of static pressure ratio (back pressure) and AVDR on the blade performance was experimentally investigated. The application of an empirical correlation to separate the effects of these two parameters was discussed.

Research on Stator Blades

While there are so many publications on rotor blades, very few has been found for stator blades due to the reason addressed before, although this is more related to the thesis work. Two researches dealing with stator blades (thus for high flow turning) are found. They are reviewed below.

Hoheisel and Seyb [43] presented a theoretical and experimental investigation of the boundary layer and loss behavior on a high turning Double Circular Airfoil (DCA) compressor cascade. The cascade was designed to achieve flow turning of 50° at an inlet Mach number of 0.85. The blade had a high camber of 56.8° and the cascade had a high solidity of 2.2. The experiments were carried out in the high speed cascade wind tunnel of DLR. A time marching method was used to predict the blade pressure distribution, coupled with a boundary layer integral method to predict the boundary layer integral parameters and the total pressure losses. Extensive experimental data was obtained to check theoretical blade design methods. It was shown that a good agreement between the measured and predicted values was achieved for the minimum-loss incidence condition and the flow choking and boundary layer separation were well predicted. It is seen this

cascade had the closest geometry and design condition compared to the cascades of the current work. The results showed that this 1st generation blade kept low losses up to $M_1=0.8$; after that losses rose up abruptly. The shown loss bucket at $M_1=0.8$ indicted a narrow low-loss incidence range. The design challenge of a high-turning, high-solidity compressor cascade at higher supersonic flow conditions has been clearly shown from Hoheisel's work. Although there is still some difference (but not much) in the cascade geometries and design conditions between Hoheisel's cascade and the cascades of the current work, it can be reasonably speculated that 1st generation circular-arc blades would not meet the requirement of the current blade design. This is why the current blade designer (Honda) chose a 2nd generation CDA as the design baseline.

Another experimental work was presented by Katoh et al. [44], involving compressor tests and the corresponding cascade testing. The compressor test showed that lower losses were achieved when replacing the original NACA-65 stator blades with supercritical CDAs. The two-dimensional cascade testing was performed on the blade profiles (NACA-65 and CDA) designed for the near-hub section of two compressor stators. The design condition was: inlet Mach number 0.8, flow turning 11° , Reynolds number 5.79×10^5 , AVDR 1.07. The cascade had a solidity of 0.93. Experiments in the cascade wind tunnel provided detailed blade performance information, such as blade surface velocity distribution, total pressure losses, and the boundary layer behavior (using hot-film), which revealed the loss reduction from NACA-65 to CDA was due to the elimination of the shock waves on the blade suction surface. More efforts were exercised to further improve the performance of the CDA blade by re-designing the CDA. Cascade test results showed wider low loss incidence range and lower losses were obtained on the re-designed CDA blade. Although the compressor test with the re-designed blade was not performed again, the authors pointed out the possible improvement in the compressor performance with using the new CDA stator. This research provides an example to directly showcase the importance and necessity of two-dimensional cascade wind tunnel testing in turbomachinery research and development. It also substantiated the superiority of the 2nd generation CDA to the 1st generation NACA airfoil. Nevertheless, low losses were only achieved at $M_1=0.8$ in Katoh's research, although the flow turning was low.

Numerical Work

Besides cascade wind tunnel testing and experimental investigation of cascade flow physics, numerical methods were also widely used by researchers to study flow behaviors of turbomachines, helping better understand cascade aerodynamics. With the progress of computational fluid dynamics (CFD), cascade flow has been solved with increasing accuracy, although the quantitative discrepancy from experimental results still exists. Compared to experimental methods, numerical methods are advantageous in terms of much less cost/time consumption and the capability to provide full and detailed flowfield information. Therefore, CFD flow analysis was also employed in the current thesis work to complement the experimental investigation. The status of the application of modern CFD methods to compressor cascade flow studies can be seen from the following review of selected previous numerical work.

Küsters and Schreiber [45] successfully applied a two-dimensional multiblock Navier-Stokes solver to a supersonic compressor cascade flow with strong shock wave/boundary layer interaction. The cascade was typical of a fan blade section with precompression design, low flow turning, and static pressure ratio around 2.0. A very fine computation grid was used to guarantee sufficient resolution of the supersonic/transonic flowfield with a complex wave pattern and shock induced boundary layer separation. Investigations were conducted at inlet Mach number between 1.28 and 1.53 with Reynolds number of 2.6×10^6 . The results were compared with previous cascade wind tunnel testing data. It was shown that the flow solver provided an accurate resolution of the complex shock wave pattern in front of and in the blade passage. The shock/boundary layer interaction was adequately simulated by a one-equation turbulence model (the current study used one-equation model as well). Overall losses were predicted well. Only a deficit existed in simulating the wake mixing process, where the code under-predicted the flow entrainment process (the current study had this under-prediction as well). In general, the good agreement between the numerical and experimental results demonstrated that the code was a capable tool to support experimental investigation and analysis of complex transonic flow, and it was useful in performing design and parameter studies.

A Navier-Stokes calculation procedure was also applied by Shamroth et al. [46] to high Reynolds number flow through subsonic compressor cascades, using the mixing length turbulence model. Comparisons of the results with existing experimental data showed good predictions of pressure distribution and boundary layer velocity profiles with small degree of quantitative discrepancy. Calvert [47] developed an inviscid-viscous interaction treatment to predict the blade-to-blade flow in axial compressors operating at supersonic inlet flow conditions with a normal shock at the blade passage inlet. The dependence of the shock loss on the shock/boundary layer interaction, found from using the viscous model and inviscid model, indicated the inferiority of the inviscid model. Comparison with experimental results showed general agreement except for some boundary layer thickness discrepancy.

The prediction of loss by CFD is usually a major concern. König et al. [48,49] presented improved blade profile loss models for modern transonic axial flow compressors. Both the models for subsonic and supersonic flows were treated. In conjunction, the subsonic and supersonic correlations achieved a continuous transition of the loss curves from subsonic to supersonic inlet conditions. The comparison of the computed values with the measured data demonstrated the correctness of the prediction for shock loss, viscous loss, and wake mixing loss. Although some quantitative discrepancy was observed on the results of the loss variation with inlet Mach number or incidence, CFD results were good enough to show trends and for relative evaluation.

These previous numerical work on compressor cascade flow suggests that modern CFD techniques are very helpful to support the research, but a numerical simulation of the flow without any defect, particularly at high speeds, is still an over-expectation. Noting this point is necessary to view the CFD results of the current work in the right perspective.

1.2.4 Controlled Diffusion Airfoil

As the baseline blade of the current study is a controlled diffusion airfoil (CDA), some background information and previous work on CDA are provided in this section.

CDA appeared in the early 1980s with the need of and growing interest in supercritical compressor blades. The benchmark research on CDA was probably due to

Hobbs and Weingold [50]. In this reference, the aerodynamic design criteria for CDA with supercritical flow conditions were illustrated. As shown in Figure 5 (from Hobbs and Weingold [50]), the normal passage shock (see also Figure 2: a) is avoided on the suction surface due to the refined blade shape design. No shock-induced boundary layer separation occurs; instead, a smooth diffusion process beginning from the peak velocity lasts all the way to the trailing edge, although the local velocity goes quite above the sonic speed. Consequently, low losses and increased incidence range are obtained on CDA blades.

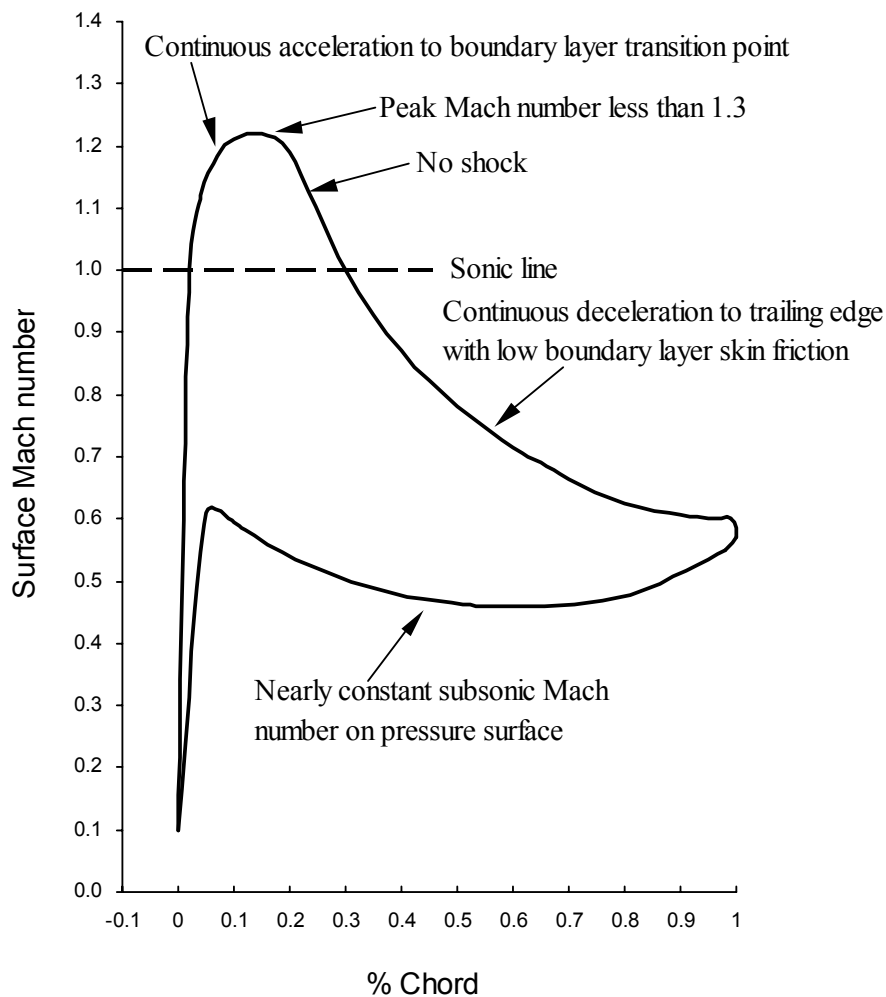


Figure 5 CDA aerodynamic design criteria

Hobbs and Weingold [50] successfully developed a series of CDAs for multistage compressor application. The cascades were designed with an inlet Mach number of 0.7, inlet flow angle of 30° , flow turning 13.6° , AVDR 1.07, and solidity of 0.933. Cascade test results demonstrated the lower losses and wider low-loss incidence range of the CDAs than conventional NACA-series airfoils and Multiple Circular Arc (MCA) airfoils. In addition, single and multistage rig tests showed high efficiency, high loading capability, and ease of stage matching. The shock-free and separation-free design concept for CDAs had been proved by the work of Hobbs and Weingold. Behlke [51] extended the basic CDA philosophy to the endwall flow region and developed new CDAs for multistage compressors. Using an Integrated Core/Endwall Vortex design model, the author produced a new full-span optimized controlled diffusion design. Extensive cascade, low-speed, large-scale, and high Mach number compressor rig tests were carried out. The results showed a 1.5% increase in efficiency and 30% increase in surge-free operation compared to original CDAs designed by Hobbs and Weingold.

Due to the superior aerodynamic performance, CDA aroused considerable research interest around the world. Steinert et al. [52] designed a CDA cascade ($M_1=0.62$, $\beta_2-\beta_1=26.4^\circ$, $\sigma=1.47$). The cascade wind tunnel test confirmed very low losses of the blade due to optimum suction surface velocity distribution (leading to separation-free operation). Later on, Steinert and Starcken [53] published their investigation on the boundary layer transition and separation behavior of that CDA blade, thus revealing the embedded flow physics for the blade's aerodynamic performances. Dunker et al. [54] redesigned the stator of an existing transonic axial compressor stage using the controlled diffusion concept. The design conditions of the cascades were $M_1=0.57-0.68$, $\beta_2-\beta_1=37.4-43.4^\circ$. They performed stage testing which demonstrated that the new airfoils operated efficiently under three-dimensional turbomachinery conditions, indicating the two-dimensional approach was promising for three-dimensional blade design.

Sanger [55] designed a controlled diffusion stator using a series of computational analysis methods coupled by a numerical optimization procedure. The midspan section of the stator was experimentally evaluated in a cascade ($\sigma=1.67$, blade camber= 41.1°) [56]. The cascade test data was used for the design/optimization validation. The cascade

testing was conducted in a low speed wind tunnel, with inlet Mach numbers ($M_1=0.2$) much less than the design level ($M_1=0.68$), but realistic Reynolds numbers were ensured through large-scale blading. Later on, similar to the work of Steinert et al. [53], the flow in the cascade was mapped by Elazar and Shreeve [57] using two-component Laser-Doppler Velocimetry (LDV) to characterize the boundary layer behavior. Shreeve et al. [58] continued LDV surveys in the near wake region of the cascade. Comparison with the pressure probe and hot-wire data indicated good agreement, providing an unusual test case for viscous code calculations and an improved understanding of the flow.

All the above work is noticed to study CDAs at normal supercritical flow conditions ($M_1 < 0.8$) or even with low subsonic cascade tests. Although it was indicated in the CDA design criteria that the peak surface Mach number should not be beyond 1.3 (corresponding to a specific upper limit of M_1), no detail information is available from open literature of CDAs at higher supercritical flow conditions, as required on the CDA of the current work.

1.3 Objectives of the Current Work

This thesis work contributes to the last two steps of the blade development program: experimental confirmation of the blade performances and the study of the associated flow physics.

First, cascade testing was conducted to evaluate the blade performances at the critical design condition ($M_1=0.87$, $\beta_1=48.4^\circ$, $\Delta\beta=48.4^\circ$), including the total pressure losses, flow turning, and static pressure rise. The test results are used to confirm the blade design and validate the blade optimization tools. Additional cascade tests were performed at selected off-design conditions to better compare the performances of the three blades, i.e., to answering which blade is better and how much difference in the blade performances at off-design conditions.

After the aerodynamic performances of the blades were determined, experimental and numerical investigations were further performed to reveal the associated flow physics, particularly the loss mechanisms. Flow diagnostic techniques such as blade surface pressure measurement, blade surface oil flow visualization, and shadowgraph were used in the experiments to study the pressure/velocity distribution, shock pattern, boundary

layer behavior. In parallel, a 2-D Navier-Stokes flow solver was applied to characterize the blade-to-blade flow, to support elucidating the flow phenomena. This third step of work will be of not only academic interest in the area of compressor cascade aerodynamics, but also valuable feedback to the blade design methodology.

The baseline blade is a conventional CDA. Although many previous studies on CDAs have been seen from published literature, none of them involved flow analysis for higher supercritical flow conditions ($M_1 > 0.8$), especially for high flow turning. The only knowledge from previous research was that there was an upper surface Mach number limit (1.3) for the conventional CDAs to keep low losses. Detailed flow analysis on the high-turning CDA at higher supercritical flow conditions by the current work will lead to broader and deeper understanding of the flow, answering why the good performance of the CDA cannot be extended to higher Mach numbers.

As the other two blades are newly designed by optimization, any flow analysis associated with them will be of interest. In particular, if the blade optimization was demonstrated to be a success, i.e., low losses were achieved on the optimized blades at higher supercritical flow conditions, considerable interest would be placed on the low-loss mechanism. Understanding of it will help improve the design philosophy for modern compressor stator blades.

2. Experimental and Numerical Methods

This chapter describes the experimental and numerical methods used in the current study. All the experiments were performed in the Virginia Tech High Speed Cascade Wind Tunnel. Description of the tunnel facility is given in Section 2.1, the geometry and parameter of the tested cascades in Section 2.2, the instrumentation and measurement techniques in Section 2.3. Numerical work was fulfilled using an available CFD code, ADPAC. Basic information of the code is provided in Section 2.4, while Section 2.5 describes the application of the code to the current study.

2.1 Cascade Wind Tunnel

The Virginia Tech High Speed Cascade Wind Tunnel, as schematically shown in Figure 6, was a blowdown type, with the capacity to sustain high speed flow for approximately 15 seconds. High pressure air, supplied by a four-stage reciprocating compressor, upon discharge from the storage tanks, passed through an activated-aluminum dryer for dehumidification and then proceeded through the inlet section of the tunnel, where a flow straightener and a screen were set to make the flow uniform. Upstream of the test section, a turbulence grid was inserted to increase inlet flow free stream turbulence level (Tu) to 1.2%-1.6%. Details of the grid design and tests were described by Douglas [59]. Without the grid, the turbulence level was found only about 0.1%. The turbulence intensity increase obtained from the use of the grid caused significant loss change at some flow conditions [60]. Thus, considering the elevated Tu better represented the realistic blade application environment on the turbomachine, all the experiments of the current work were conducted with the grid in use.

When the flow entered the test section, it was turned with large angles by the tested cascade. After that, the flow was guided by the exhaust passage and finally discharged into the ambient. A multistage centrifugal blower standing beside the tunnel was used to provide bottom wall suction in the test section to adjust cascade inlet flow uniformity/periodicity (will be detailed later). The choke plate inserted in the exhaust section was employed to change the static pressure in the test section for sidewall air bleed (will be detailed later). For each blowdown tunnel run, the cascade inlet total

pressure was maintained by a feedback control scheme to obtain the desired inlet Mach number.

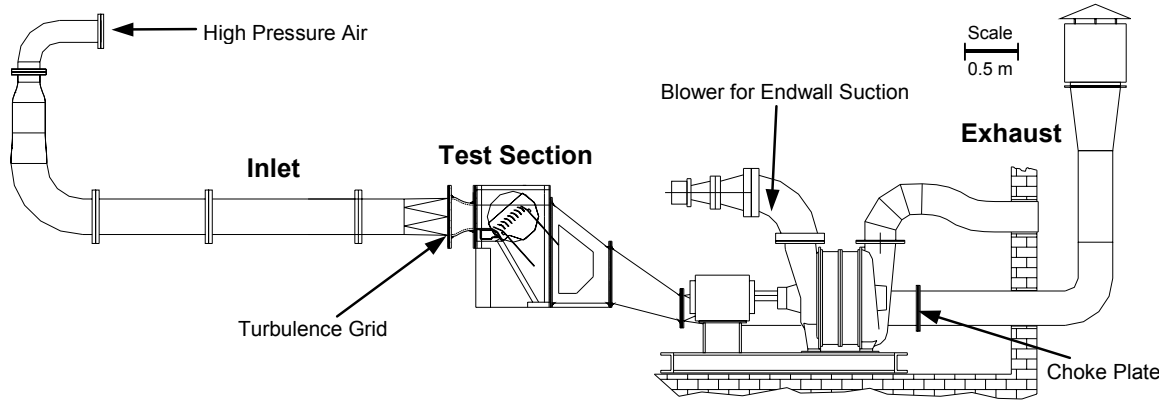


Figure 6 The Virginia Tech High Speed Cascade Wind Tunnel

2.1.1 Flow Periodicity

Flow periodicity is one of the prerequisites for two-dimensional linear cascade testing quality, as the cascade model is set to simulate the inherently periodic flow of a turbomachine [1]. Given the limited size of the tunnel and a limited number of blades constituting the cascade, special care should be exercised in the cascade wind tunnel testing to achieve acceptable flow periodicity, thus ensure test quality. Starcken and Lichtfuss [8] discussed this issue and made comments on the corresponding solutions in general. A detailed review on cascade testing facility and instrumentation by Starcken et al. [61] is another good reference, which covers the issue of flow periodicity for subsonic, transonic, and supersonic conditions. Researchers in the German Aerospace Center achieved satisfactory flow periodicity in the cascade tests by applying endwall suction and using tailboards, throttles, etc. [39, 52, 62]. Deutsch and Zierke [63] obtained good periodic flow using endwall suction in combination with tailboards in their cascade testing of a DCA compressor cascade with a high camber of 65° . Recently, Lepicovsky et al. [64] studied flow periodicity in their transonic cascade, indicating tailboards had strong influence on the flow periodicity.

In the current investigation, guide vanes, tailboards and bottom wall suction were employed to achieve reasonably good flow periodicity. As shown in Figure 7, a pair of tailboards were added to the cascade exit. They are both 47 cm in length. In addition, a pair of guide vanes were placed at the top and bottom side of the cascade. The guide vanes were arc-shaped with the same thickness as the tailboards. The guide vanes and the tailboards were deployed such that the tailboards were in the direction of the tangent lines of the guide vanes at the joints, where the tailboards and guide vanes touched each other. The two tailboards were set parallel to each other and in the direction of the design outlet flow angle, instead of blade outlet metal angle, as can be observed in Figure 7. Tailboards and guide vanes were always used together to proper boundary conditions to achieve periodic cascade flow.

Bottom wall suction, as shown in Figure 7, was employed to further improve flow periodicity whenever needed. Preliminary tests showed that for higher inlet Mach numbers, tailboards and guide vanes were not sufficient to exclude the influence of the bottom wall boundary layer. By adding bottom wall suction, the thickened bottom boundary layer was removed, thus improving the inlet flow condition for the cascade. Bottom wall suction was provided by the blower as shown in Figure 6. A suction block was mounted at the bottom side of the cascade inlet (see Figure 7). The cross section of the cascade inlet has the dimension of 15.2 cm (width) \times 23.5 cm (height). The block was designed to have slots on the surface to the cascade and a cavity in the middle so that suction could be implemented. During operation, the suction rate could be adjusted by the regulation valves placed on the piping between the suction block and the blower. In the experiments, optimum suction rate was determined by trial and error until pitchwise distribution of inlet static pressure looked became as uniform/periodic as possible.

Detailed description of the experiments and results about the flow periodicity was given by Song et al. [65]. This reference also included detailed discussion on the effects of guide vanes, tailboards and bottom wall suction and comments on improving flow periodicity for high speed high turning compressor cascade testing.

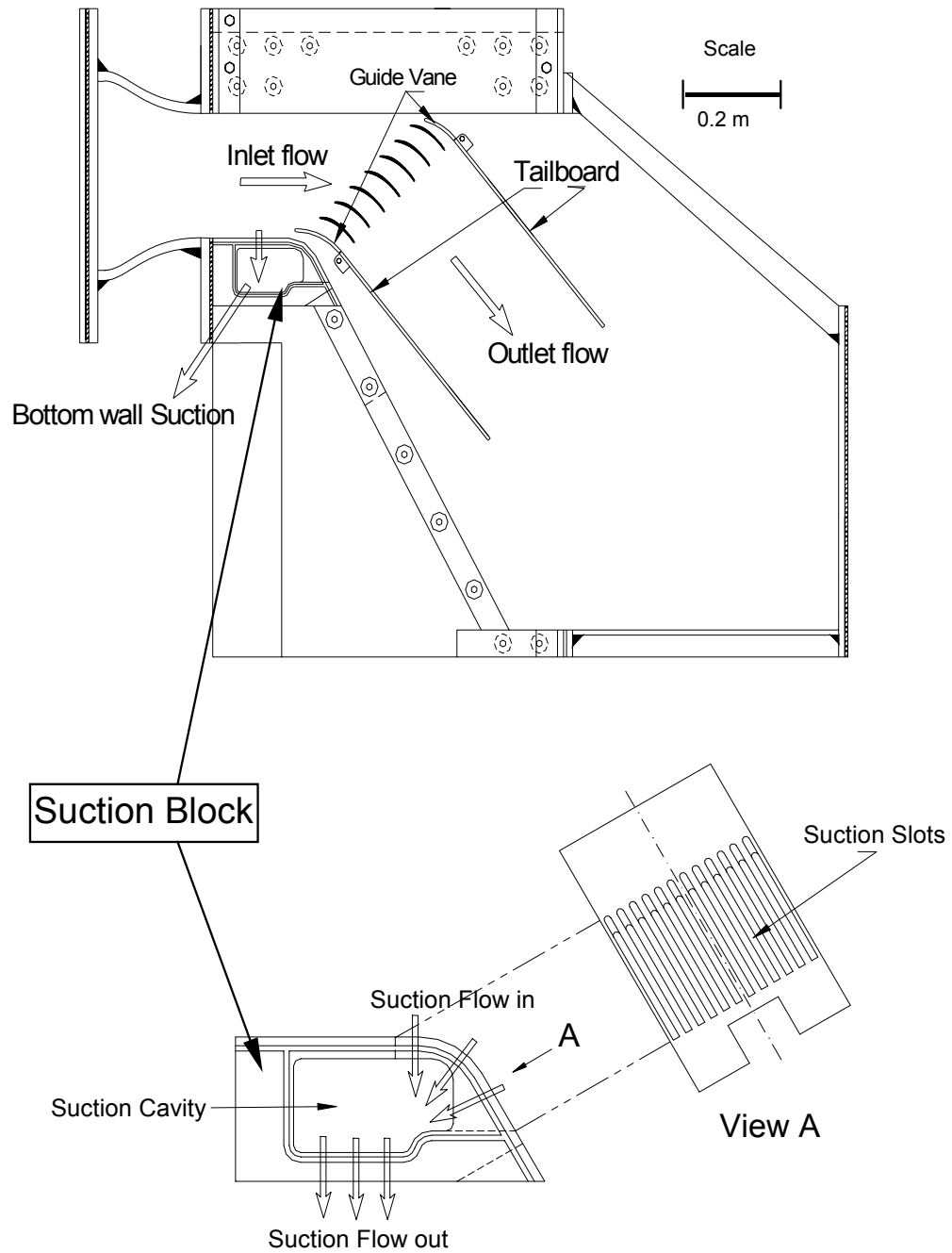


Figure 7 Test section with measures to ensure flow periodicity

2.1.2 AVDR Control

Another important issue in two-dimensional linear cascade testing is the effect of AVDR (axial velocity density ratio). A schematic to show the cascade flow contraction and the corresponding AVDR control is given in Figure 8.

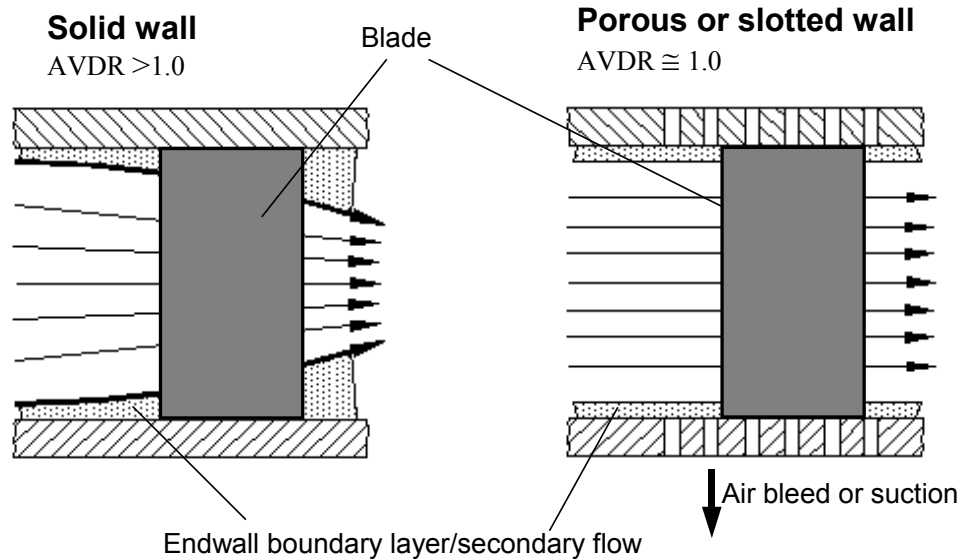


Figure 8 Cascade flow contraction and AVDR control

AVDR is defined as

$$AVDR = \frac{\int_0^{2 \text{ pitch}} \rho_2 \cdot V_2 \cdot \cos \beta_2 \cdot ds_2}{\int_0^{2 \text{ pitch}} \rho_1 \cdot V_1 \cdot \cos \beta_1 \cdot ds_1} \quad \text{(Equation 1)}$$

In this research, AVDR was calculated using Equation 1 with the measured corresponding flow parameters. In an ideal two-dimensional linear cascade flow, AVDR is unity. However, in cascade testing, the AVDR value determined from the measured aerodynamic parameters in the midspan plane is usually greater than unity due to the contraction of the flow across the cascade. The flow contraction results from the sidewall boundary layer thickening and/or the sidewall secondary flow. To some extent, AVDR represents the contraction ratio of the flow. The higher value of AVDR means the flow contracts to a higher degree. To control AVDR, porous or slotted walls have been widely used, whereby some amount of air was removed by either bleed or suction.

Previous research has shown that AVDR has significant influence on the cascade flow and hence the blade performance. Therefore, its effect has to be taken into consideration in the cascade tests. It would be incontrovertible if AVDR could be ideally controlled to the desired value, e.g., the data obtained for comparison were under the equal value of AVDR. However, this is not always attainable due to the facility limitation. Therefore, what makes more practical sense is to get valid data and reach correct conclusions from the cascade tests despite the existing AVDR influence. What specific strategies the cascade experimentalists should take depend on their facility capacity, objectives of the experiments, and the flow conditions. This issue, for its significant value in cascade wind tunnel research, is discussed in detail in Appendix A.

AVDR control in the current work was achieved using the following method. Slotted sidewalls were used in addition to solid sidewalls. The slots were made in the rear part of the cascade passages, open to the ambient for air bleed, as shown in Figure 9. With the choke plates of different internal diameters inserted in the exhaust section of the tunnel (see Figure 6), static pressure was adjusted in the cascade while inlet Mach number was maintained the same. Consequently, different bleed air rates could be obtained, resulting in different AVDR values. Testing with solid sidewalls provided data at another different AVDR value. As such, the effect of AVDR on the blade performance could be experimentally evaluated.

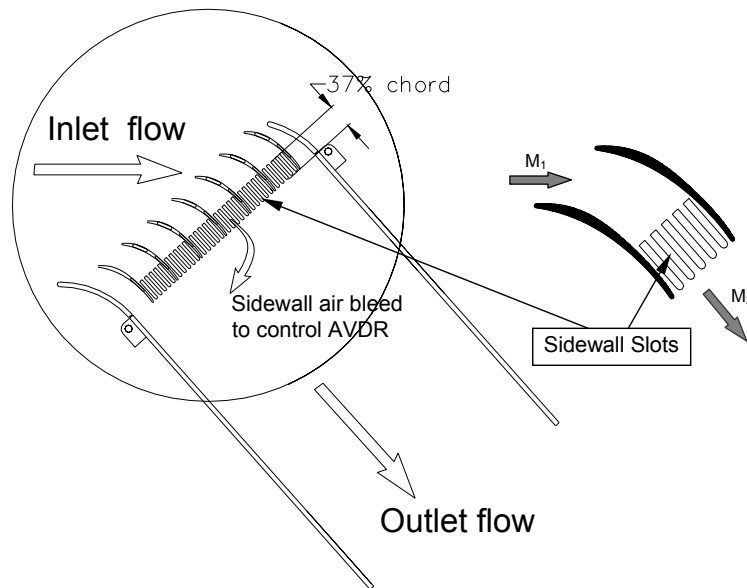


Figure 9 Cascade sidewall air bleed to control AVDR

2.2 Cascade Geometry

The three blades tested in this research, ORG, ES and MOGA, have similar cascade geometry (chord, aspect ratio, solidity, stagger angle, and camber angle), but differ in blade shape. The geometric parameters of the cascades are listed in Table 2. The cascade nomenclature used in this research is illustrated in Figure 10. The shape comparison of the three blades is given in Figure 11. It can be seen that the blades are highly cambered and have close spacing, as they are designed for the stator hub section. More specifically, the highest camber of each blade appears at different locations, about 30% chord for ORG and around mid-chord for both ES and MOGA. While the two optimized blades having the same overall turning characteristics, they differ significantly in shape. ES has the very thin portion around mid-chord, while MOGA has much more uniform thickness along chord. How different are the cascade performances from these three different blade shapes and the underlying flow physics will be revealed by the current research.

Table 2 Cascade Geometry

Blade Chord (C)		86 mm
Aspect ratio		1.77
Solidity ($\sigma=C/S$)		2
Blade number		7
Stagger Angle (γ)	ORG	15°
	ES	16°
	MOGA	16°
Camber Angle (φ)	ORG	55°
	ES	56°
	MOGA	54°

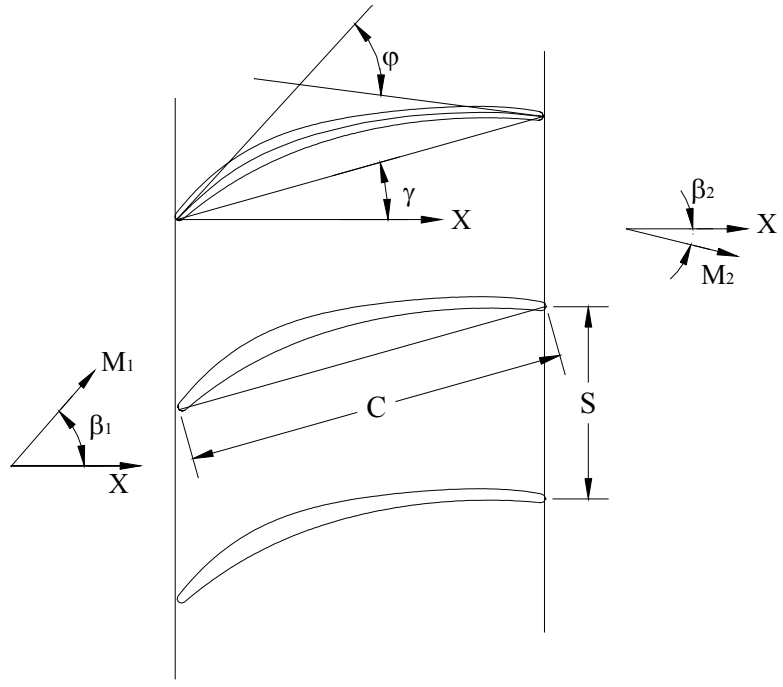


Figure 10 Cascade geometry and nomenclature

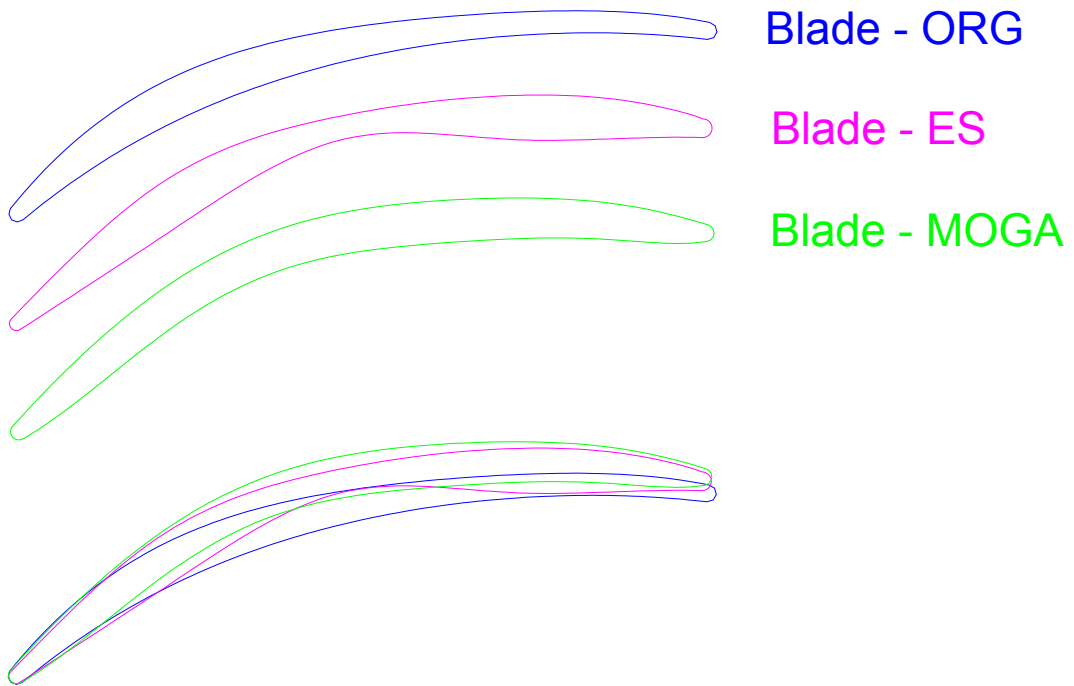


Figure 11 Blade shape comparison

2.3 Instrumentation and Measurements

The cascade test section, as shown in Figure 12, was fully instrumented for aerodynamic measurements to determine the flow condition for each tunnel run and the blade performance. In addition, flow diagnostic experiments were conducted to understand the associated flow physics.

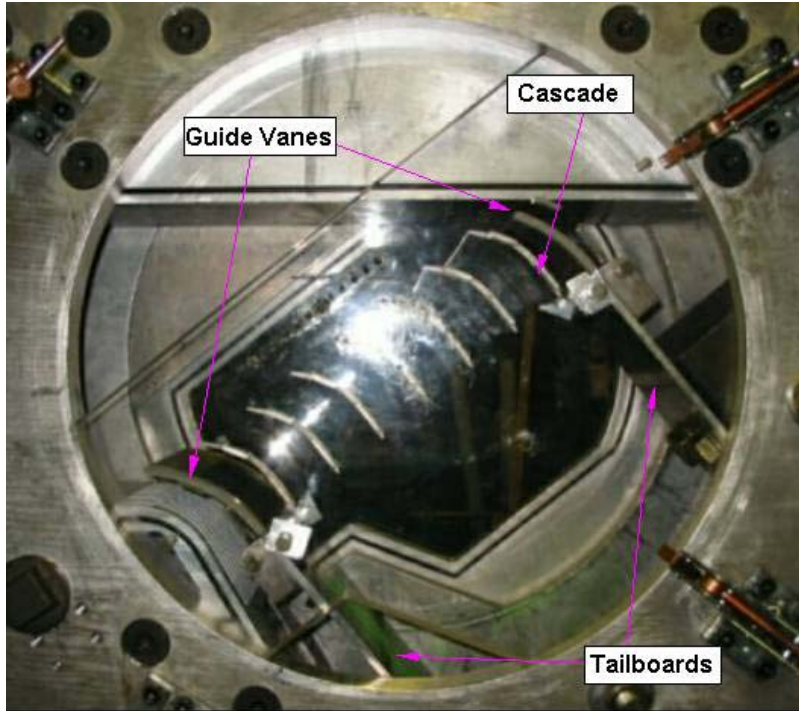


Figure 12 Side view of the cascade test section

Aerodynamic measurements in the experiments, as shown in Figure 13, included inlet total temperature (T_{t1}), inlet total pressure (P_{t1})/static pressure (P_{s1})/Mach number (M_1), inlet flow angle (β_1), outlet total pressure (P_{t2})/static pressure (P_{s2})/Mach number (M_2), outlet flow angle (β_2). Mach numbers were calculated using the measured pressures and temperature using Equation 2.

$$M = \sqrt{\frac{2}{0.4} \cdot \left[\left(\frac{P_t}{P_s} \right)^{\frac{0.4}{1.4}} - 1 \right]} \quad \text{(Equation 2)}$$

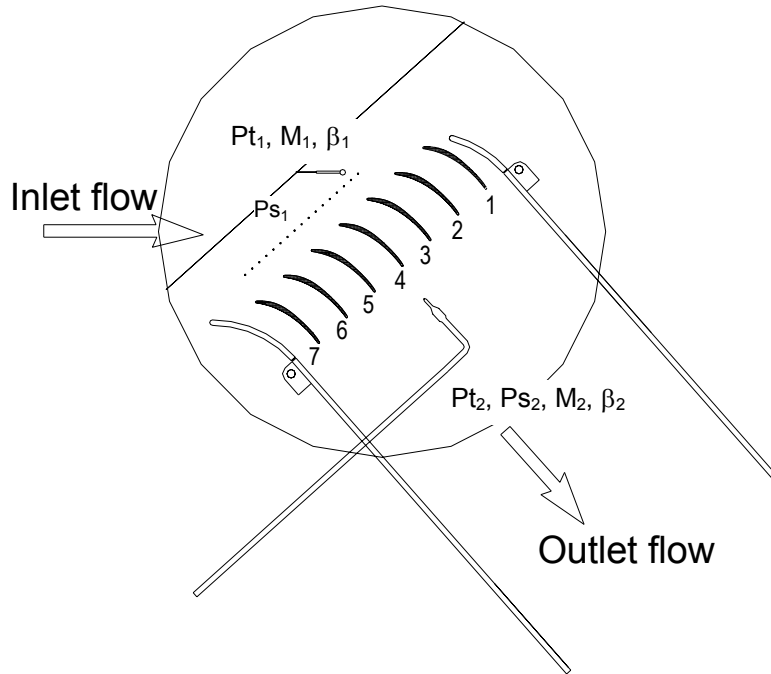


Figure 13 Aerodynamic measurements for the cascade

The inlet total temperature was measured using a type K thermocouple total temperature probe located upstream of the test section. The free stream turbulence intensity was measured using a hotwire at the cascade inlet. Detailed information about the hotwire measurements and data reduction was given by Justin [59]. As seen in Figure 13, the cascade was composed of seven blades, numbered 1 to 7 from the top side to the bottom side. All the aerodynamic measurements were taken in the mid-span plane. Inlet total pressure was measured 87% chord upstream of Blade 2 using a total pressure probe. Inlet flow angle was checked 42% chord upstream of the cascade for different pitchwise locations using a three-hole angle probe (prism-type). Seventeen sidewall pressure taps were evenly spaced in the pitchwise direction 29% chord upstream of the cascade, exactly covering the middle four passages. All of these seventeen locations were used to monitor the inlet flow uniformity/periodicity, while some of them in the middle locations were specifically chosen for inlet Mach number determination.

Another three-hole angle probe (cone-type) was traversed 50% chord downstream of the cascade to measure outlet total pressure, Mach number and flow angle. To meet the specific geometric and aerodynamic requirements of the current cascade tests, this probe was specially designed. Both angle probes were calibrated in a high-speed flow setup.

Details are given in Appendix B. Wake profiles of the blades were obtained from the traverse data. The overall aerodynamic parameters were averaged for the middle two passages (from Blade 3 to Blade 5). Total pressure loss coefficient was calculated using Equation 3:

$$\omega = \int_0^{2 \text{ pitch}} \frac{Pt_1 - Pt_2}{Pt_1 - Ps_1} \quad \text{(Equation 3)}$$

It has been checked out that there is little difference between the overall parameters calculated using mass-average and area-average methods. This research adopted the area-average method. All the pressure measurements were taken using MKS pressure transducers (two ranges: 3 psig and 20 psig) except for the inlet static pressures were measured by a 32-channel PSI pressure system. All the data were recorded by a data acquisition system. The DAQ system was controlled by a computer with a LabVIEW program.

In the experiments, the LabVIEW DAQ program was configured with sampling frequency of 100 Hz and total sampling time of 10 seconds. The traverse of the angle probe was driven by a stepper motor. The motor was controlled by the DAQ computer with another program, with which the traverse speed and distance could be specified. Because the tunnel was a blowdown type, data had to be taken within the short duration of constant flow. However, the traverse speed could not set too high to lose the spatial resolution of the measurement. Through trial and error, it was found the traverse speed around 3.3 cm/s gave a good trade-off, which took about 6.5 seconds for traversing the middle four blade passages. During the experiments, DAQ was turned on 1-2 seconds before the start of the traverse thus all the traverse data was securely obtained within the data recording time of 10 seconds.

The test conditions of the experiments are summarized in Table 3, including the uncertainties for the primary parameters. Detailed uncertainty analysis is given in Appendix C. It should be pointed out that the wind tunnel was not able to control Reynolds number independently, thus leading to Reynolds number variation with inlet Mach number and AVDR. However, the variation was noticed relatively small. In addition, these high Reynolds numbers were far beyond the critical Reynolds number

range for cascade flows. In the critical range ($0.3 - 3.0 \times 10^5$), Reynolds number has significant effect on the total pressure loss coefficient (see page 28 of [1] and page 206 of [4]). Therefore, the effect of Reynolds number on the blade losses in this research can be reasonably neglected.

Table 3 Test Conditions and Experimental Uncertainty

Parameter	Value	Uncertainty
M_1	0.61 – 0.95	± 0.01
M_{1s}	see “Results” chapter	± 0.01
α_1	44.4° – 50.4°	$\pm 0.5^\circ$
α_2	see “Results” chapter	$\pm 0.5^\circ$
AVDR	1.03 – 1.18	± 0.01
Re	$1.15 - 2.0 \times 10^6$	$\pm 0.02 \times 10^6$
Tu	1.2 – 1.6%	$\pm 0.05\%$
ω	0.05 – 0.35	± 0.005

Flow diagnostic experiments included blade surface pressure measurement, shadowgraph for the passage flow and blade surface oil flow visualization. All these results, plus the wake profiles obtained from the downstream probe traverse, helped elucidate the loss mechanisms, as illustrated in Figure 14.

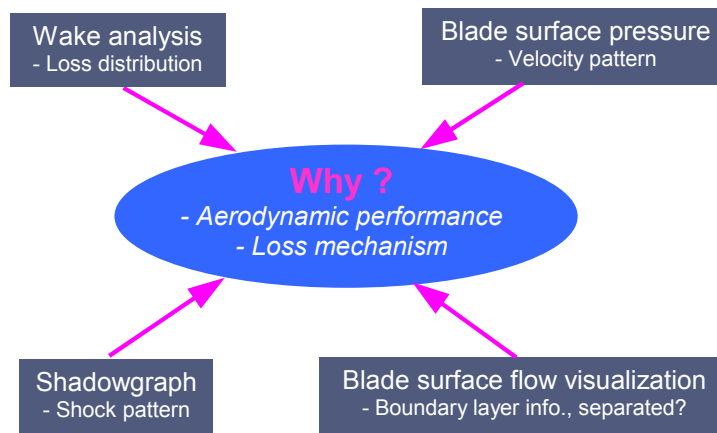


Figure 14 Experimental investigation of loss mechanisms

Blade surface pressure measurement was conducted on the middle passage between Blade 3 and 4 (see Figure 13). Blade 3 was instrumented on the pressure side while Blade 4 was instrumented on the suction side, with pressure taps aligned in the axial direction at the mid-span. A picture of the instrumented blades is given in Figure 15. Using the measured blade surface static pressures and the inlet total pressure, blade surface isentropic Mach numbers can be calculated. As normally adopted by the researchers in this area, the current investigation reduced the surface pressure data into surface Mach number, thus directly exhibiting the velocity development on the blade surface.

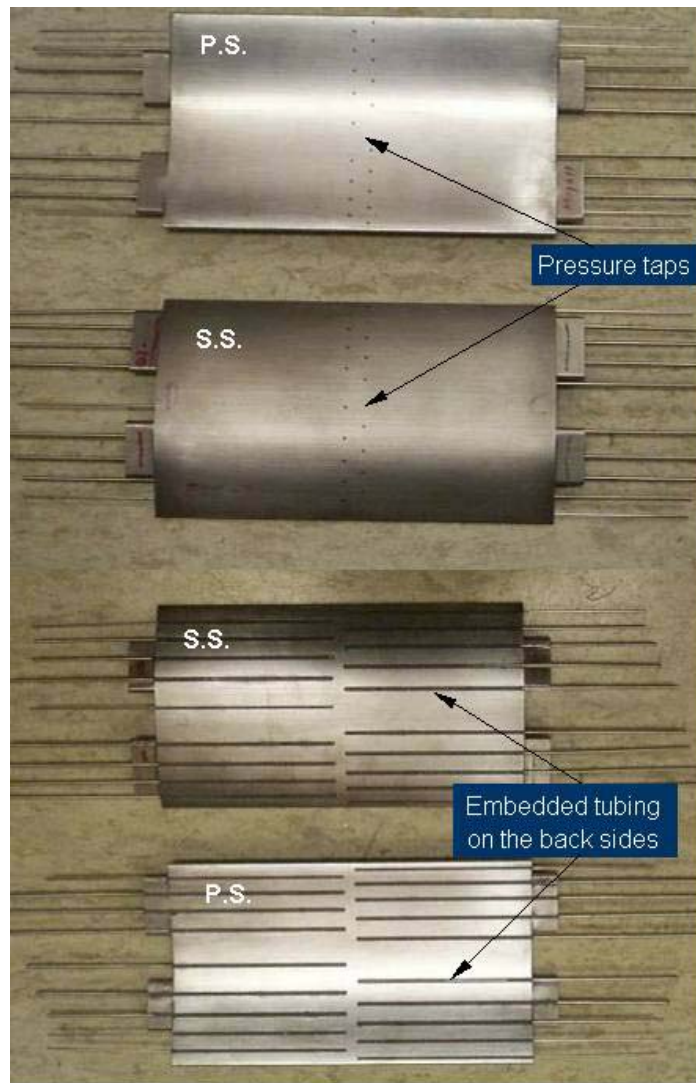


Figure 15 Instrumented blades for surface pressure measurement

Shadowgraphs were taken for the blade passage between Blade 3 and Blade 4, which was intended to visualize the shocks occurring in the blade passage. Goldstein [66] gave a good description of this optical flow diagnostic technique and its application.

Blade surface oil flow visualization was performed on the blade suction surfaces. The blade surfaces were coated with a thin layer of oil in which a finely powdered color pigment was dissolved. When the tunnel was turned on, the colored oil film was carried with the air stream so that the flow direction close to the blade surface was visualized. After the tunnel run, the oil streaky pattern left on the blade could be reviewed to obtain boundary layer development information. Detailed discussion on this flow visualization technique was provided by Merzkirch [67]. Pictures of the blades coated with colored oil were shown in Figure 16, taken before and after the tunnel run.

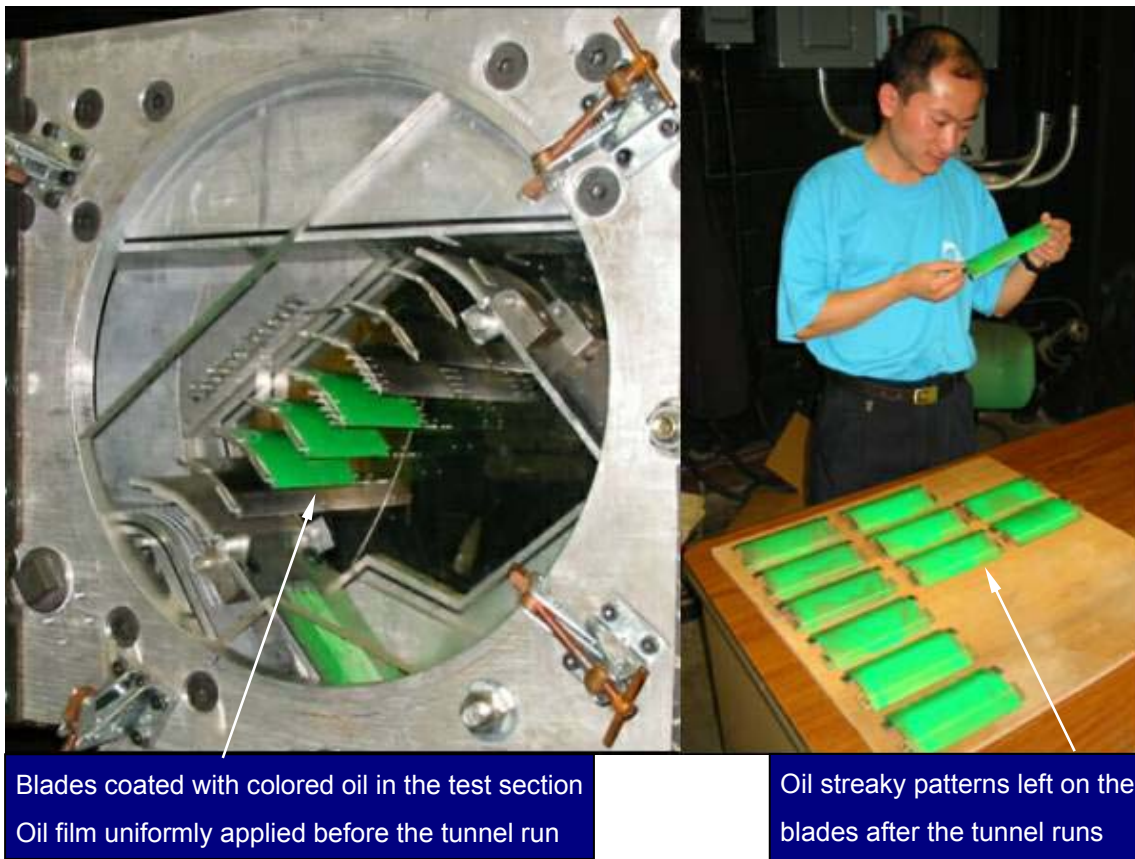


Figure 16 Experiments of blade surface oil flow visualization

2.4 CFD Code

The numerical simulation of the blade-to-blade flowfield in the current research was fulfilled by using an available CFD code, ADPAC (Advanced Ducted Profan Analysis Codes). This code was developed by Allison Engine Company under NASA sponsorship. Brief description of the code is given in this section. For detailed information and the manual for the code, refer to Edward et al. [68].

The code was specifically developed for aerodynamic and/or heat transfer analysis of modern turbomachinery configurations, with the capability of predicting both steady state and time-dependent flowfields by solving Euler or Navier-Stokes equations. It allows either serial execution or parallel execution on massively parallel or workstation cluster computing platforms from a single source. The code utilizes a finite-volume, four-stage Runge-Kutta time-marching numerical procedure in conjunction with a flexible multiple grid block geometric representation to permit detailed aerodynamic simulations for complex configurations. The code had been verified for both turbomachinery and non-turbomachinery based applications. In addition to being used for analyzing the steady and unsteady aerodynamics of high-bypass ducted fans involving multiple blades rows, ADPAC possesses many features which make it practical to compute a number of other flow configurations, such as the cascade flow in the current investigation.

2.4.1 Solution Procedure Sequence

ADPAC is provided as a compressed file which must be processed before utilization. This operation is required only once when the first time use is initiated. Once the source files have been correctly extracted, the sequence of tasks can be started to perform the numerical analysis, as illustrated by the flowchart in Figure 17. Step 1 involves selecting geometry and flow conditions, defining which specific results are desired, and specifying whether steady state or time-dependent data are required, whether inviscid calculation (Euler equations) is sufficient or whether a viscous flow solution (Navier-Stokes equations) is needed. In Step 2 and 3, the geometry is specified (such as the blade profile) and the flow domain is represented by the computational grid. Grid generation can be handled through commercial packages. In this research, GRIDGEN [69] was used.

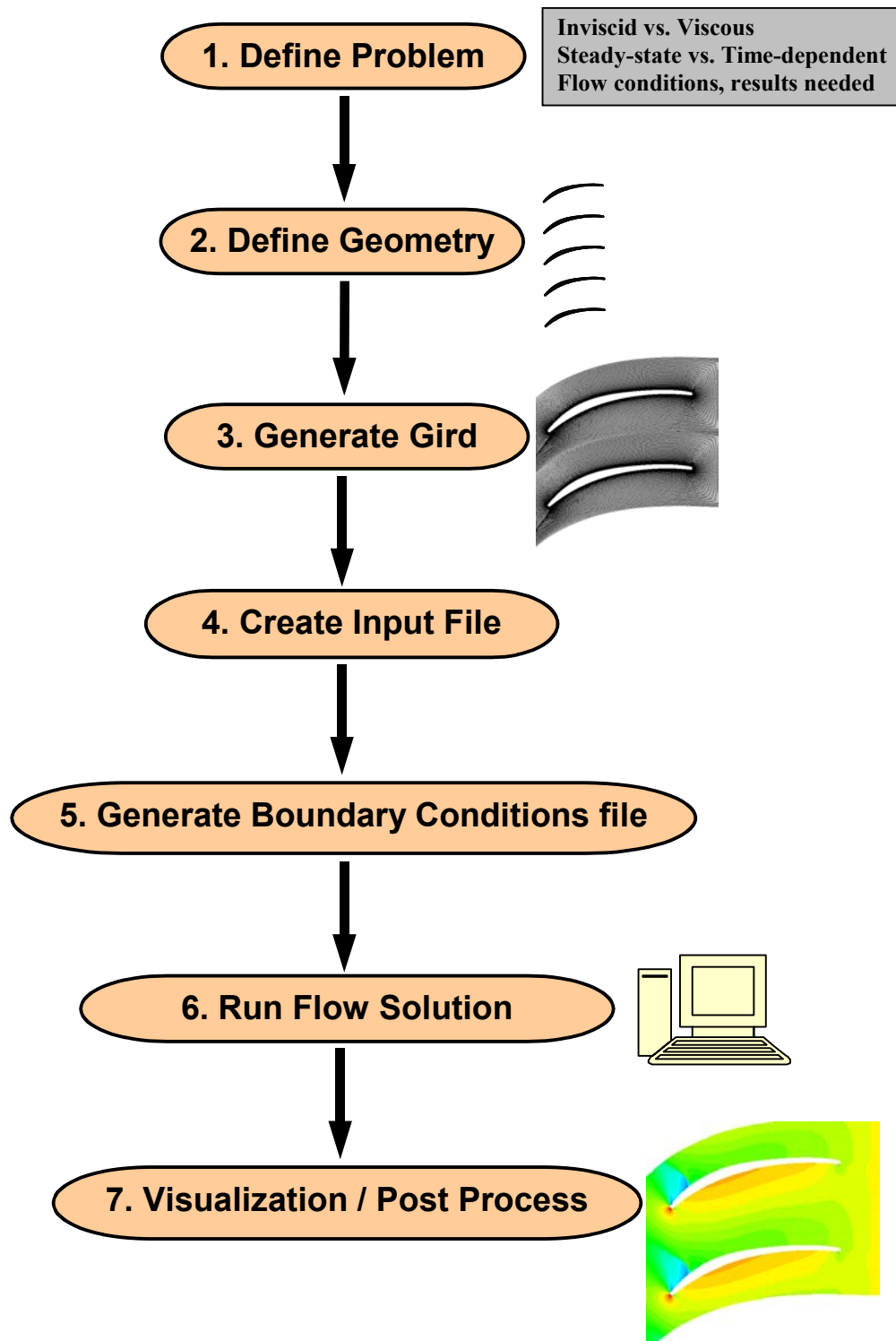


Figure 17 Sequence of tasks of an ADPAC analysis

Most of the work to fulfill a desired execution of the code is included in Step 4 and 5. The standard input file controls operations specific to a particular run of the code. Operations such as the number of iterations, flow conditions, and input/output control are governed by the values specified in the input file. All the boundary condition information is provided by the boundary data file, in which numerous values need to be defined and/or chosen according to the code syntax. In the next section 2.5, preparation of the input and boundary condition files for the current application will be discussed more in detail.

The next step is to run the code. During the computation, some real-time output can provide information about the progress of the code running. The convergence history is also available for review. When the computation ends, all the results are stored in a file named “PLOT3D”. Commercial post-processing softwares can be used by to read the output files and create the plots of the flowfield. A commercial software, FIELDVIEW [70, 71], developed by Intelligent Light, was used for all the post-processing of the numerical solutions in the current research.

2.4.2 Numerical Algorithms

In CFD, a flow domain is discretized by a grid. Many CFD analyses rely on a single structured ordering of the grid points (one block) upon which the numerical solution is performed. In comparison, a multiple-block grid system has several structured grid units (multiple blocks) used in harmony to generate the numerical solution. The comparison is illustrated for a two-dimensional flow through a nozzle in Figure 18 (from Edward et al. [68]). The single block in the top of Figure 18 results in a single computational space. In theory, the nozzle flow path could be subdivided into a number of domains. As shown in the bottom of Figure 18, twenty blocks are used, resulting in twenty computational domains. Multiple-block grids make the computation complicated in that the numerical solution must provide a means for the isolated blocks to communicate with each other in order to satisfy the conservation laws governing the aerodynamic solution.

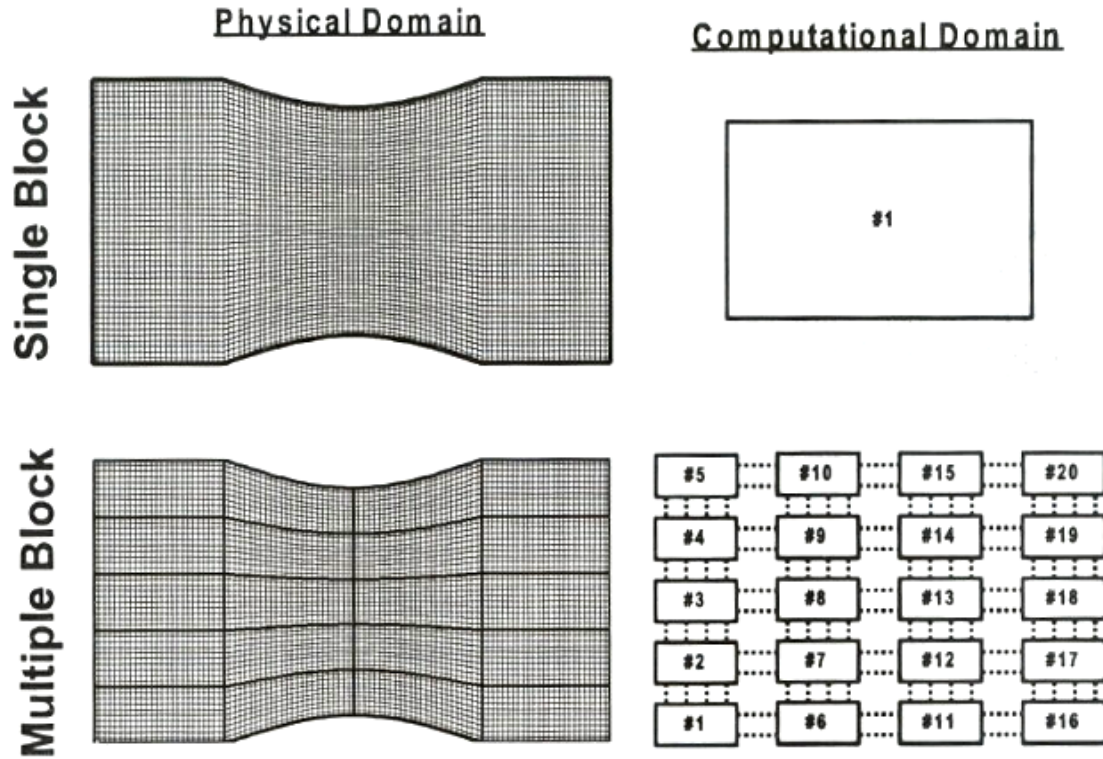


Figure 18 ADPAC single-block and multiple-block

For a simple nozzle case illustrated in Figure 18, there is virtually no advantage in using a multiple-block grid system. However, for a more complicated case, such as the flow in a turbomachine, a multiple-block grid system has significant advantages in that it easily encompasses the domain of interest with high grid quality that seems impossible for a single structured grid. An example is given in Figure 19 (from Edward et al. [68]) for a flow passing a turbomachinery blade. In this case, three blocks are used, one H-shaped block for the inlet region, one O-shaped block surrounding the blade, and one H-shaped block for the exit region. This type of so called H-O-H grid system has been widely used in CFD for solving the flowfields around an aircraft wing or in the compressor/turbine cascade. ADPAC fully utilizes the multiple-block grid concept by permitting an arbitrary number of structured grid blocks with user specifiable communication paths between blocks. The inter-block communication paths are implemented as a series of boundary layer conditions on each block and in some cases by communication from one block to another. The multiple-block solution concept provides

an effective means of treating complicated geometries, particularly for turbomachinery configurations, such as multiple blade rows with varying blade number, endwall treatment.

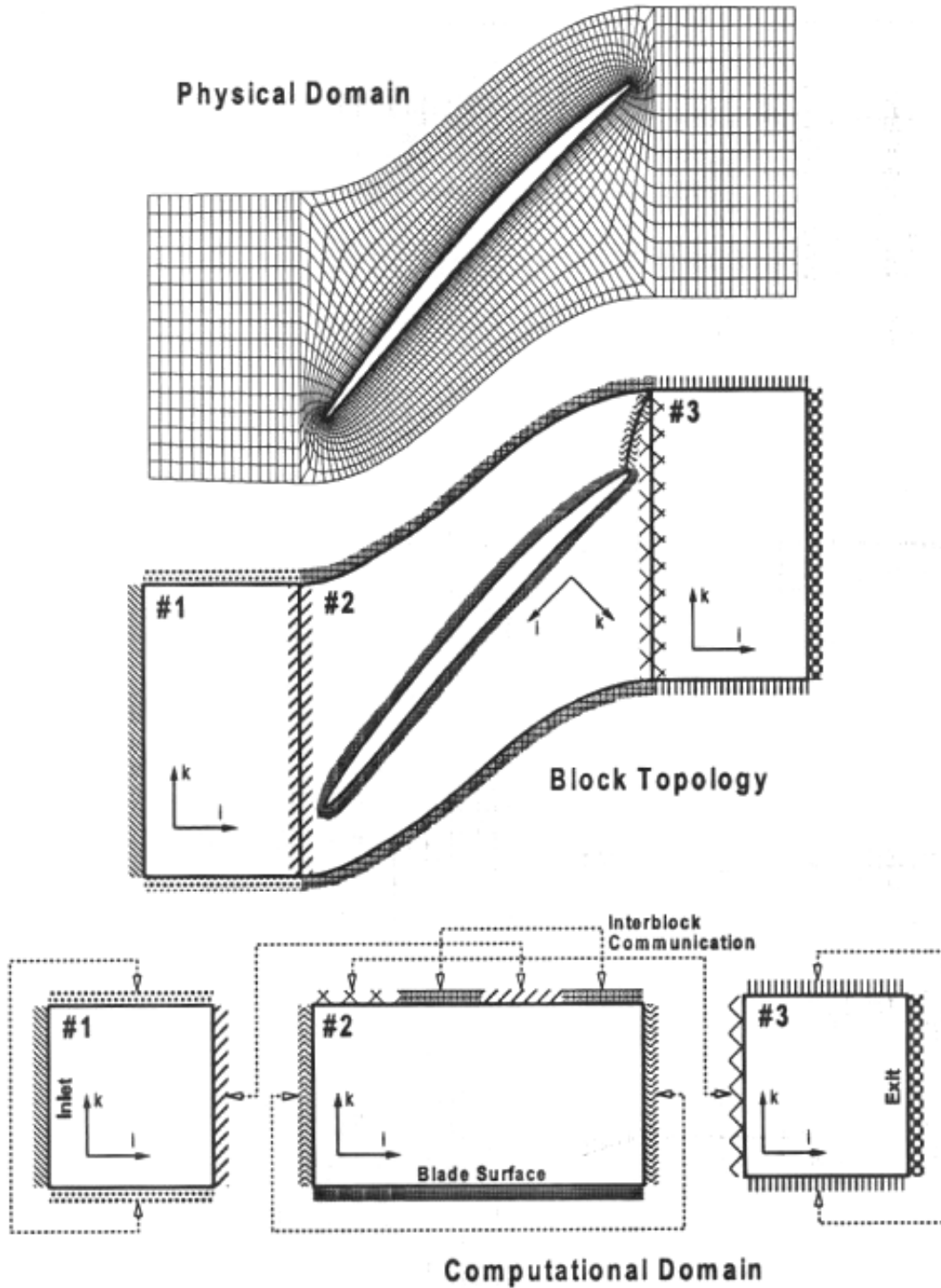


Figure 19 H-O-H grid system and computational domain communication

Another numerical solution technique is incorporated into ADPAC with an attempt to accelerate the convergence of an iterative process. The idea is to make the computation on coarser meshes and propagate the obtained solution to the fine mesh through interpolation. This operation may be recursively applied to several coarsenings of the original mesh to effectively enhance the overall convergence. Coarse meshes are derived from the preceding finer mesh by eliminating every other mesh line in each coordinate direction. As a result, the number of multi-grid levels (coarse mesh divisions) is controlled by the mesh indices of the boundary patches used to define the boundary conditions on a given mesh block in ADPAC. It can be seen that this technique cuts down the computation time by generating a reasonably approximate solution on the coarser meshes before undergoing the expenses of the fine mesh iterations. An illustration of the multi-grid convergence acceleration concept is given in Figure 20 (from Edward et al. [68]).

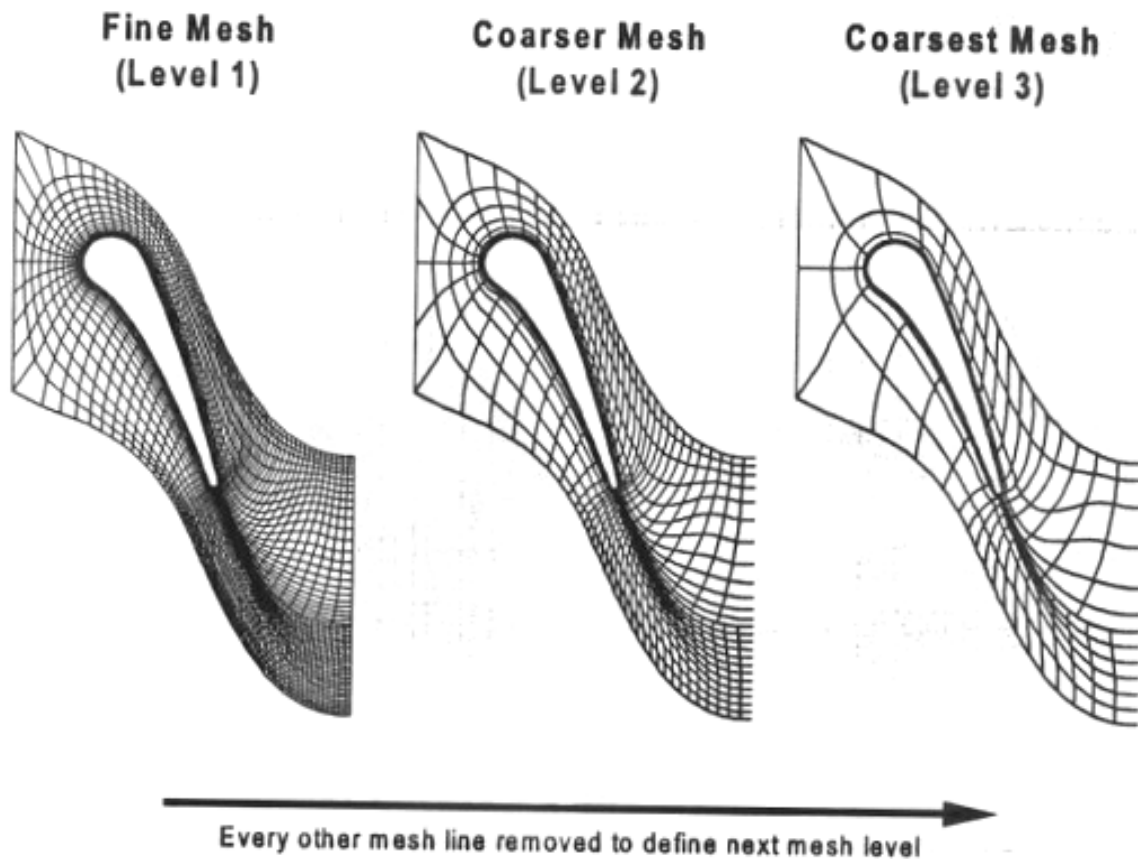


Figure 20 Multi-grid mesh coarsening

2.4.3 Governing Equations

ADPAC numerical solution procedure is based on an integral representation of the strong conservation law form of the three-dimensional Reynolds-Averaged Navier-Stokes (RANS) equations. Detailed derivations of the various forms of the equations used ADPAC are not included herein but can be found in Appendix A of Reference [68]. User input allows the choice of different solution schemes, which can be made on a block-by-block basis. Solving Euler equations, two-dimensional flow, and steady flow can be obtained as a simplified subset of the full three-dimensional Navier-Stokes equations by configuring the input file and the boundary condition file. An example of setting the solution scheme will be shown in Section 2.5, for the application of the code to the current work.

Four turbulence models are available from ADPAC for users to choose for a specific application need.

- Mixing-Length Turbulence Model [72]
- Algebraic Baldwin-Lomax Turbulence Model [73]
- One-Equation Spalart-Allmaras Turbulence Model [74]
- Two-Equation Turbulence Model [75]

Other information of the computational methodology involved in solving the governing equations can be also found Appendix A of Reference [68], including “Nondimensionalization”, “Fluid Properties”, “Numerical Formulation”, and “Boundary Conditions”.

2.5 CFD Procedure of the Current Work

Numerical investigation was performed on the cascade flows for the three blades, ORG, ES and MOGA, using the above described CFD code (ADPAC). The code was set to solve the two-dimensional steady Navier-Stokes equations with the choice of One-Equation Spalart-Allmaras Turbulence Model. According to previous successful application of ADPAC to cascade flows [76], this turbulence model gave the best solutions, which was concluded based on the comparison with experimental data. Numerical simulation of the flowfield was conducted for a series of inlet Mach numbers and inlet flow angles, covering all the experimental conditions. With the comparison and confirmation of the available experimental results, numerical results fully characterized the flowfield, providing detailed flow information such as flow speed, pressure, shock pattern, boundary layer development, losses, etc. The flowfield information from CFD simulation was then used to help elucidate the flow physics.

2.5.1 Computational Domain

As normally used for cascade flows, the H-O-H grid system was adopted. As shown in Figure 21, using the multiple-block grid system allows a fine mesh round the blade (i.e., in the blade passage) and fits the blade shape very well. Near the blade surface, the mesh is set even finer. All these mesh characteristics lead to improved resolution of flow information from the computation, thus are advantageous to better predict boundary layer development and capture shocks. After trial and error, the grid size was chosen as: inlet region 49×45 , blade region 461×45 , and outlet region 49×57 . This grid size was demonstrated fine enough for the computation and used for all the numerical simulation in the current research. In fact, calculations were also conducted for a finer grid system, which gave the same solutions as the original grid. Figure 22 gives the comparison between the two grids. The higher compactness of the grid lines of the finer grid can be clearly seen.

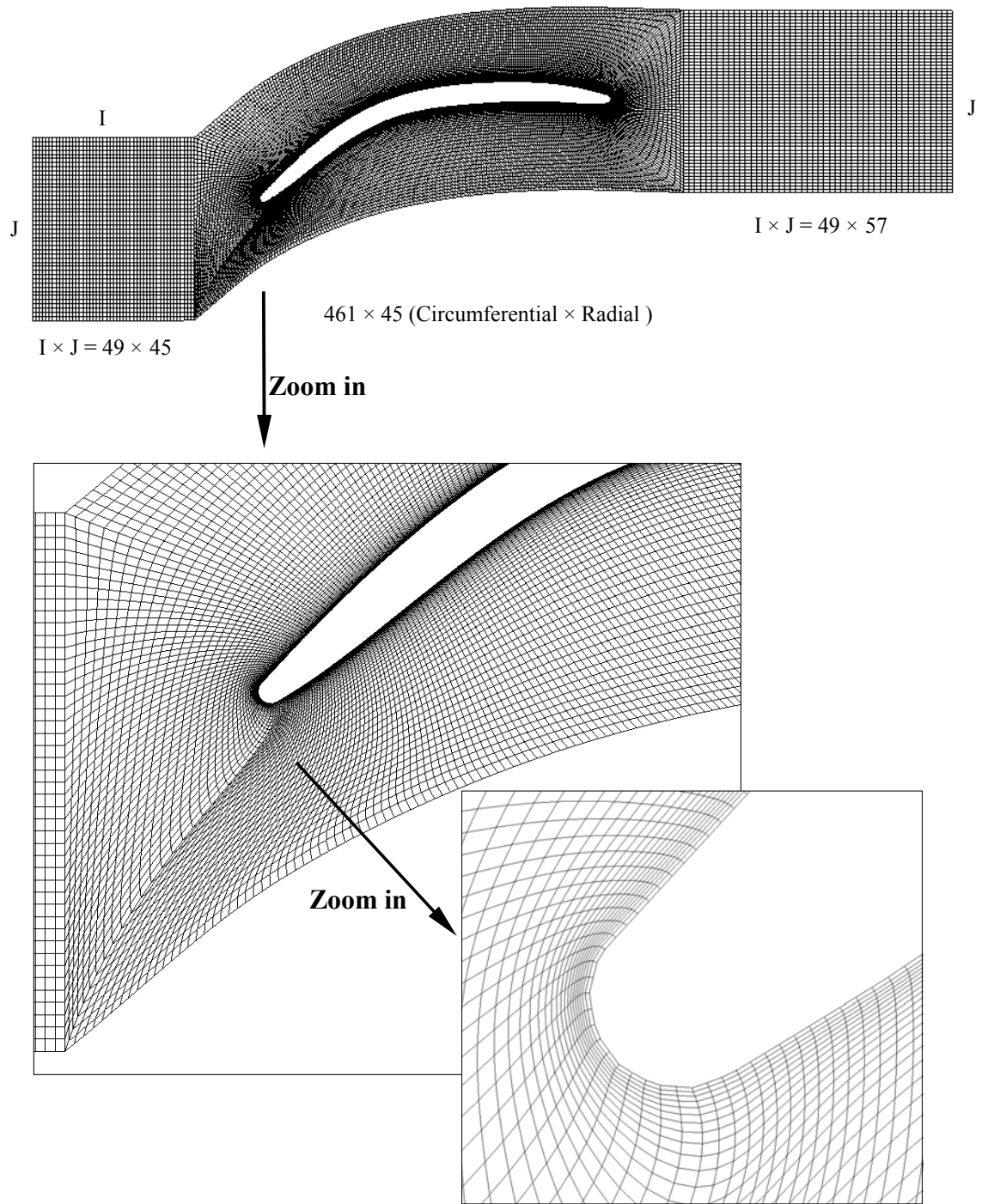


Figure 21 The H-O-H grid system used in the current CFD work

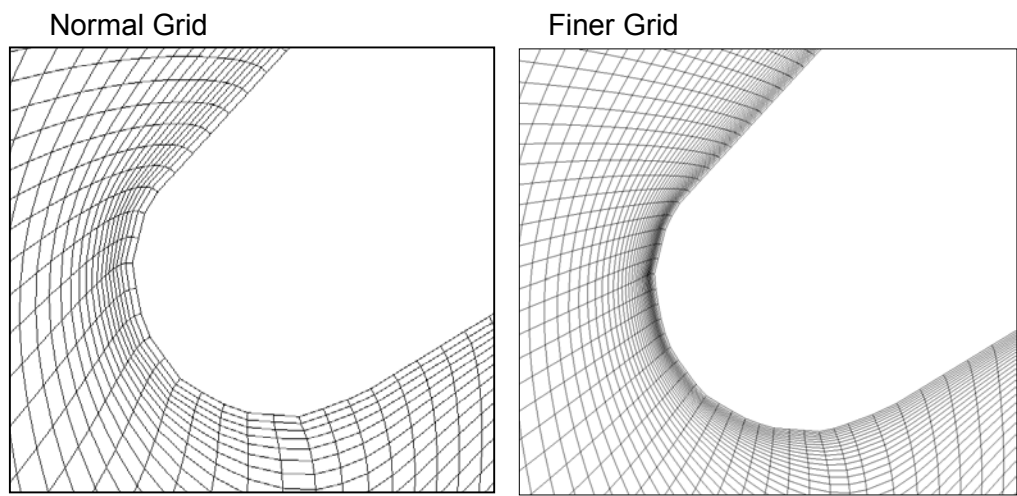
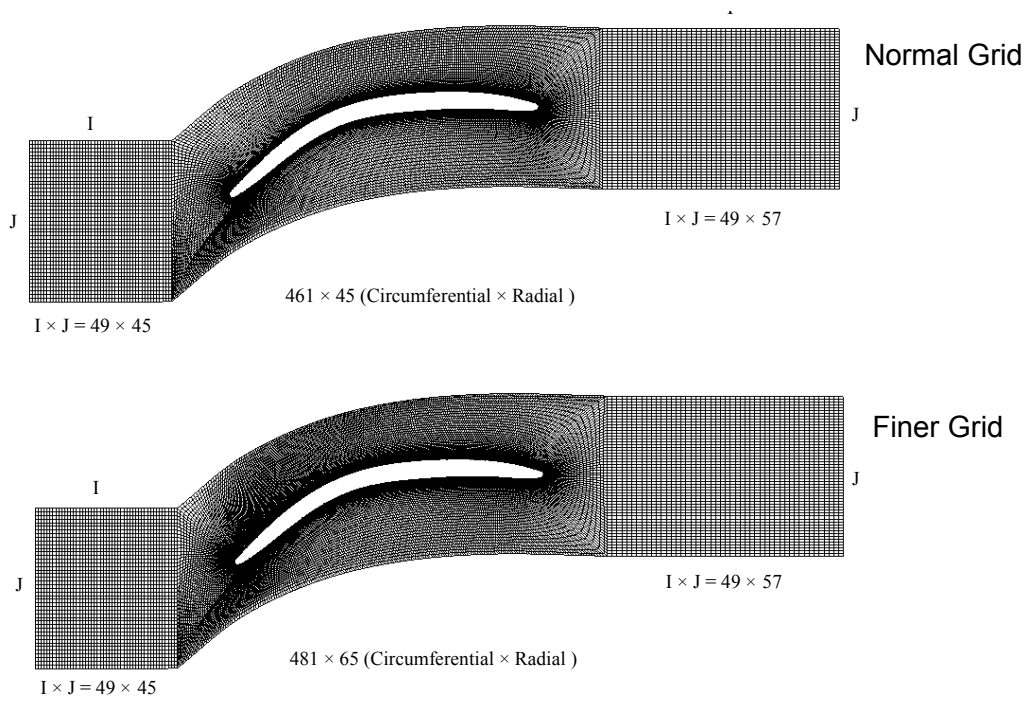


Figure 22 The finer grid compared to the normal grid

2.5.2 Code Input File

The standard ADPAC input file is named “*case.input*,” where *case* is the user-specified computation case name used for all the files, and *input* is the extension name describing the type of the file. So all files used in an ADPAC calculation are name following the standard form: *case.extension*. The input file contains the user-specified parameters which allow the user to control the basic operation of the code. During code execution, the input file is read one line at a time as a character string, and the strings are arranged sequentially to determine the specific code action in each case. The input file utilizes a keyword input format, such that any line which does not contain a recognizable keyword is taken as a comment line. Therefore, the user can place any number of comments in the file as long as the line does not contain a keyword input string in the standard form, and the code execution is unaltered. Comments may also be placed after the variable assigned to the keyword if only there are one or more blanks separating the keyword value from the comment string.

All keyword input lines are given in the format below:

KEYWORD = Value Comment String

where KEYWORD is one of the standard recognized keywords built in the code, and Value is the specific value to be assigned to that variable by the user. The input line must contain the equals sign (=) with one or more blanks on both sides in order to be read correctly. The Comment String must also be separated by one or more blank spaces from the Value.

It is unnecessary to specify all possible keywords in the input file. The code is programmed with a default set of input variables such that the only input variable which must be present is the CASENAME. A list of the input variables is given in Table 4. Table 4 is one actual input file used in the current research, for Blade ORG. Those necessary and important variables are specified and described in the file.

Table 4 One Input File Used in the Numerical Study

File Name: *org.input*

```

=====
#-----
# ADPAC Input File Generated by SETUP-Version 1.02
# (05/15/2003 – Bo Song)
# (Desired Mach Number = 0.7)
#-----
#           JOB TITLE
#-----
#           Compressor Cascade-ORG Input File
#-----
#           INPUT DATA
#-----
# VARNAME = VARIABLE VALUE  COMMENT
#-----

CASENAME   =   org           The case name is “org” (for Blade ORG)
CFL        =  -5.000000     Setup default-local time stepping, -5.0 is normally for
                               steady flow
CFMAX      =   2.500000     Setup default-time-marching smoothing
DIAM       =   0.083333     Setup default-unit conversion for the mesh, 1/12 foot
EPSTOT     =   0.200000     Multigrid smoothing coefficient
EPSX       =   1.000000     Setup default-residual smoothing coefficient
EPSY       =   1.000000     Setup default-residual smoothing coefficient
EPSZ       =   1.000000     Setup default-residual smoothing coefficient
F1EQ       =   1.0          SA one-equation turbulence model, disable other models
FCART      =   1.0          Cartesian coordinate
FFILT      =   1.000000     Setup default-added dissipation
FINVVI     =   1.000000     1: viscous flow 0: inviscid flow
FITCHK     =  100.00000     Setup default-checkpoint restart iteration interval
FITFMG     =  100.00000     Setup default-full multigrid iterations
FKINF      =   20.0         X value of SA one-equation turbulence model,
                               recommended value around 20

FMULTI     =   1.000000     no multigrid, set integers ≥ 1 to turn on multigrid
FNCMAX     =  4000.000000   Total number of iterations, as long as good convergent
                               solutions obtained
FRESID     =   1.000000     Setup default-residual smoothing trigger

```

FREST	=	0.000000	Setup default-no restart; 1: restart file called
FSAVE	=	1.000000	Setup default-restart file written trigger
FSOLVE	=	1.000000	Setup default-time marching strategy choice (0,1,2)
FTIMEI	=	1.000000	Setup default - iteration between time step,updated every iteration
FTOTSM	=	1.000000	Post multigrid smoothing trigger,aid stability, but hinder convergence sometime
FTURBB	=	10.000000	Setup default-iteration number when turbulence model activated, recommended ≥ 10
FTURBI	=	1.000000	Setup default-turbulence parameters updated every iteration
FVTSFAC	=	2.500000	Setup default-viscous time step factor
FWALLF	=	0.000000	No wall functions
GAMMA	=	1.400000	Setup default-gas specific heat ratio
P3DPRT	=	1.000000	PLOT3D output trigger (on=1.0)
PREF	=	2530.0000	Inlet Pt (lbf/ft ²), match experimental conditions
PRNO	=	0.700000	Setup default-gas Prandtl number
PRTNO	=	0.900000	Setup default-Gas turbulent Prandtl number
RGAS	=	1716.260010	Setup default-gas constant (ft-lbf/slug-R)
RMACH	=	0.7	Initial inlet flow Mach, will be ultimately determined by Boundary File set separately
TREF	=	510.000000	Inlet Tt (Rankine) match experimental conditions
ENDINPUT			

The first couple of lines in the input file are the user comment lines, which start with the mark “#” so that the code dose not read them for the execution. The important variables in the input file which are dealt with most frequently in the numerical study are described below.

CASENAME specifies the case name required by the code, as mentioned above. FNCMAX specifies the total iteration number, which terminates the code execution whether a satisfactory convergent solution is obtained or not. Therefore, it is the user’s task to find an ideal iteration number through trial and error. To saving computing time,

the iteration is chosen with just sufficient times to allow convergent solutions. The criteria for the convergence are available in the convergence file which keeps the convergence history of the computation. An example of the computing convergence history obtained in the current study is given in Table 5. It has been demonstrated that a convergent solution can be deemed when the RMS residual is less than -6 order of magnitude and the inlet mass flow rate matches the outlet mass flow rate very well (satisfying mass conservation law). As seen in Table 5, this computation case is deemed convergent.

Table 5 One Convergence File obtained in the Numerical Study

File Name: *org.converge*

CYCLE NUMBER	MAXIMUM RESIDUAL \log_{10} of residual	RMS RESIDUAL \log_{10} of residual	MASS INFLOW	MASS OUTFLOW
1	-0.38407	-3.78606	0.49515	0.60688
...				
10	-0.65141	-3.76557	0.45923	0.58512
...				
1000	-2.18406	-5.12472	0.42695	0.41323
...				
2000	-2.74024	-6.00612	0.41843	0.41684
...				
3000	-3.61342	-6.75684	0.42002	0.42018
...				
4000	-4.31722	-7.33921	0.42203	0.42209

PREF and TREF are the other most important variables in the input file. They specify the total pressure and total temperature for the cascade inlet flow. If experimental data is available for the comparison with the CFD results as in the current research, PREF and TREF should certainly be chosen as the same as the experimental conditions. This rule applies for all the numerical simulations wherever experimental data is available.

A complete and detailed description of the variables in the standard ADPAC input file is available from Edward et al. [68].

2.5.3 Code Boundary Data File

The ADPAC boundary data file contains the user-specified parameters which control the application of boundary conditions on the multiple-block mesh during a solution. These specified parameters determine the location of solidwall or periodic boundary condition, inflow/outflow regions, and block-to-block communication paths. The boundary data file follows the standard ADPAC name format so that it is named “*case.boundata*” where the case name can be specified by the user.

Several boundary condition application concepts are used in the ADPAC program. The “Phantom Cell” concept is employed in the finite volume solution algorithms. The phantom cells are automatically defined in the code and the user needs not to deal with generating fictitious points within the mesh to accommodate the boundary condition application procedure. Another important aspect of the application of boundary conditions in the code involves the order in which boundary conditions are applied. ADPAC applies all the boundary conditions to the various mesh blocks in the order in which they are specified in the boundary data file. As a result, it is possible to overwrite a previously specified boundary patch with subsequent different conditions. This necessitates the user’s proper precautions to prohibit accidentally overwriting a desired boundary patch. During code execution, the boundary data file is read one line at a time as a character string. Each string should be parsed sequentially. The boundary data file uses a keyword input format as the input file so that comments can be added. A boundary data file used in the current work is given in Table 6. All boundary specifications begin with a line containing 19 variables as outlined by the labels in the table.

More explanation on the boundary condition application concepts and a detailed description of the function of each of the variables in the boundary specification line is given by Edward et al. [68]. Nevertheless, it is worth mention of the important functions of some variables in the boundary data file as shown in Table 5. PTOT and TTOT are normalized inlet total pressure and temperature which are specified in the input file. ALPHA is the user-specified inlet flow angle. CHI is the coefficient used in the One-Equation Spalart-Allmaras Turbulence Model, usually recommended 1.0 for turbulent flow. PEXIT is the normalized exit static pressure with respect to the inlet total pressure. The user adjusts this PEXIT value to get the desired inlet Mach number.

Table 6 One Boundary Data File Used in the Numerical Study

File Name: *org.boundata*

```

=====
#-----
# ADPAC Bound Data File
# Grid generated using Gridgen
# Inlet flow angle = 48.4 deg, desired inlet Mach number = 0.7
# ORG blade, Bo Song - 05/15/2003
#-----
#
# BLOCKDATA FOLLOWS:          LABELS
#
# B   L L L L L L L L L L M M N N M M N N C
# C   B B F F D D S S 1 2 1 1 1 1 2 2 2 2 O
# T   L L A A I I P P L L L L L L L L L M
# Y   O O C C R R E E I I I I I I I I I M
# P   C C E E 1 2 C C M M M M M M M M M E
# E   K K 1 2      1 2      1 2      1 2      1 2      1 2      1 2      N
#      1 2
#-----

PROBE  1 1 I I P P M M 2 2 1 45 1 2 1 45 1 2 Blk #1 face - inlet flow (mass ave)
PROBE  3 3 I I M M M M 48 48 1 57 1 2 1 57 1 2 Blk #2 exit - exit flow (mass ave)

PATCH  1 2 I J M M J K 49 45 1 45 1 2 1 45 1 2 Blk #1-#2
PATCH  2 1 J I M M I K 45 49 1 45 1 2 1 45 1 2 Blk #2-#1

PATCH  1 1 J J M P I K 45 1 1 49 1 2 1 49 1 2 Blk #1-#1 top-bottom periodic
PATCH  1 1 J J P M I K 1 45 1 49 1 2 1 49 1 2 Blk #1-#1 top-bottom periodic

PATCH  2 2 I I P M J K 1 461 1 45 1 2 1 45 1 2 Blk #2-#2 I-Faces
PATCH  2 2 I I M P J K 461 1 1 45 1 2 1 45 1 2 Blk #2-#2 I-Faces

PATCH  2 3 J I M P I K 45 1 225 281 1 2 57 1 1 2 Blk #2-#3
PATCH  3 2 I J P M J K 1 45 1 57 1 2 281 225 1 2 Blk #3-#2

PATCH  2 2 J J M M I K 45 45 45 225 1 2 461 281 1 2 Blk #2-#2 top-bottom periodic
PATCH  2 2 J J M M I K 45 45 281 461 1 2 225 45 1 2 Blk #2-#2 bottom-top periodic

PATCH  3 3 J J M P I K 57 1 1 49 1 2 1 49 1 2 Blk #3-#3 top-bottom periodic
PATCH  3 3 J J P M I K 1 57 1 49 1 2 1 49 1 2 Blk #3-#3 top-bottom periodic

SSVI   2 2 J J P P I K 1 1 1 461 1 2 1 461 1 2 Blk #2 blade surface
RPMWALL  TWALL
      0.0      0.0

INL2DA  1 1 I I P P J K 1 1 1 45 1 2 1 45 1 2 Blk #1 inlet flow
PTOT  TTOT  ALPHA  CHI
      1.00  1.00  48.40  1.0

EXITG   3 3 I I M M J K 49 49 1 57 1 2 1 57 1 2 Blk #3 exit
PEXIT
      0.881
=====

```

3. Results and Discussion

This chapter presents experimental and numerical results of the blade performance and the associated flow physics. Focusing on the design condition, Section 3.1 provides cascade test results to confirm the blade design/optimization, followed by a detailed discussion of the loss reduction mechanism. Section 3.2 extended the discussion to different Mach numbers at the design incidence angle. The blades are further evaluated at off-design incidence conditions in Section 3.3. Therefore, a systematic study of the blades has been completed.

3.1 Cascade Performance and Flow Physics at the Design Condition

Cascade tests were conducted for the three blades at the design condition ($\alpha_1 = 48.4^\circ$, $M_1 = 0.87$) to evaluate the blade performances, including loss, static pressure ratio and exit flow angle. As discussed in Section 2.1.2, AVDR is an important parameter in two-dimensional linear cascade testing and it could influence the cascade flow and the blade performance. Therefore, the blade performances were tested with the variation of the AVDR. The objective was to make sure that the evaluation of the relative performances of the three blades was not biased by the AVDR influence. Then the flow physics at the design condition is discussed by presenting additional experimental and numerical results.

3.1.1 Experimental Results of Losses

Figure 23 shows the tested losses of the three blades at the design condition with the variation of AVDR. It is seen that AVDR has a large influence on the losses of the baseline blade but small influence on those of the optimized blades. This indicates that the blades have different interaction between the mid-span main flow and the sidewall secondary flow, and the effect of AVDR on losses is coupled with different flow behaviors of the blades. The AVDR values of the three blades are different despite the same sidewall configuration and air bleed procedure used. ORG has the lowest AVDR, ES has the intermediate AVDR and MOGA has the highest AVDR. For each blade, the lowest AVDR data point corresponds to the highest sidewall air bleed rate with slotted

sidewalls while the lowest AVDR data point corresponds to the solid sidewall condition. It is seen that with increasing AVDR, losses decrease for all the three blades. Detailed analysis of the AVDR influence is given in Appendix A.

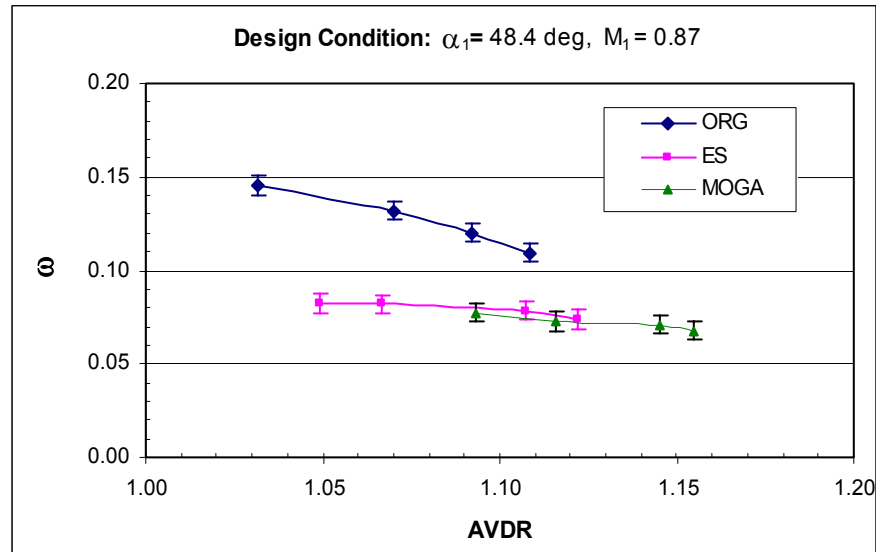


Figure 23 Experimental losses at the design condition

Despite the existing AVDR influences, the superiority of the optimized blades to the baseline blade has been clearly demonstrated. In other words, the AVDR influence in the current study does not bias the relative comparison of the blade performance. The optimized blades have much lower losses than the baseline blade and MOGA has even slightly lower losses than ES. Quantifying the loss reduction at AVDR=1.11 (corresponding to the smallest loss reduction in the tested AVDR range), about 30% loss reduction has been achieved on the optimized blades.

3.1.2 Experimental Results of Pressure Ratio and Exit Flow Angle

Besides the total pressure loss coefficient, two important parameters to characterize the blade performance are static pressure ratio and exit flow angle. They were also measured in the experiments. As shown in Figure 24, higher pressure raise has been achieved on the optimized blades. This is in accordance with the superior compression and lower losses of the optimized blades. The trend of the pressure ratio decreasing with increasing AVDR was also found by Schreiber and Starken [39] on a

low-turning transonic compressor cascade and by Steinert et al. [52] on a medium-turning subsonic compressor cascade.

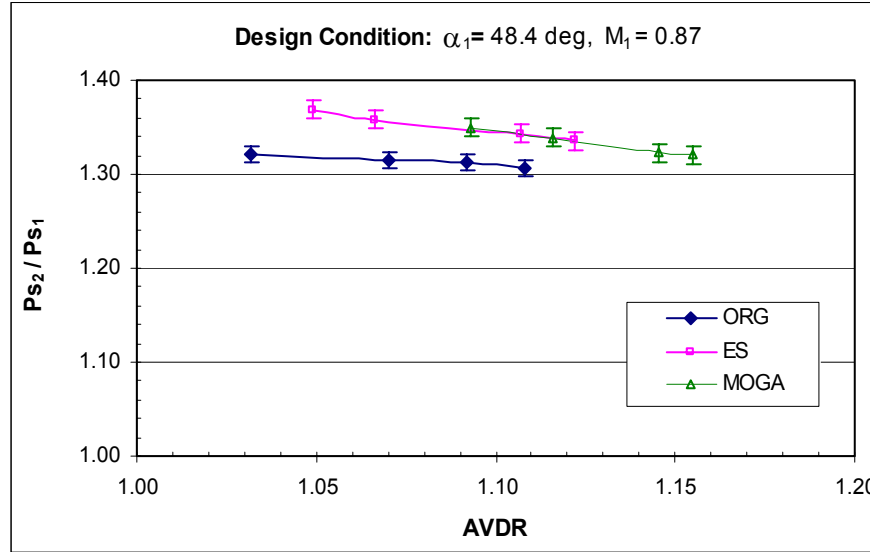


Figure 24 Experimental static pressure ratios at the design condition

Figure 25 shows the results of the exit flow angle. Relative to the design exit flow angle of 0° , positive values of the angles mean under-turning of the flow and vice versa. It can be seen the exit flow angle of ORG is around 0° , ES around 2° , and MOGA around 3° . Although the optimized blades have much lower losses, the major objective of the blade design/optimization, they sacrifice the flow turning to some degree. This flow under-turning from the optimized blades needs to be taken into account during the compressor stage matching. If $2\text{-}3^\circ$ flow under-turning could not be accepted for the stage matching, further blade shape tailoring for the optimized blades is needed to obtain higher flow turning. Considering MOGA has 2° less camber than the baseline, achieving higher flow turning by enlarging the camber angle is practical. Further discussion of this issue is out of the scope of this dissertation, and will be an interesting future work.

Figure 25 also shows the different AVDR effect on the flow turning of the three blades. The overall decreasing trend of the exit flow angle with increasing AVDR was noticed from previous research [39, 52], but those published flow angle data still had the scattering of about one degree, which is equivalent to what was obtained in the current

experiment. It should be pointed out that, accurately measuring flow angle in cascade testing is a well-known challenge. As shown by Gostelow [1], the principal difficulty in measuring flow angle using angle probes lies in the wake region, where large total pressure gradient exists. Different types of probe could indicate different extents of peaks and troughs in the pitchwise distribution. In addition, the uncertainty associated with the angle probe (design, calibration, and application) may cause extra data scattering. Taking into account all these factors, the measured flow angles in cascade testing would be acceptable if the overall flow angles could be determined with the uncertainty of one degree. In the current experiment, the flow angle measurements are adequate to relatively evaluate the flow turning of the three different blades.

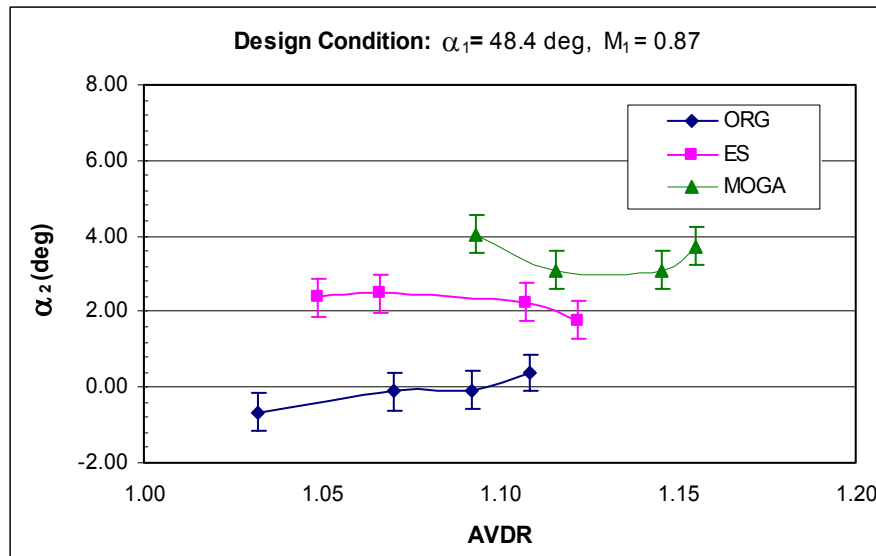


Figure 25 Experimental exit flow angles at the design condition

3.1.3. Flow Mechanisms for the Loss Reduction

In order to seek the flow mechanisms for the significant loss reduction from ORG to ES and MOGA, a series of experiments were further performed in conjunction with CFD flowfield characterization. The associated flow physics is elucidated using wake profile, blade surface flow visualization, shadowgraph, boundary layer profile, contours of Mach number/total pressure loss coefficient/pressure gradient, and blade surface pressure gradient.

Wake Profile

Downstream traverse wake profiles (pitchwise distribution of total pressure loss coefficient) are shown in Figure 26. Wider and deeper wakes are observed on ORG (a sign of possible boundary layer separation), leading to much higher overall losses. ES and MOGA have the same wake size, but ES has a small loss bump in the mainstream, which accounts for the slightly higher overall losses than MOGA. More results will be shown next, which provide better understanding of the wake profiles.

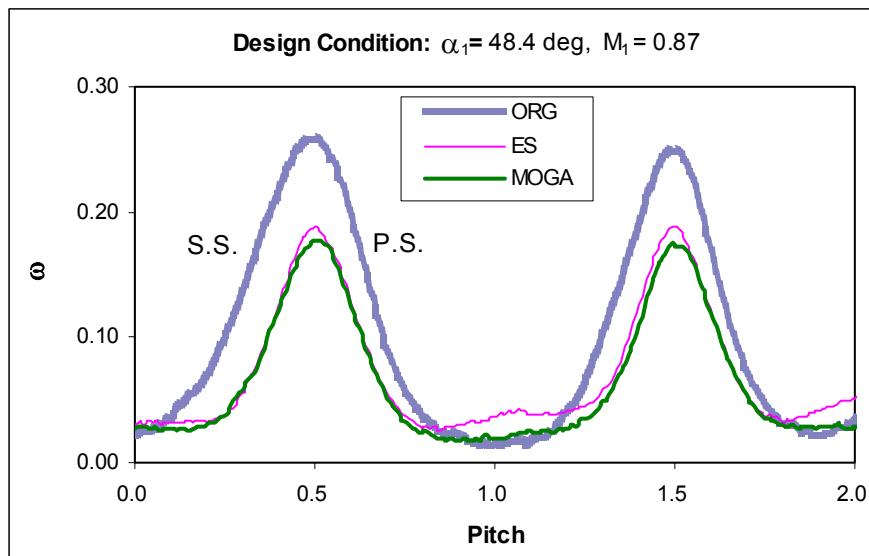


Figure 26 Experimental wake profiles at the design condition

Blade Surface Oil Flow Visualization

Blade boundary layer development was investigated using blade surface oil flow visualization. The oil streaky patterns left on the blades after the tunnel runs were photographed, as shown in Figure 27. During the tunnel run, reverse flow was observed on the suction surface of ORG. This confirmed the boundary layer separation, starting around 20% chord and not reattaching. In contrast, ES and MOGA had attached flow all the way toward the trailing edge, i.e., no boundary layer separation occurred. These experimental results explain why the optimized blades have much smaller wakes and much lower losses.

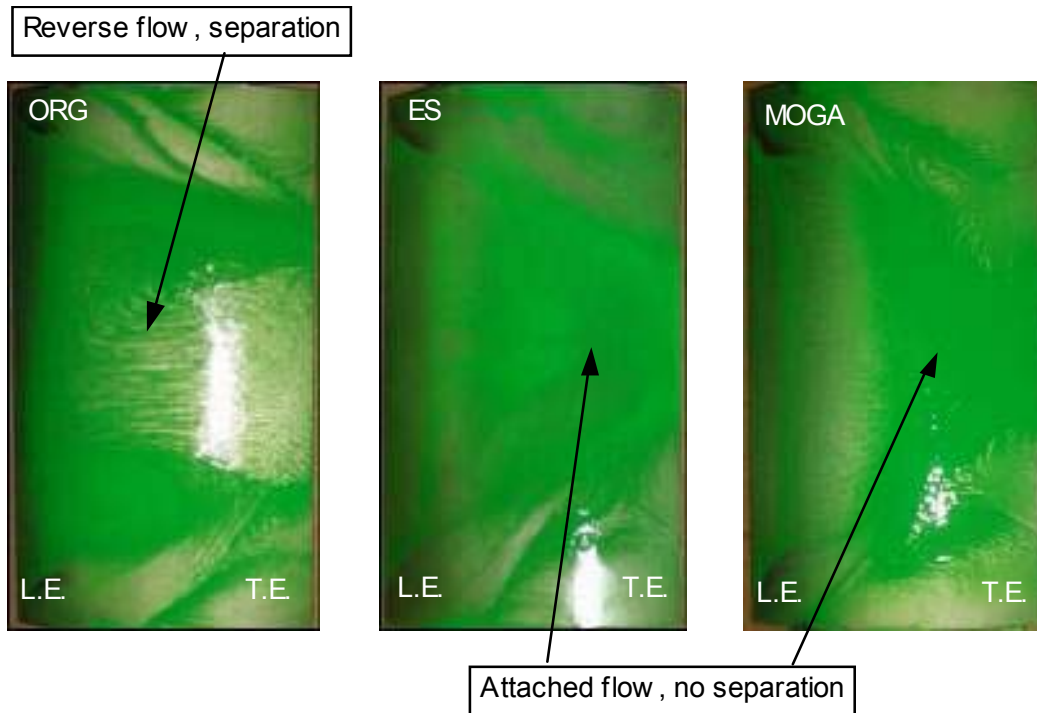


Figure 27 Blade suction surface flow visualization at the design condition

Flowfield Characterization by CFD

Flowfield characterization by CFD provides additional view of the flow. The credibility of CFD can be ascertained from the agreement between experimental and CFD results, as shown where the comparison is made in the following sections of this chapter.

Figure 28-30 shows the contours of Mach number, total pressure loss coefficient and vectors of Mach number at the design condition for the three blades respectively. These figures exhibit the flow structure, loss generation and transport, and boundary layer development. It is seen that a typical supersonic patch for a supercritical blade is formed at the front part of each blade on the suction side, terminated by a passage shock at about 20% chord. Right after the passage shock, boundary layer separation commences for the baseline blade while no separation occurs for the optimized blades. These results agree with the experimental results of wake profile and blade surface visualization shown in Figure 26 and 27.

Further examination of the supersonic patches reveals differences between the three blades. For ORG, flow accelerates around the leading edge first, after a deceleration,

re-accelerates to a higher velocity. The high velocity region is terminated by a strong shock (bowed in shape, with higher intensity near the blade surface), which initiates boundary layer separation on the suction surface. The flow does not reattach afterwards, leading to considerable loss generation. The shock loss (at 20% chord) is much smaller in comparison with the boundary layer losses. Along the streamwise transportation process of the main flow, the shock loss is finally immersed into the big wake downstream due to the separated boundary layer, thus not observed in the wake profile.

ES has the highest velocity around the leading edge, causing a strong leading edge shock (visualized by shadowgraph as will be shown next). After the leading edge shock, the flow decelerates to the passage shock location. The leading edge shock hits the passage shock, generating an interaction in the outer mainstream (causing higher shock intensity) while lessening the passage shock intensity near the blade surface. The adverse pressure gradient from this lessened shock reduces the possibility of shock-induced boundary layer separation. As exhibited by the Mach number vector, the flow maintains attached along the blade suction surface to the trailing edge, thus the wake and losses of ES are much smaller than ORG. The shock loss (at 20% chord) is transported with mainstream and still visible downstream of the cascade. This accounts for the small hump in the wake profile of ES, as seen in Figure 26. MOGA has similar flow pattern as ES, except for the leading edge acceleration is not that strong to reach the passage shock. The shock loss, which is lower than ES, is smeared out in the downstream region. That's why MOGA has slightly lower overall losses than ES.

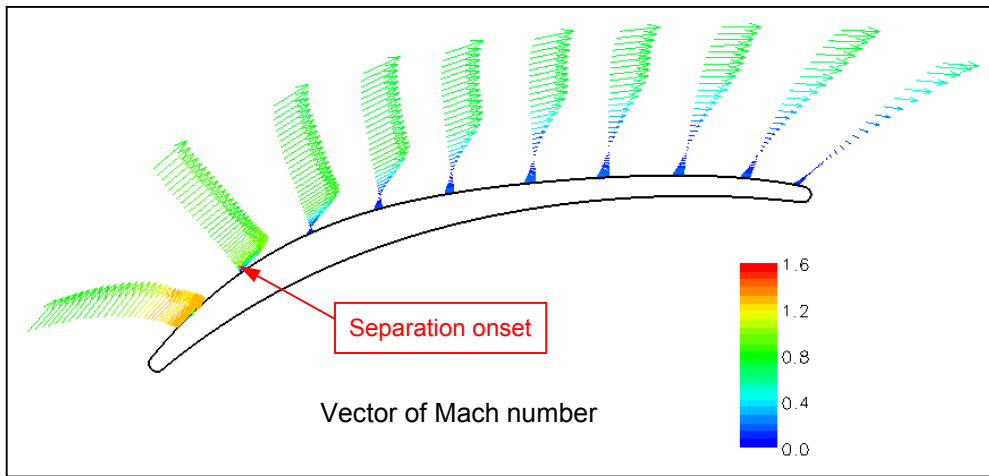
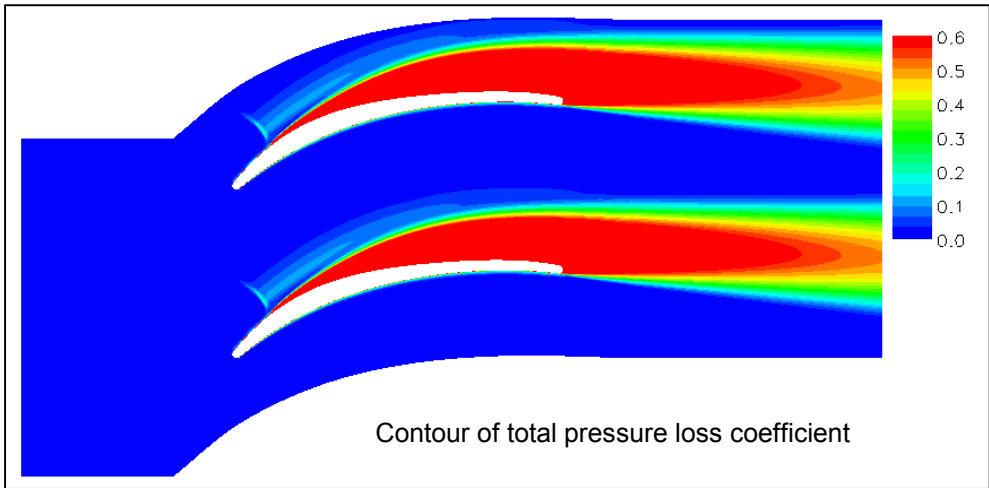
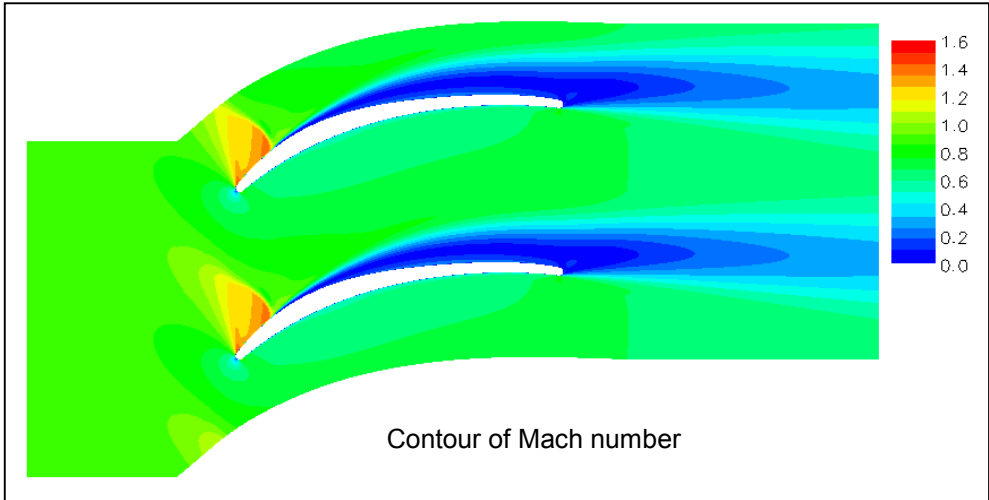


Figure 28 CFD flowfield characterization at the design condition - ORG

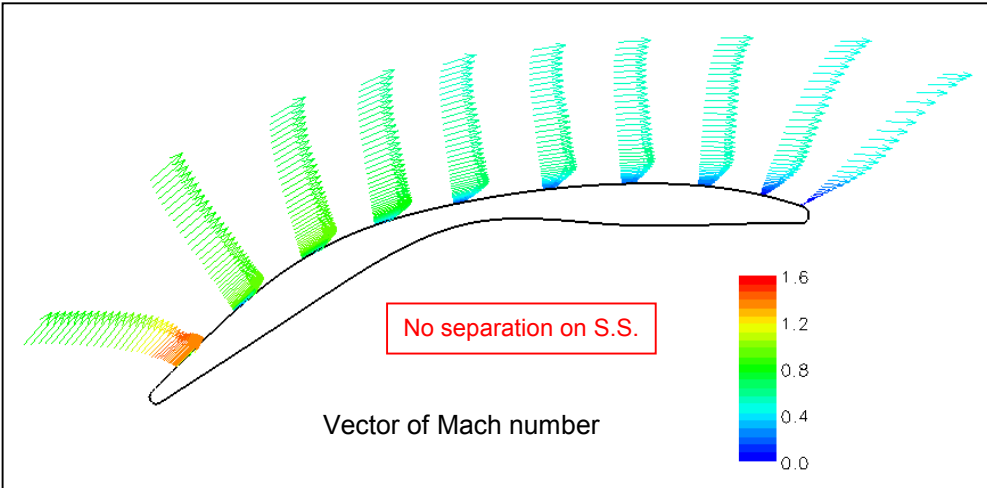
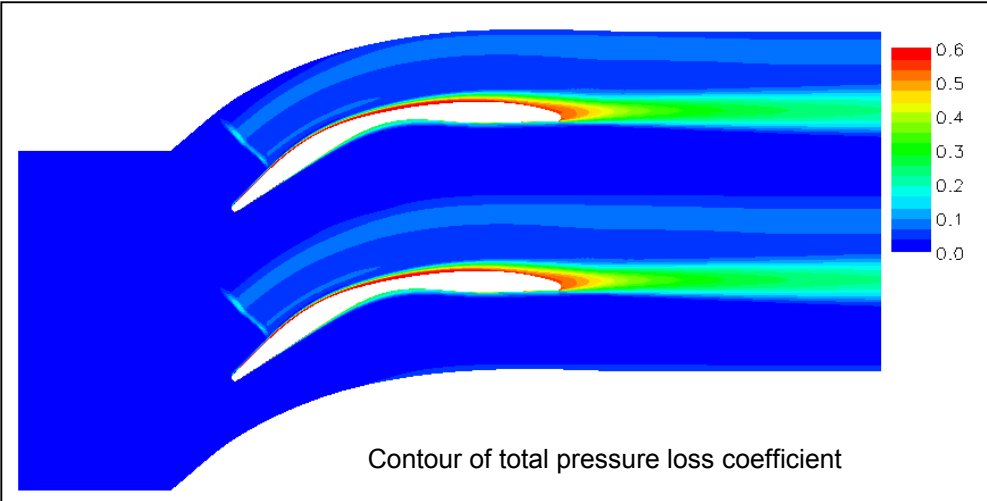
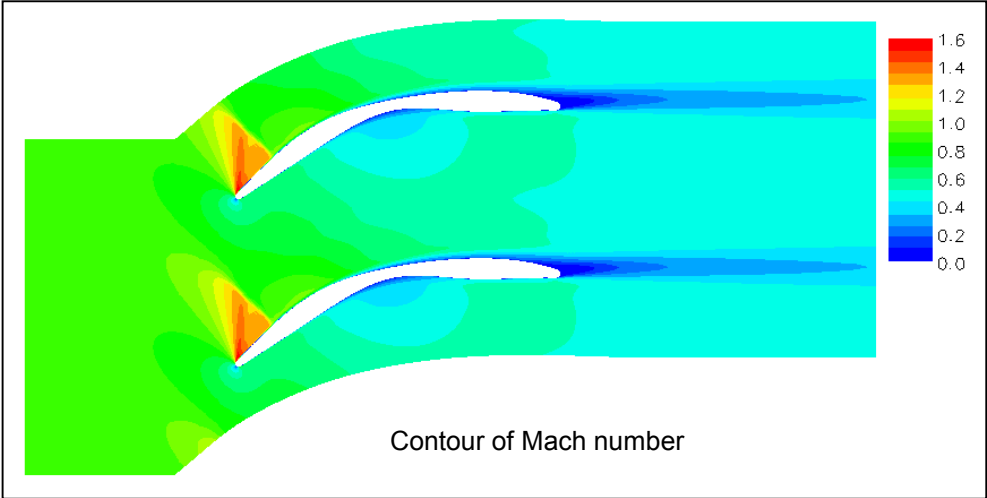


Figure 29 CFD flowfield characterization at the design condition - ES

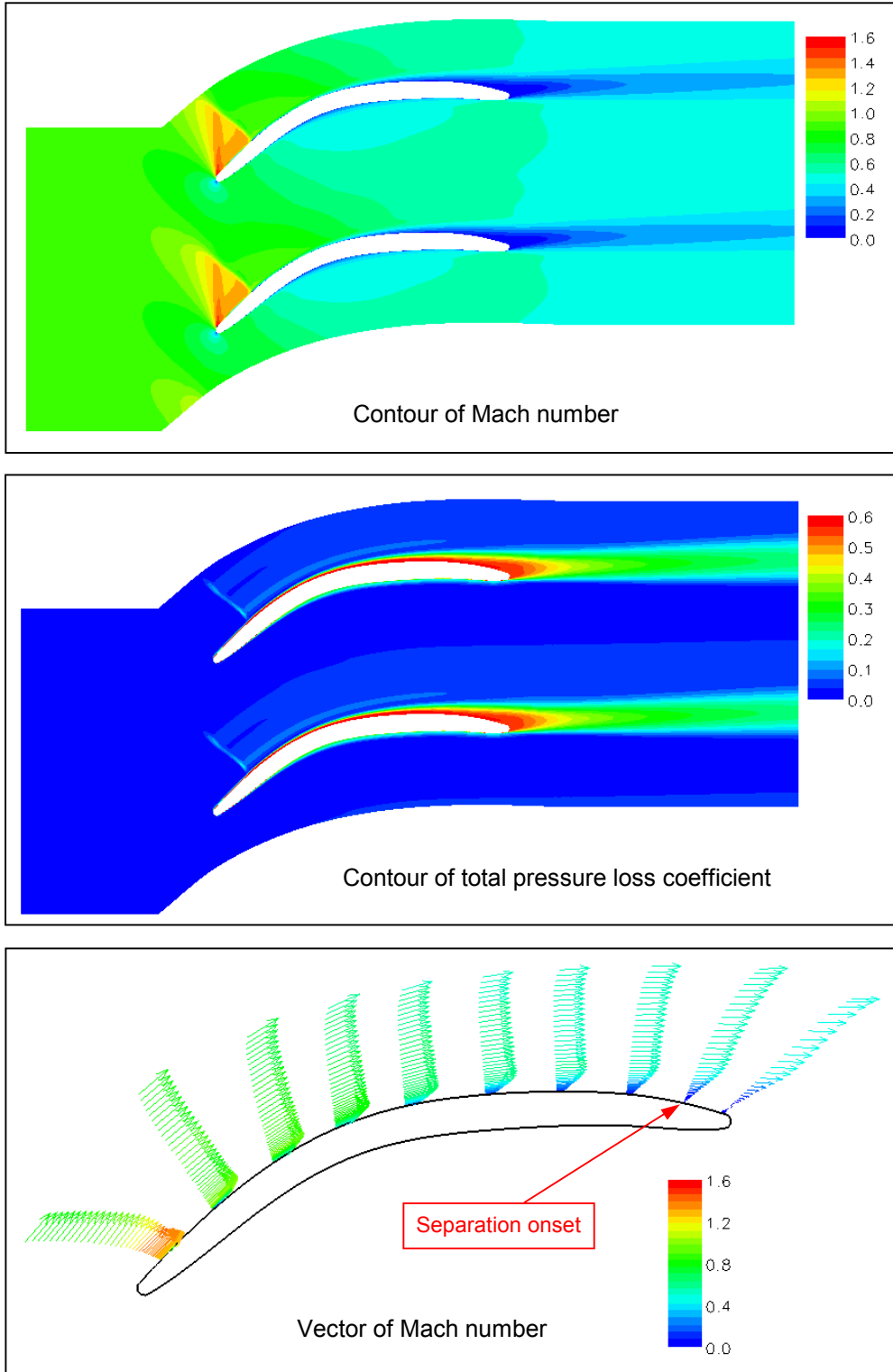
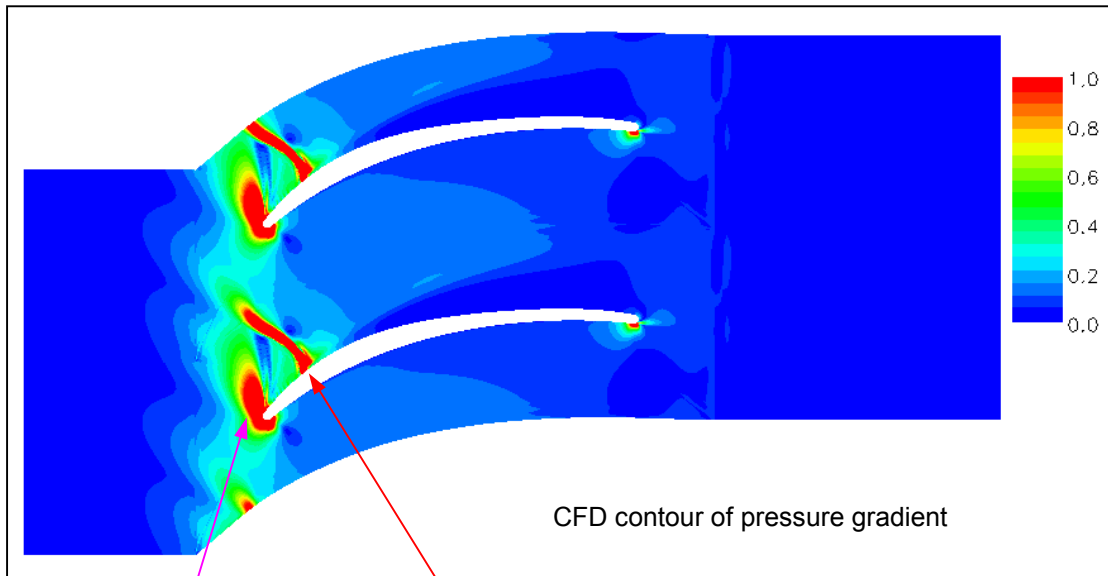


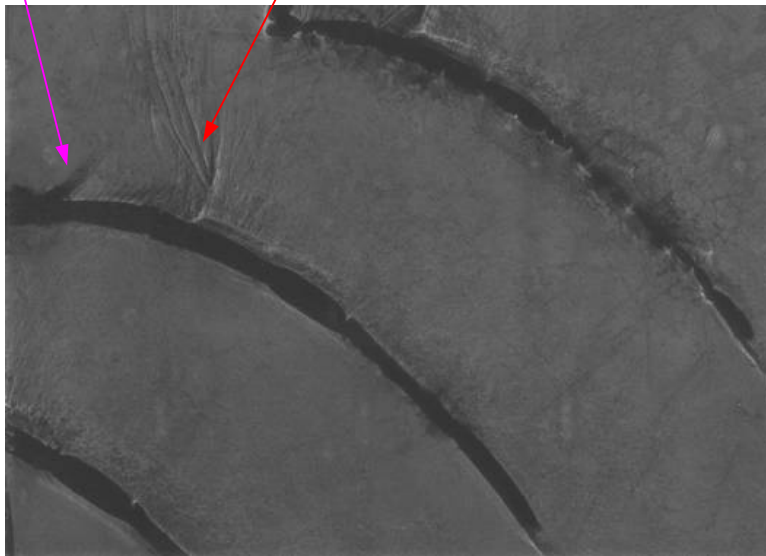
Figure 30 CFD flowfield characterization at the design condition - MOGA

To better manifest the shock patterns, Contours of pressure gradient from CFD results are shown in Figure 31-33. Shadowgraphs were taken in the experiments and are also shown in Figure 31-33 for comparison with the CFD results. It is seen that good agreement between experimental and CFD results has been obtained, in terms of not only the shock pattern and location, but also the shock shape (bowed for ORG and straight for ES and MOGA). This agreement provides a strong evidence for the credibility of the CFD flow characterization of the current work.



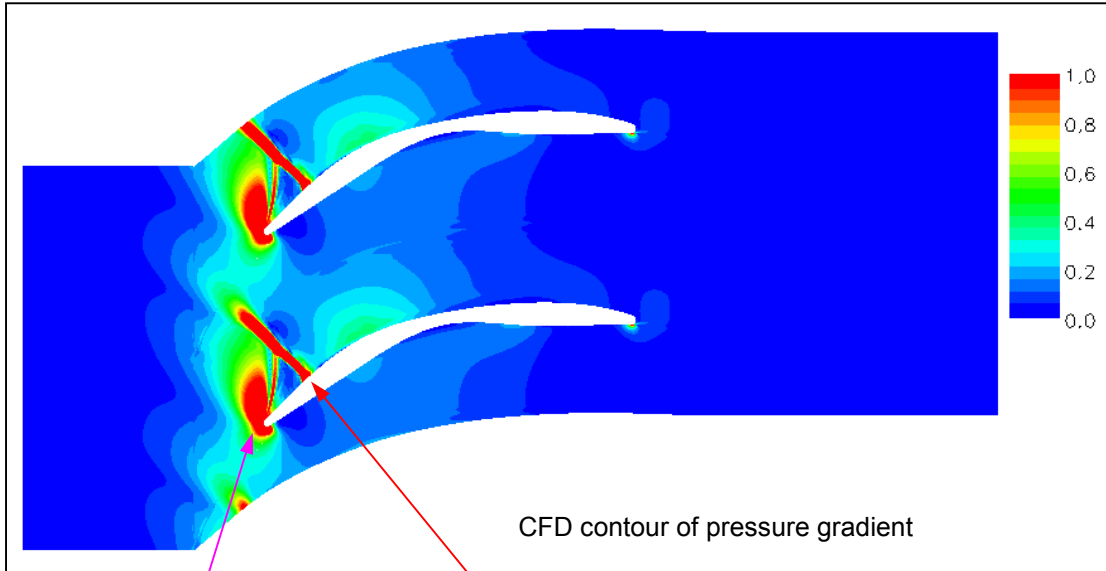
Leading edge shock

Passage shock - bowed



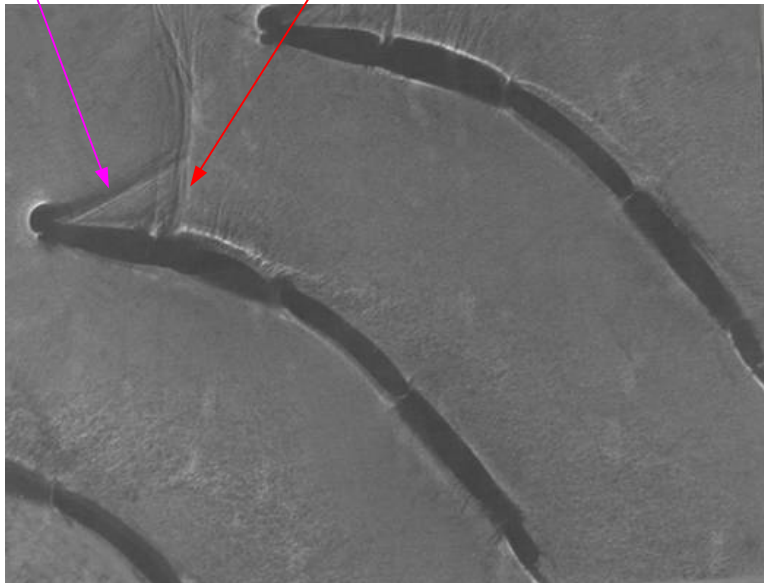
Experimental shadowgraph

Figure 31 Shock pattern at the design condition - ORG



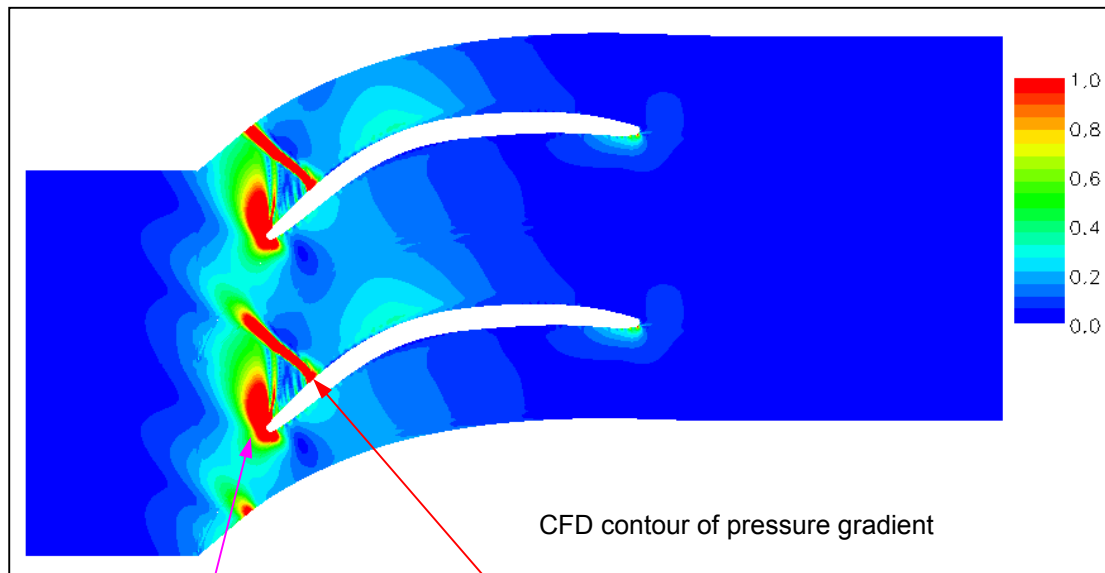
Leading edge shock

Passage shock - straight



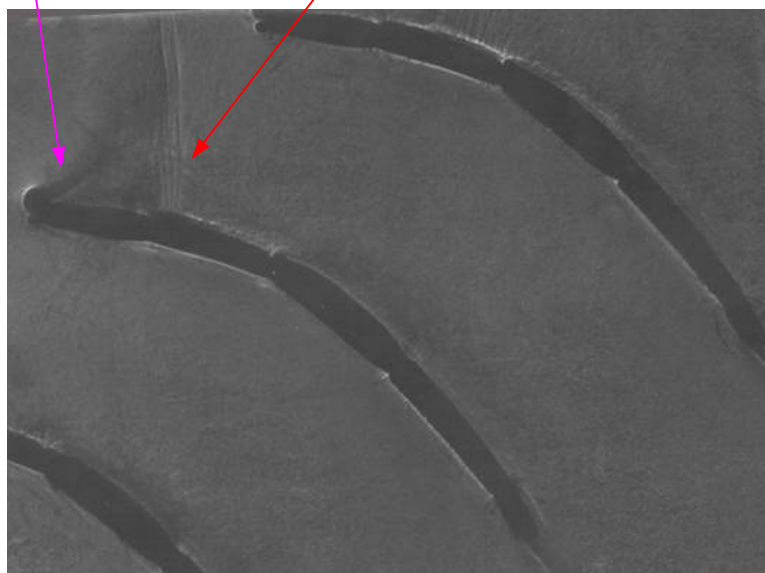
Experimental shadowgraph

Figure 32 Shock pattern at the design condition - ES



Leading edge shock

Passage shock - straight



Experimental shadowgraph

Figure 33 Shock pattern at the design condition - MOGA

For ORG, the leading edge shock is weak such that it does not reach the passage shock. The leading edge shock is visible from the experimental shadowgraph but more difficult to see from CFD results. The passage shock has higher strength near the blade surface, making it more likely for the boundary layer to separate. For ES, two shocks are clearly exhibited and the leading edge shock hits the passage shock. The shock pattern of MOGA is closer to ES than ORG, but the leading edge shock is not that strong to reach the passage shock.

It can be concluded from the above results that the loss reduction from the baseline blade to the optimized blades is due to the different boundary layer behaviors (separated or not). CFD contours of pressure gradient as shown in Figure 31-33 provided further understanding about why the baseline has severe separation but the optimized blades have not. In addition to the different blade front part acceleration and re-acceleration patterns, as well as different shock patterns (the strength of the passage shocks of the optimized blades are lessened, especially near the blade surface), the pressure gradient distribution across the blade plays another important role, as discussed below.

The effect of pressure gradient of the blade suction surface on the boundary layer development is revealed by Figure 34. The pressure (P_s) used in the figure is the normalized value by the inlet total pressure. The magnitude of the pressure gradient (P_s Grad. Mag.) used in the figure is based on the normalized P_s . For ORG, high adverse pressure gradient near the blade surface due to the highest blade curvature at ~20% chord coincides right after the shock (substantial adverse pressure gradient), thus these two driving factors induced boundary layer separation and the flow never re-attached towards the trailing edge. It is seen that due to the front-part highly cambered (thus front-part highly loaded) blade shape, ORG fulfills diffusion within first 30% chord, typical characteristics for CDA blade with good performance at normal supersonic flow conditions ($M_1 = 0.6-0.8$). However, the current work has demonstrated that it is not suitable for higher supersonic flow conditions ($M_1 = 0.87$) due to the strengthening and location of the passage shock.

Unlike ORG, ES and MOGA both have the highest blade curvature at 30-40% chord, thus the corresponding high adverse pressure gradient occurs more downstream,

away from the passage shock. Right after the shock, there is even an acceleration (favorable pressure gradient) near the blade surface, re-energizing the surface flow. Consequently, boundary layer does not separate right after the shock and after the re-acceleration (25% chord), the flow is able to overcome the adverse pressure gradient due to the highest curvature (30-40% chord) and avoid separation, followed by a gradual diffusion towards the trailing edge. It is seen that the key for the optimized blades to maintain well-controlled boundary layer development and diffusion is the near mid-chord highly cambered (35% instead of 20% chord) blade shape. This is probably an important indication found from the current study for developing highly cambered compressor blades at higher supersonic flow conditions ($M_1 = 0.8-0.95$).

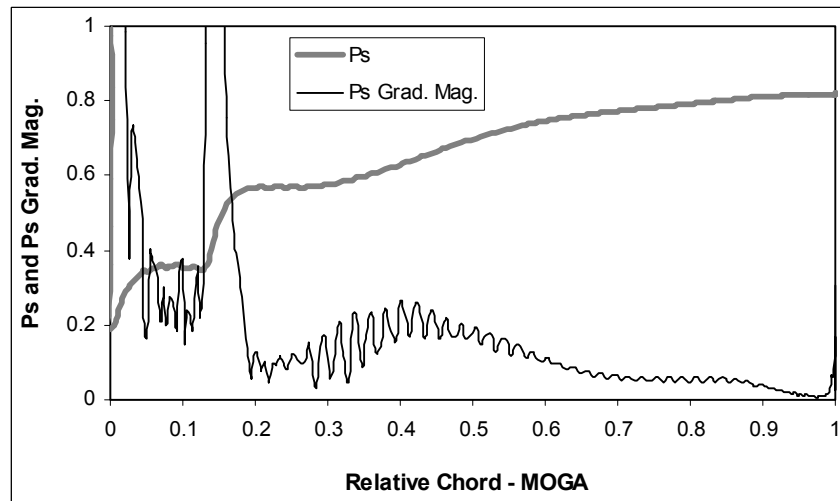
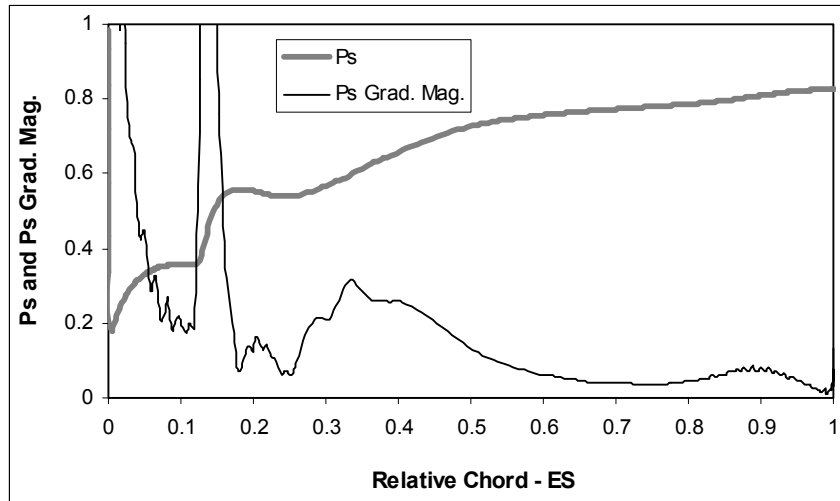
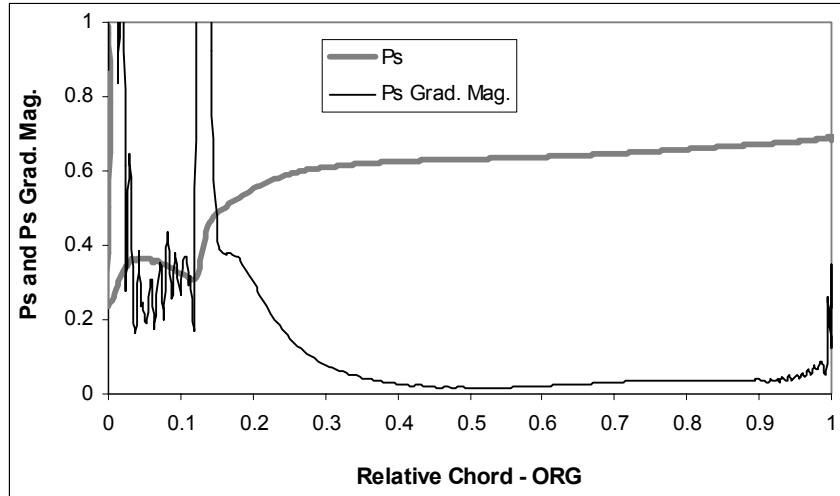


Figure 34 CFD pressure and pressure gradient magnitude on the blade suction surface at the design condition

3.2 Cascade Performance and Flow Physics at the Design Inlet Flow Angle

Cascade tests were conducted for the three blades at the design inlet flow angle ($\alpha_1 = 48.4^\circ$) for different inlet Mach numbers, using solid sidewall. Both experimental and numerical results of losses, static pressure ratio and exit flow angle are presented. The associated flow physics is discussed as well.

3.2.1 Losses

The development of losses with inlet Mach number at the design inlet flow angle was investigated experimentally and numerically. As shown in Figure 35, both experimental results (solid sidewall tests) and CFD (2-D steady Navier-Stokes solutions) show significant loss reduction at high inlet Mach numbers ($M_1 > 0.83$) from the baseline blade to the optimized blades. At the design condition ($M_1 = 0.87$), experimental results show about 30% loss reduction. Both experiment and CFD obtained similar loss development trend with increasing inlet Mach number. For ORG, low losses were maintained for a range of inlet Mach numbers less than 0.83, which is the normal characteristic of a CDA blade. With further increasing inlet Mach number to higher supercritical flow conditions ($M_1 > 0.83$), losses increase abruptly, leading to much elevated losses at the design condition. In contrast, losses of the optimized blades keep low losses at higher supercritical flow conditions ($M_1 = 0.83 - 0.91$), providing a robust envelope around the design condition.

Comparing the two optimized blades, MOGA even gives slightly lower losses than ES for all the tested inlet Mach numbers according to experimental data. But CFD did not predict this slight difference. The reason for this slight loss difference is probably due to the thinner boundary layer for low Mach numbers and less shock loss for high Mach numbers of MOGA. As discussed earlier in Section 3.1.3, ES has a small loss hump in the wake profile due to the strong double shock interaction. Therefore, although both ES and MOGA have well-controlled boundary layer from separation at higher supercritical flow conditions, MOGA excels in that it has better shock patterns thus less entropy generation at the blade front. Furthermore, considering the shapes of the two blades, which are obtained from aerodynamic design using different optimization

methods, MOGA is preferred as it has much smoother blade thickness distribution along chord, superior from the standpoint of mechanical design.

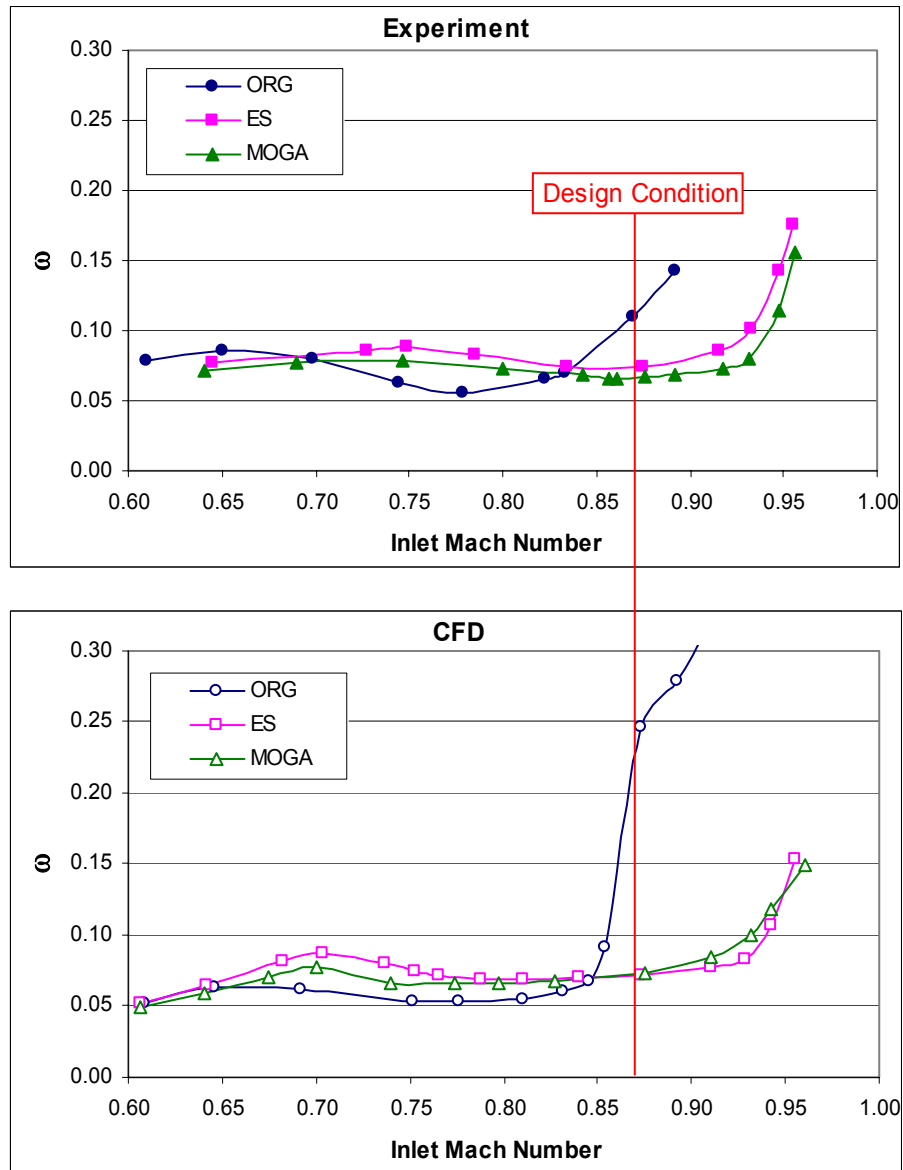


Figure 35 Loss development with inlet Mach number at the design inlet flow angle (48.4°)

Comparing the experimental and CFD results shown in Figure 35, good agreement is seen in terms of ω - M_1 development trend and loss values of the three blades, except that CFD over-predicted the losses of ORG at higher supersonic flow conditions,

where severe boundary layer separation occurred. To better view the comparison between the experimental and CFD results, the same data shown in Figure 35 were re-plotted in Figure 36.

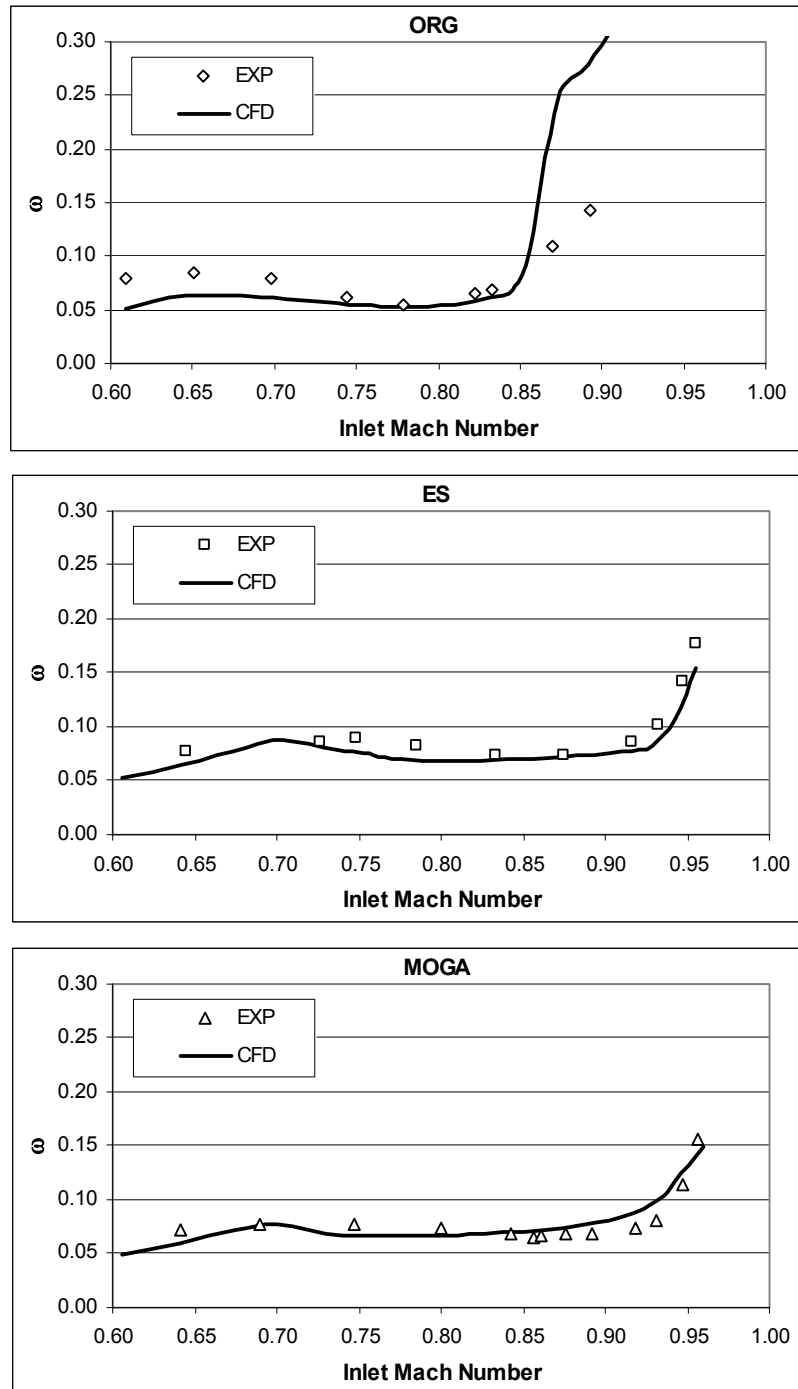


Figure 36 Comparison of experimental and CFD losses at the design inlet flow angle (48.4°)

3.2.2 Effect of Reynolds Number

As mentioned earlier in Section 2.3.1, the tunnel facility cannot allow independent Reynolds number control, thus the Reynolds number varied for a range of $1.15 - 1.8 \times 10^6$ with increasing inlet Mach number in the experiments. This relatively small Reynolds number variation at a higher Reynolds number range should be of negligible influence on the flow and blade performance. Previous research has shown that the critical Reynolds number range lies below 3×10^5 [4], as shown in Figure 37. The Current experiment is well beyond this range.

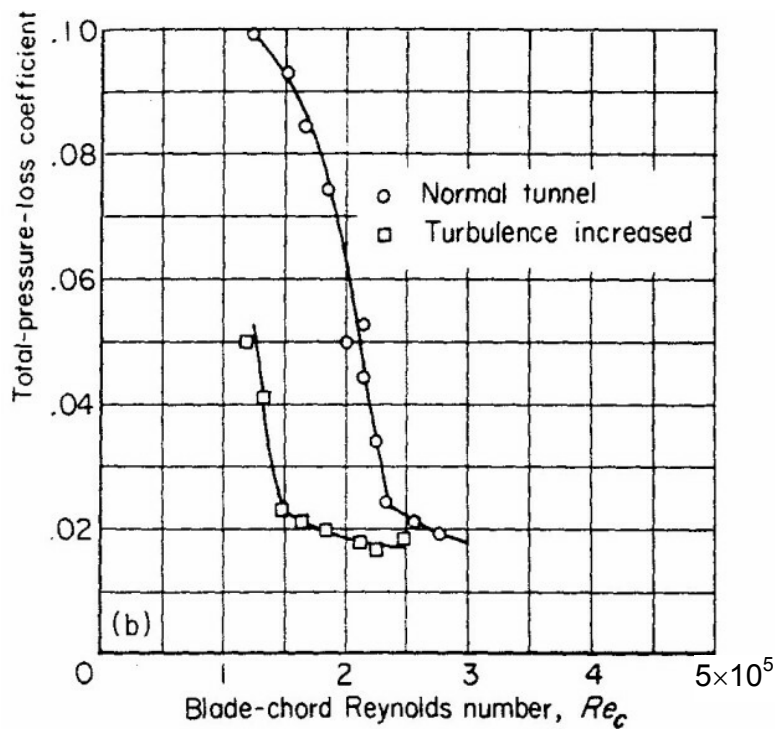


Figure 37 Effect of Reynolds number on compressor cascade losses

It should be pointed out that the CFD results in Figure 36 were obtained with matching the experimental Reynolds number variation. To check the sensitivity of CFD results to the Reynolds number variation in the experimental range, another set of loss results was obtained from CFD by keeping a constant $Re=1.6 \times 10^6$ while increasing inlet Mach number. As shown in Figure 38, the solid lines are the same CFD results used in Figure 36 which represent the experimental Reynolds number variation; the symbols are

CFD results with the constant Reynolds number of 1.6×10^6 . There is nearly no difference between the two sets of loss results, indicating that it does not matter using either way to simulate the Reynolds numbers in the current work.

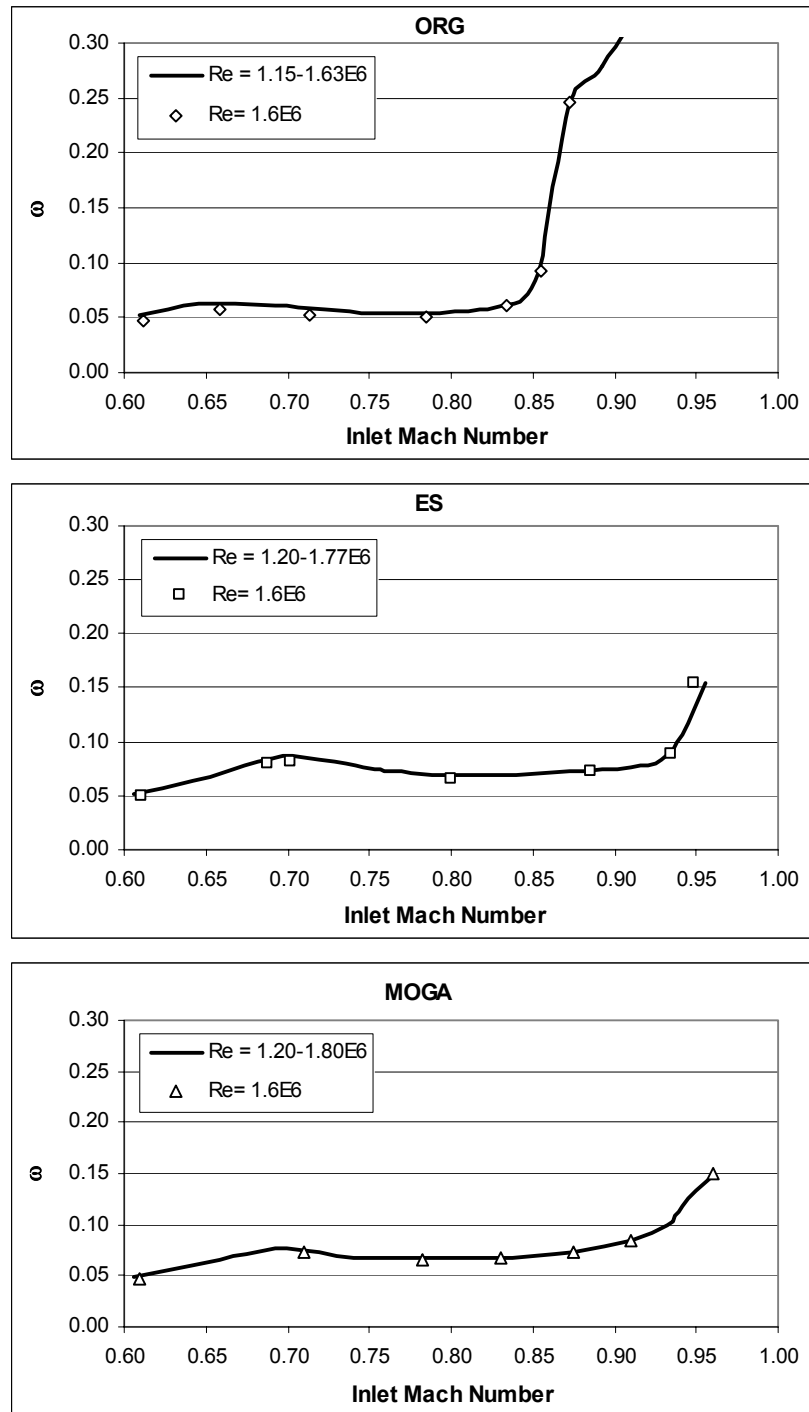


Figure 38 Effect of Reynolds number on losses checked by CFD (48.4°)

3.2.3 Pressure Ratio and Exit Flow Angle

Experimental and CFD results of static pressure ratio for the three blades are shown in Figure 39. It is seen that the pressure ratio simply increases with increasing inlet Mach number. The three blades have similar pressure rise for most of the tested Mach number range except around the design condition ($M_1 = 0.87$), where ES and MOGA have higher pressure rise than ORG. This agrees with the loss characteristics shown in Figure 35. Due to the boundary layer separation, ORG has less diffusion, thus lower pressure ratio. The trend of the pressure rise development with inlet Mach number was predicted well by CFD except for some over-prediction at higher supercritical flow conditions ($M_1 > 0.8$). Close to the design inlet Mach number, in agreement with the over-prediction of the losses (see Figure 36), CFD predicted much lower pressure rise for ORG.

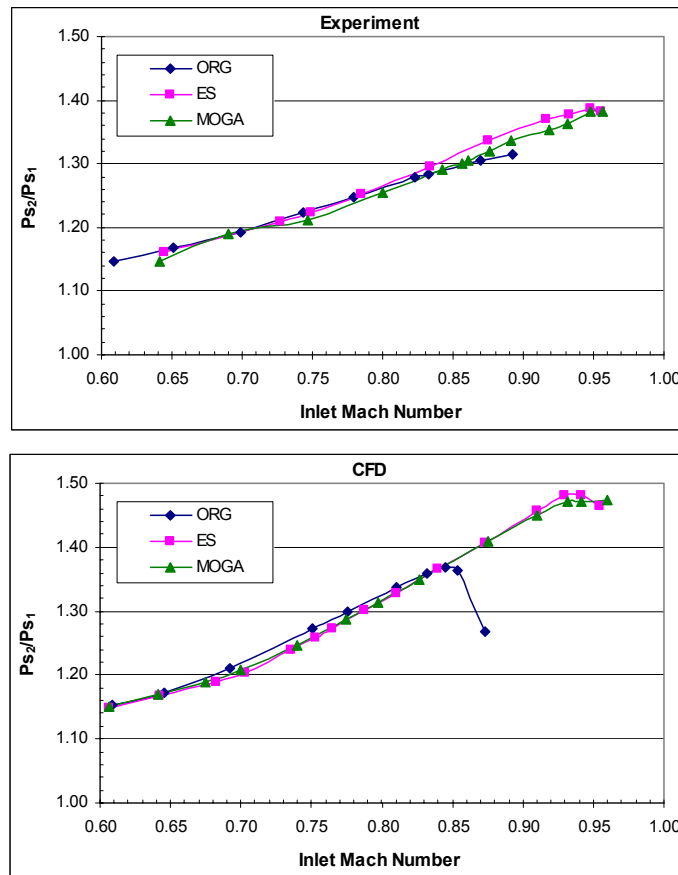


Figure 39 Static pressure ratio at the design inlet flow angle (48.4°)

Experimental and CFD results of exit flow angle for the three blades are shown in Figure 40. It is seen that the exit flow angles of the three blades decrease with increasing inlet Mach number, meaning higher flow turning was obtained near the design condition, which was desirable. In general, ES has flow turning 2.5° lower than ORG and MOGA has 2° lower flow turning than ES. Comments on the under-turning of the optimized blades have been made at the design condition in Section 3.1.2. The relative difference of exit flow angle was correctly predicted by CFD, but CFD generally obtained 2° smaller exit flow angles than experiments.

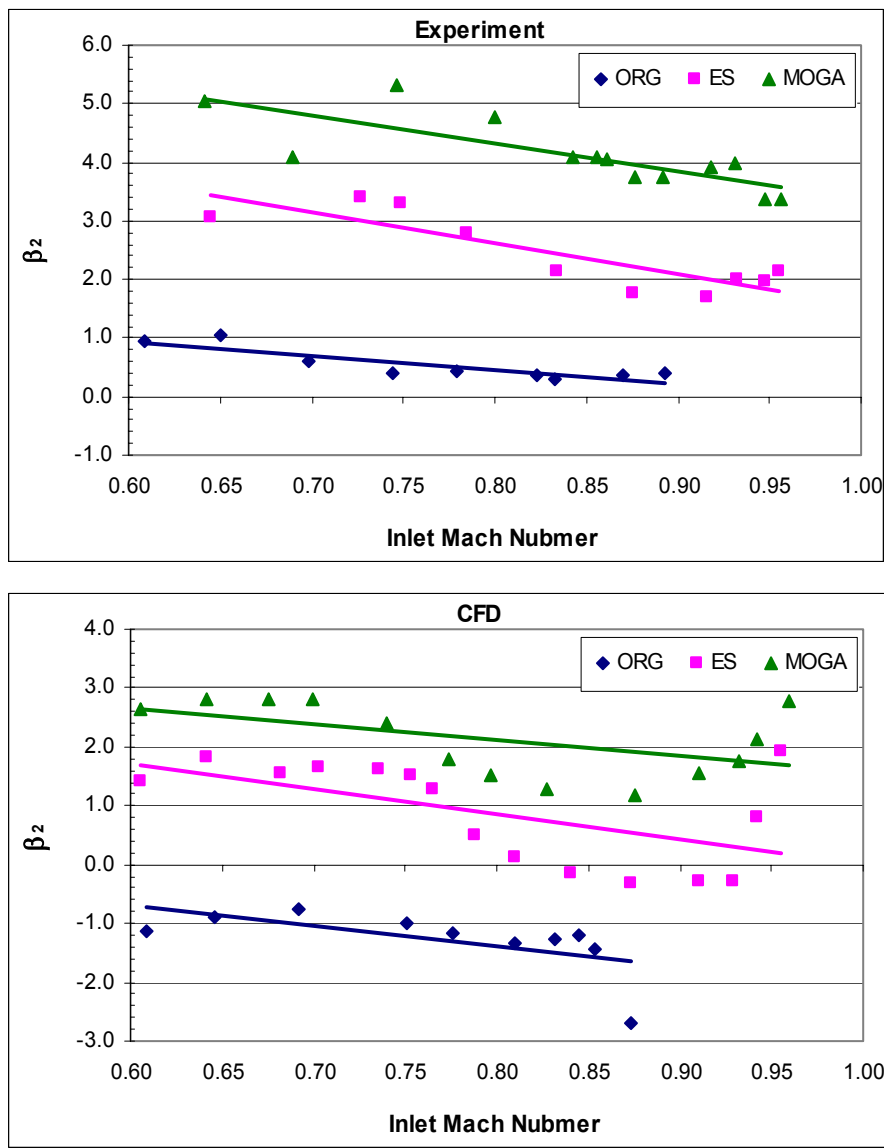


Figure 40 Exit flow angle at the design inlet flow (48.4°)

3.2.4 Blade Surface Mach Number and CFD Flowfield Contour

Blade surface isentropic Mach number (M_{is}) distribution provides a good perspective of the flow and has been widely used in the research area of cascade flow. Its definition is given by Equation 4.

$$M_{is} = \sqrt{\frac{2}{0.4} \cdot \left[\left(\frac{Pt_1}{P_{S_s}} \right)^{\frac{0.4}{1.4}} - 1 \right]} \quad \text{(Equation 4)}$$

Figure 41 shows experimental and CFD results for ORG. At $M_1 = 0.75$, ORG has normal CDA performance, i.e., continuous diffusion along the whole suction surface without boundary layer separation and nearly constant subsonic Mach number on the pressure surface. This Mach number distribution trend looks similar to that of Elazar and Shreeve [57]. But it is different from the typical CDA trend [50] in that there is no continuous acceleration from the leading edge up to 20% chord, referred to as the “ski-jump” [77]. Cumpsty and Dong questioned Elazar and Shreeve about this difference in the discussion of [57]. It was answered in the current work in that it was the incidence that changed the blade surface Mach number distribution trend. As will be shown in the next section, the typical CDA blade surface Mach number distribution (the “ski-jump”) was obtained at an off-design incidence angle (inlet flow angle 45.4°) for ORG.

Increasing M_1 to 0.84-0.91 results in a change of the flow pattern. After deceleration from the leading edge velocity peak, the flow accelerates to a second velocity peak (around 20% chord). Right after the second velocity peak, signs of the passage shock and the subsequent boundary layer separation can be recognized. As M_1 increases from 0.84 to 0.91, the second acceleration becomes stronger, resulting in stronger passage shock. Consequently, severer boundary layer separation is initiated, leading to elevated losses.

The quantitative agreement between CFD and experiment is not good although they both revealed the same flow behavior development with increasing inlet Mach number. The reasons are due to the AVDR effect and inaccurate prediction of the degree of the boundary layer separation. It is noticed that the agreement in losses are relatively better (Figure 36) except for the separated flow cases. This is because blade surface Mach

number is more sensitive to the AVDR influence than losses. See Appendix A for detailed discussion, including previous research review on this issue.

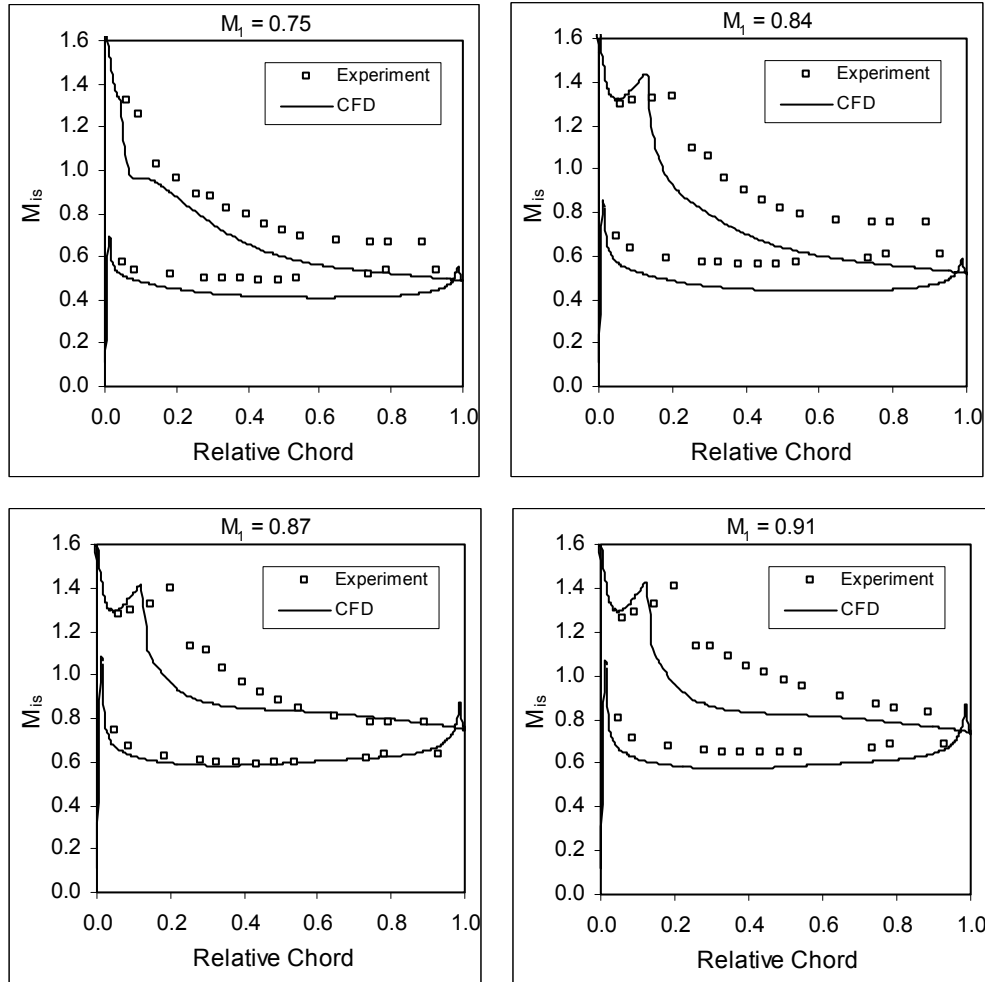


Figure 41 Blade surface Mach number at design inlet flow angle - ORG

The flow characteristics in Figure 41 are further visualized by CFD flowfield characterization at $M_1=0.75$, 84, 91, shown in Figure 42, 43, 44 respectively. CFD contours for $M_1=0.87$ have been shown earlier in Section 3.1.3. It is seen that with increasing M_1 , the shock is strengthened, leading to initiation of the boundary layer separation around $M_1=0.84$. At higher supersonic flow conditions ($M_1=0.87$, 0.91), the severe boundary layer separation are clearly exhibited (actually over-predicted).

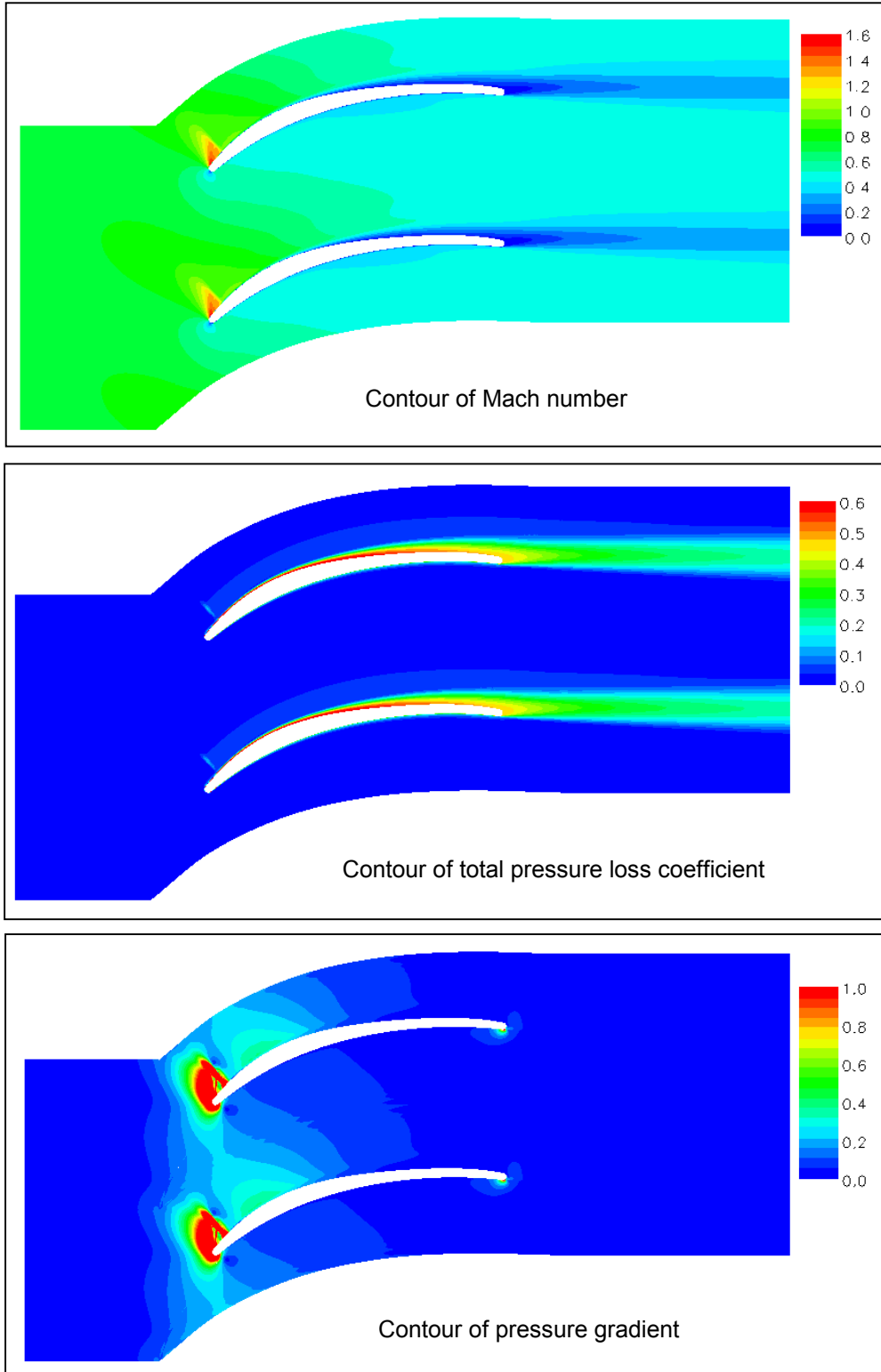


Figure 42 CFD flowfield characterization at design inlet flow angle (ORG $M_1=0.75$)

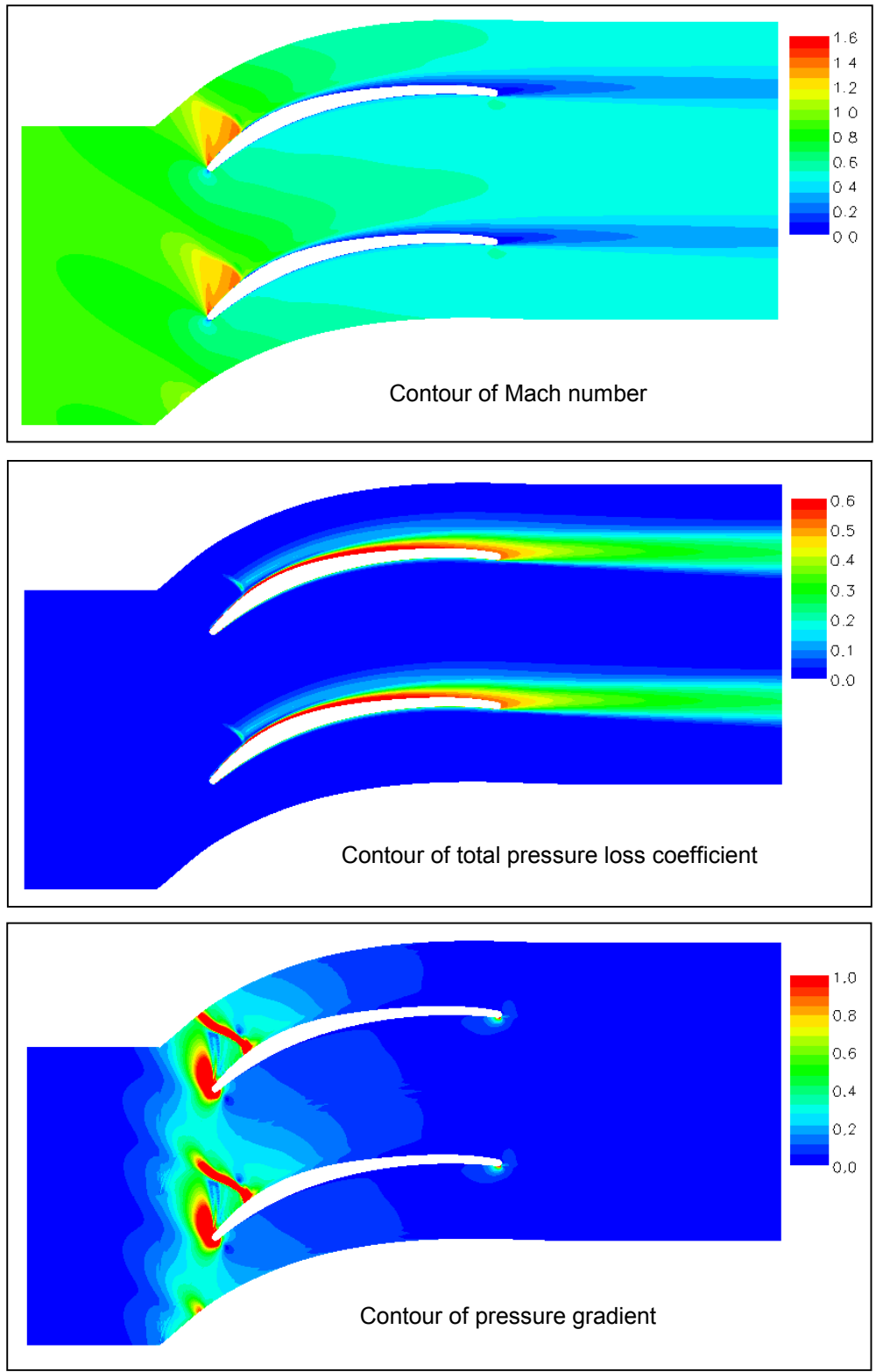


Figure 43 CFD flowfield characterization at design inlet flow angle (ORG $M_1=0.84$)

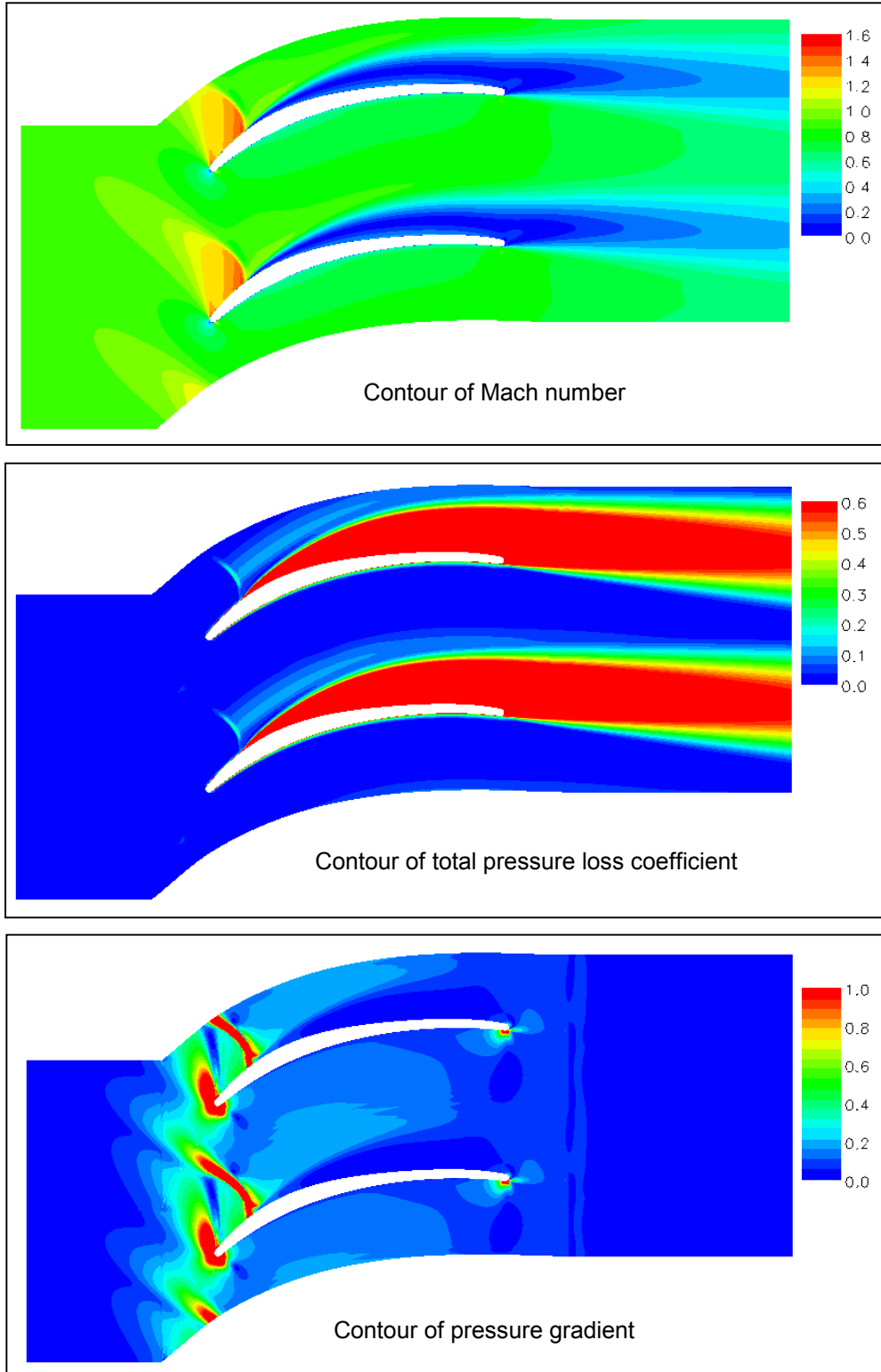


Figure 44 CFD flowfield characterization at design inlet flow angle (ORG $M_1=0.91$)

Figure 45 and 46 show the results of blade surface Mach number for ES and MOGA respectively. It is seen that the flow behaviors of the optimized blades differ significantly from the baseline blade. First, surface Mach number varies on the pressure surfaces of the optimized blades, with a big depression near mid-chord. This distribution results in more even loading (the baseline blade is basically front-loaded). Second, stronger leading edge acceleration weakens the second acceleration (thus lessens the strength of the passage shock). Third, at higher supersonic flow conditions ($M_1 = 0.87$ and 0.91), although the passage shock exits, favorable pressure gradient follows the shock and the adverse pressure gradient is away from the shock (20% chord) to a more downstream location (30% chord). For all these reasons, there is no shock-induced boundary layer separation for the optimized blades, leading to much lower losses than ORG. Only when M_1 is elevated to a higher value like 0.94 or 0.95 , the blade front part velocity patterns of the optimized blades become similar to that of the baseline at $M_1=0.87$, and the passage shocks are now strong enough to initiate boundary layer separation, leading to abrupt loss rise. This is the mechanism for the optimized blades to extend low losses from normal supersonic flow conditions ($M_1=0.65-0.83$) to higher supersonic flow conditions ($M_1=0.84-0.91$).

Good agreement between CFD and experiment was obtained for low Mach numbers, as shown for ES at $M_1=0.75$ and MOGA at $M_1=0.68$. Increasing M_1 to 0.91 or higher value, the quantitative discrepancy enlarges due to stronger AVDR effect, leading to the up-shifting of experimental results compared to CFD curves. The flow behavior suggested by blade surface Mach number distribution is also exhibited by CFD flowfield characterization, as shown in Figure 47-52.

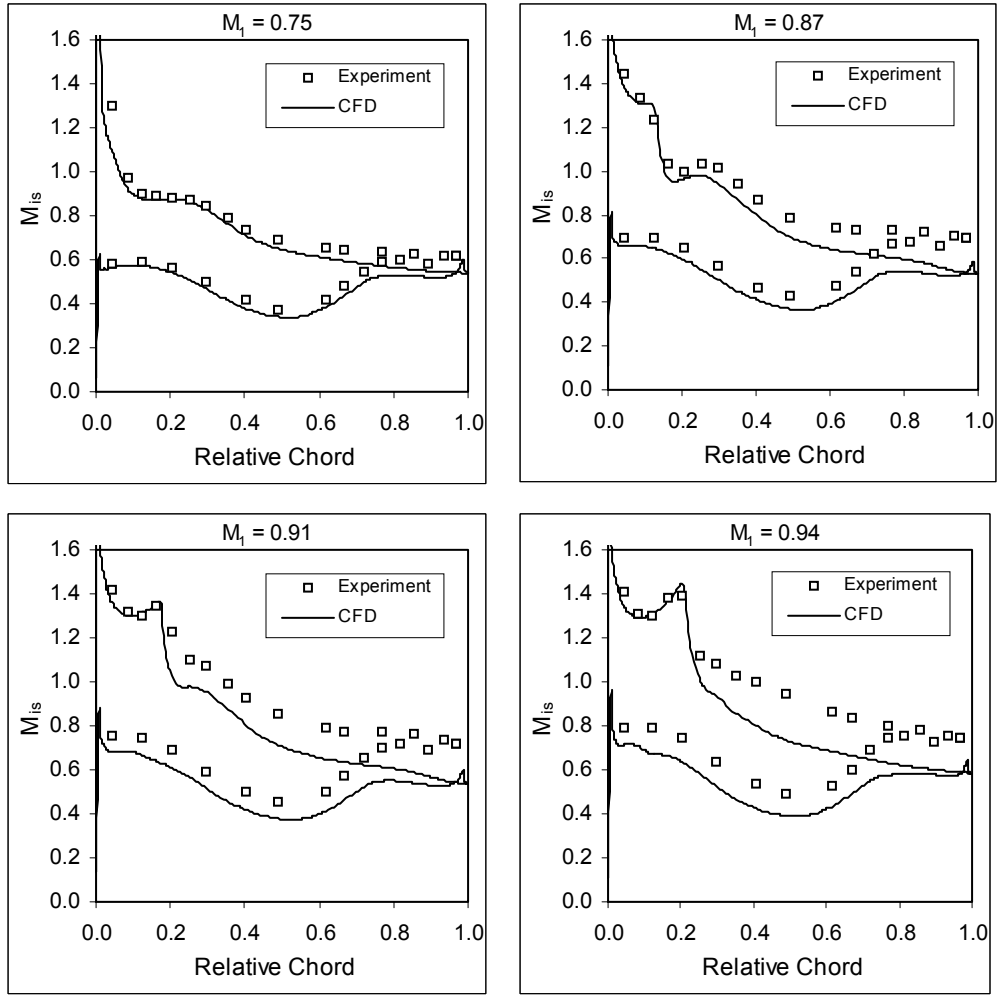


Figure 45 Blade surface Mach number at design inlet flow angle - ES

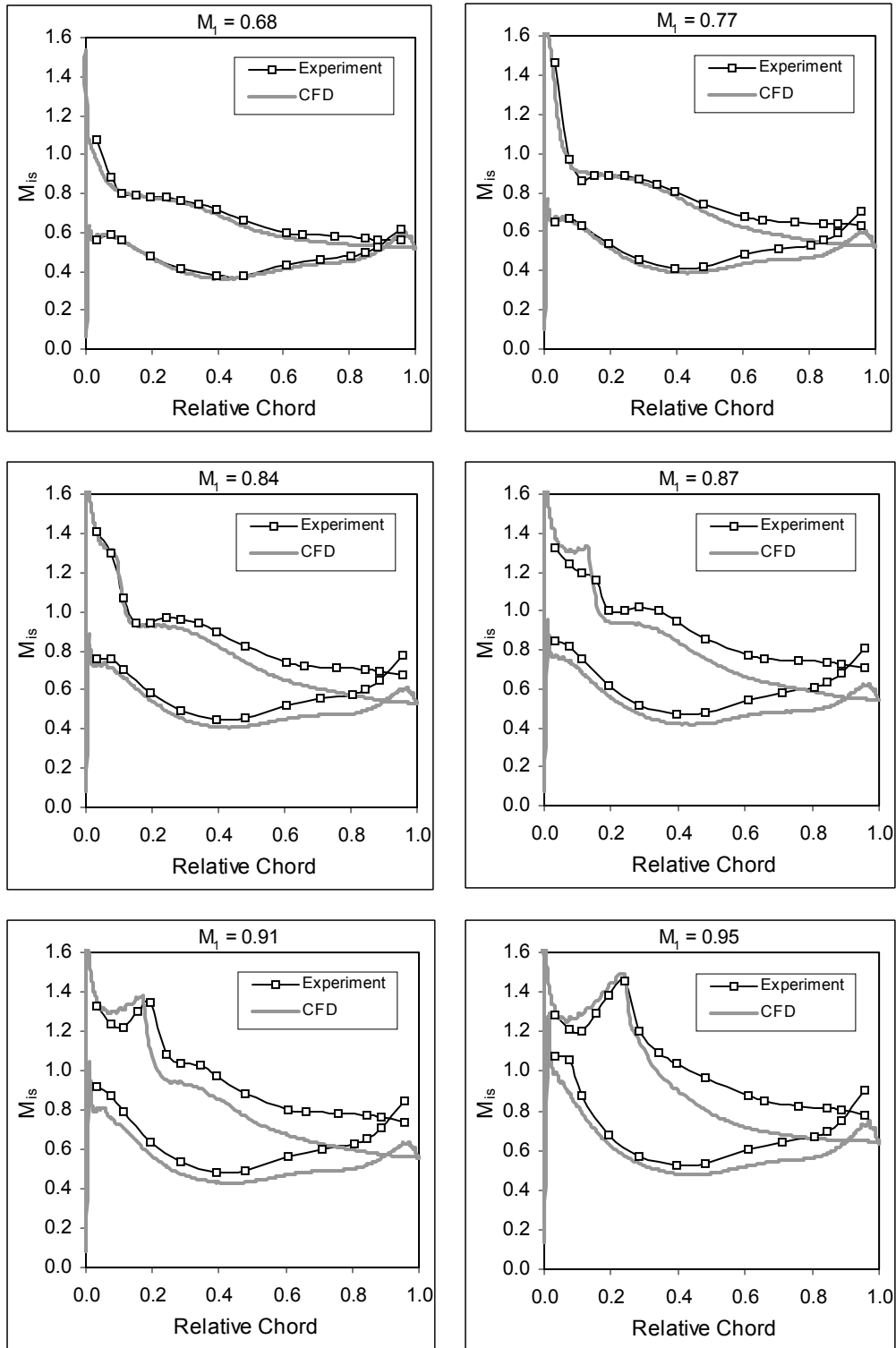


Figure 46 Blade surface Mach number at design inlet flow angle - MOGA

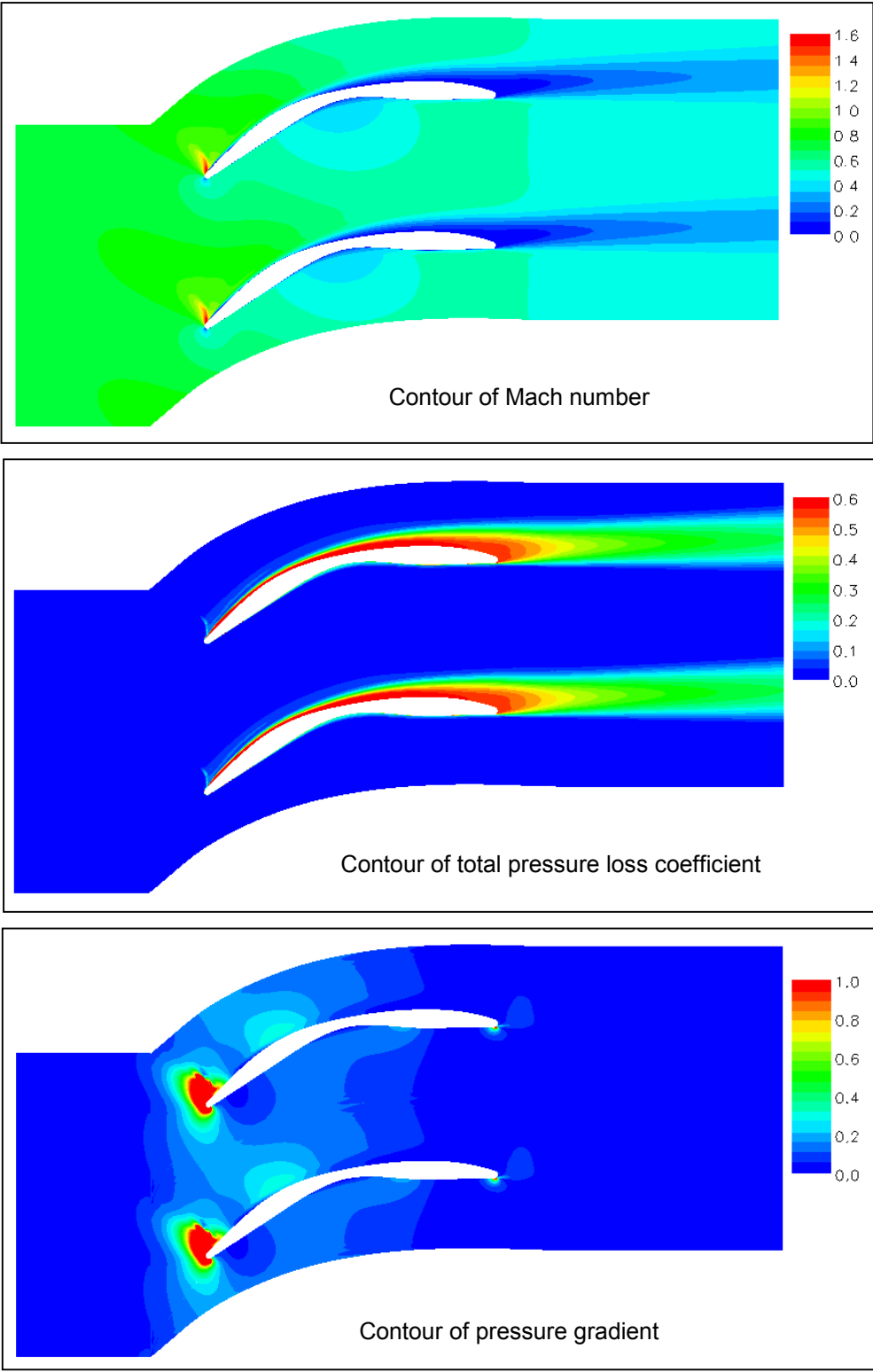


Figure 47 CFD flowfield characterization at design inlet flow angle (ES $M_1=0.75$)

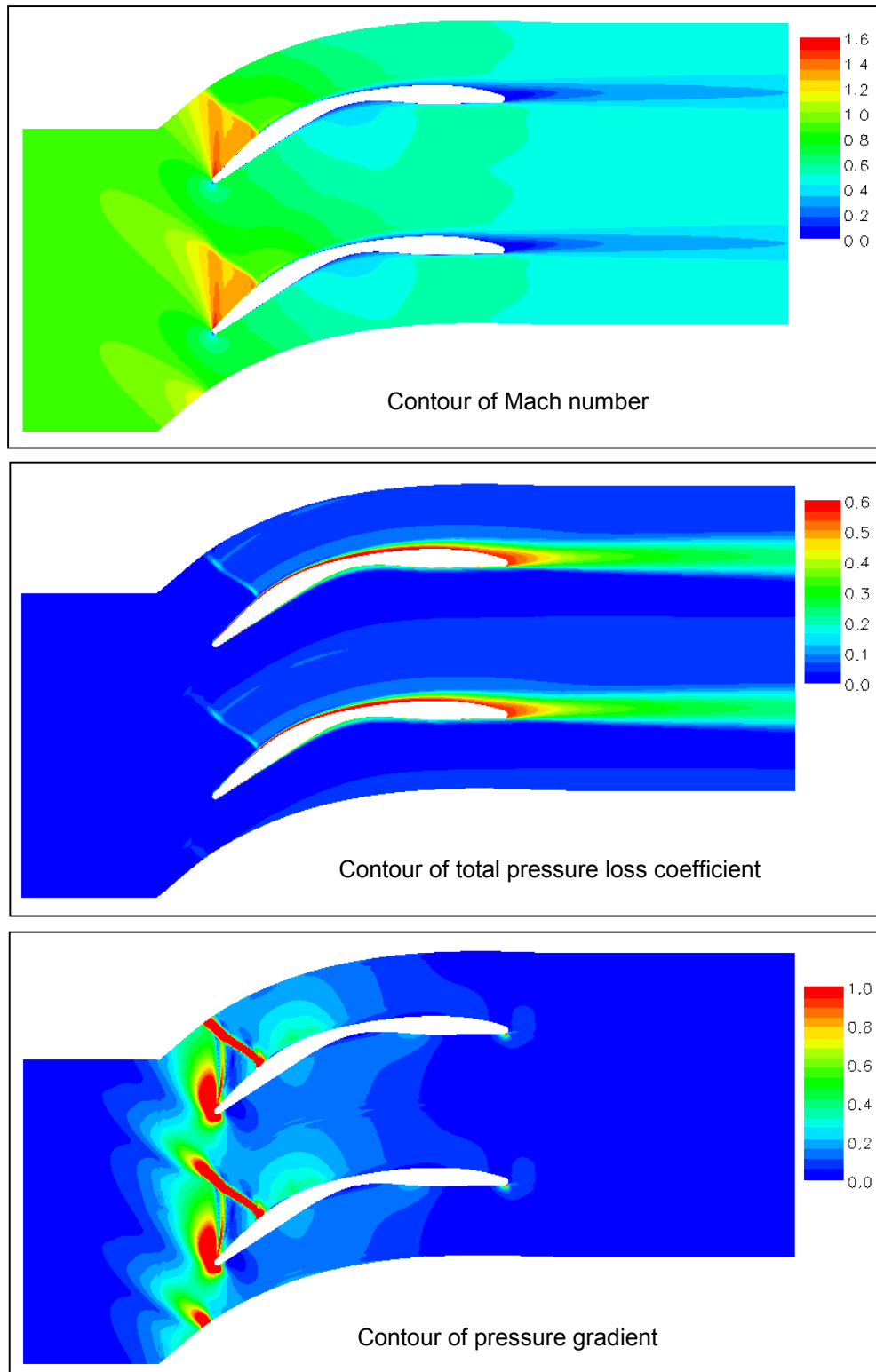


Figure 48 CFD flowfield characterization at design inlet flow angle (ES $M_1=0.91$)

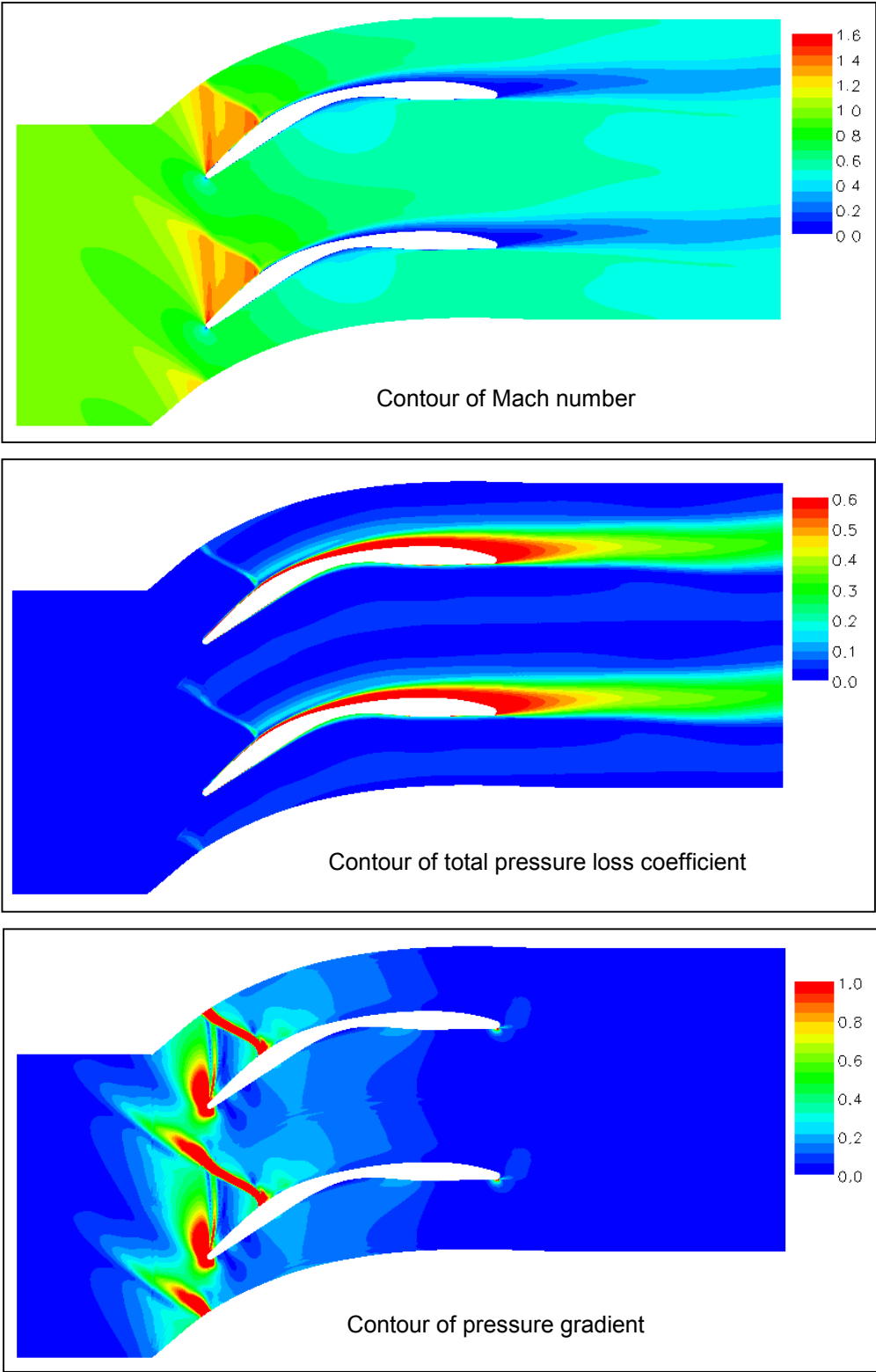


Figure 49 CFD flowfield characterization at design inlet flow angle (ES $M_1=0.94$)

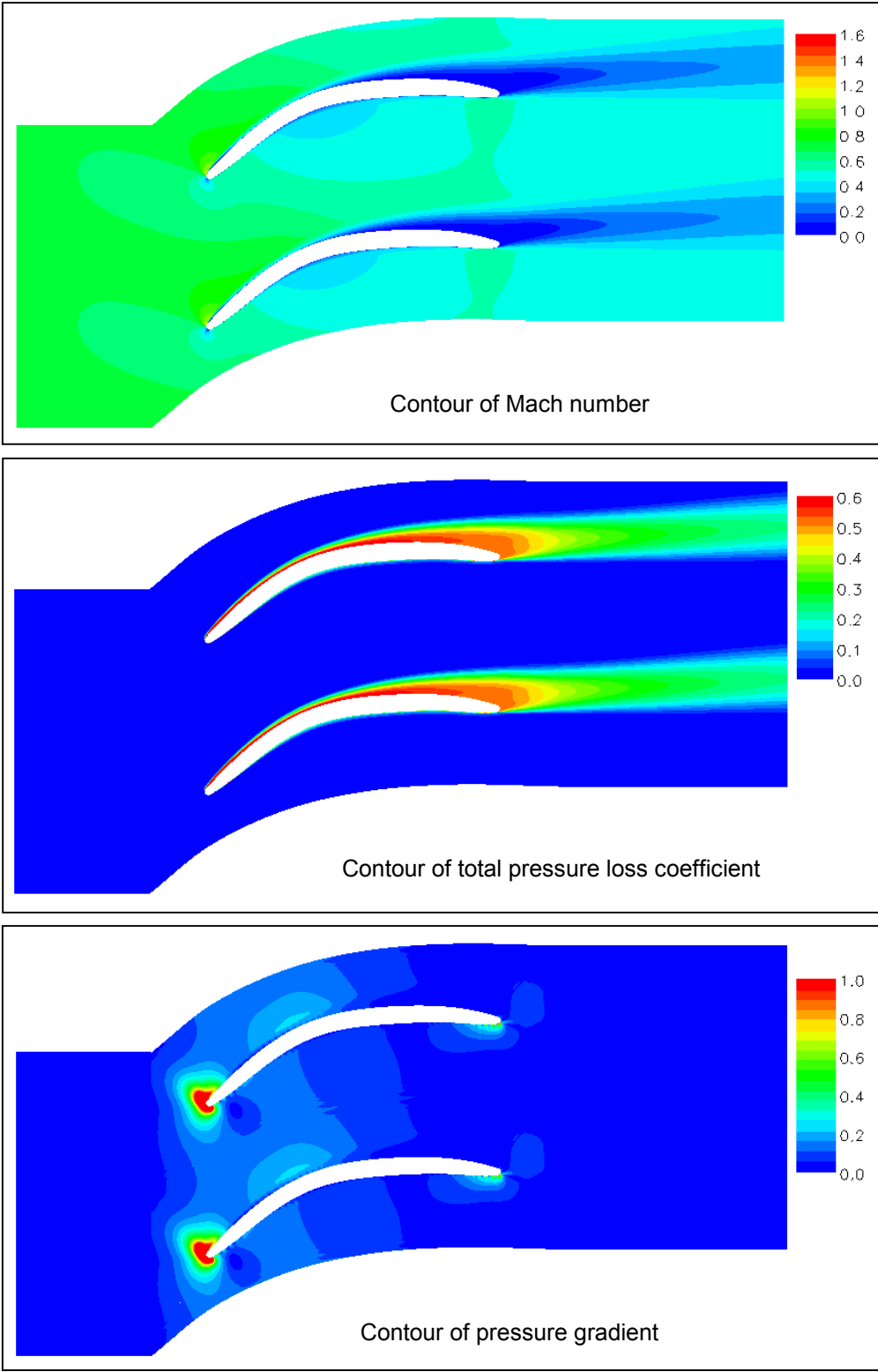


Figure 50 CFD flowfield characterization at design inlet flow angle (MOGA $M_1=0.68$)

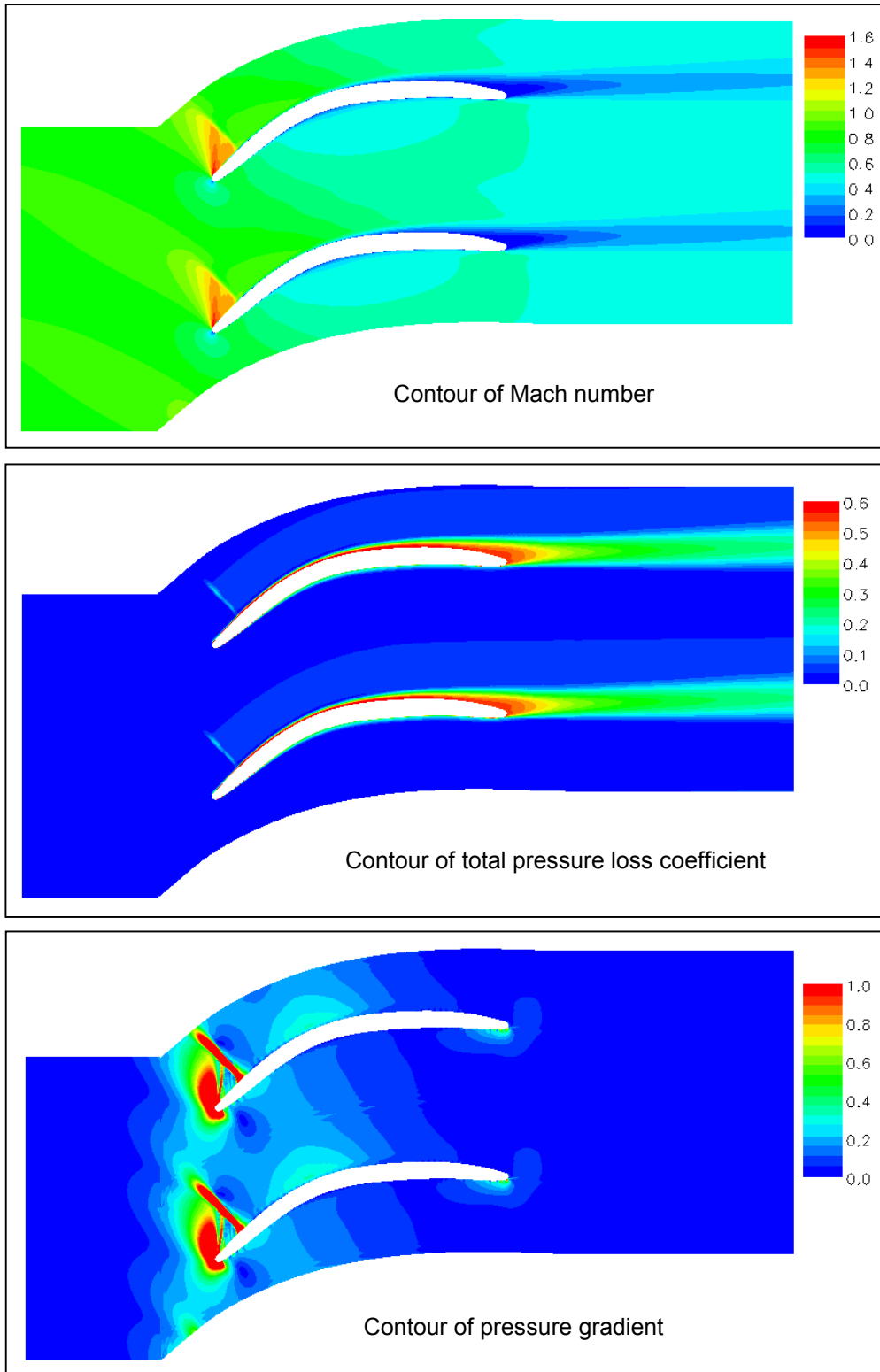


Figure 51 CFD flowfield characterization at design inlet flow angle (MOGA $M_1=0.84$)

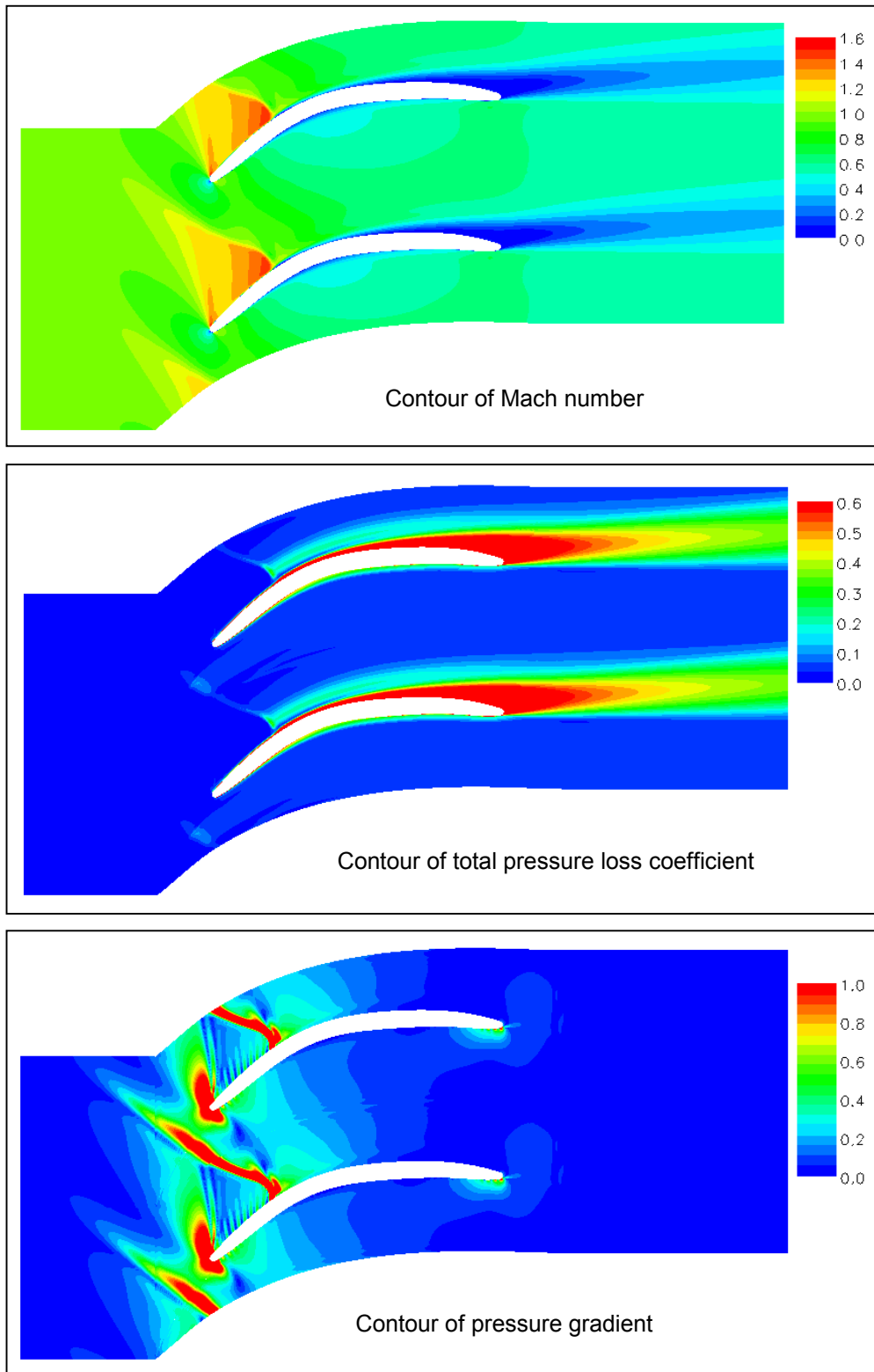


Figure 52 CFD flowfield characterization at design inlet flow angle (MOGA $M_1=0.95$)

3.2.5 Double Shock Flow Phenomenon

In the experiments, unlike the normal “single peak” wake profile, the wake profiles of ES were noticed having a small hump in the mainstream (out of wake) near the design condition. Special attention was paid to this flow phenomenon for academic interest. It was found that this unusual wake profile is due to the double shock interaction, as discussed below.

Figure 53 shows the wake profiles of ES at the design inlet flow angle at two inlet Mach numbers of 0.75 and 0.87. Losses decrease when inlet Mach number is increased from 0.75 to 0.87, due to a smaller wake (viscous losses), despite the shock loss hump in the mainstream (shock loss). CFD predicted deeper wakes and less mix-out of the exit flow. Accordingly, the shock loss hump from CFD is more distinct. Although the hump size is quite different between experiment and CFD, they both reveal the same flow structure in the blade passage: the leading edge shock hits the passage shock, where a local high loss region is generated. The loss-affected fluid is then transported with the passage flow, appearing as the hump in the wake profile. Figure 54 clearly shows this high loss band in the passage. This kind of wake shape (double peak) was also predicted by Kunz and Lakshminarayana [78] for a supersonic compressor cascade.

As shown in Figure 54, the boundary layer thickens faster and finally separates near the trailing edge at $M_1 = 0.75$. However, the flow remains attached at $M_1 = 0.87$ although strong shocks exist and the shock interaction causes local loss (the hump in the mainstream). The reason might be due to an advantageous pressure gradient distribution (acceleration after the shock) for $M_1 = 0.87$, as shown in Figure 55. Although there might be better explanation which replies on future work, it is clear so far that even with the strong double shock interaction (thus generating local shock loss), the boundary layer is well controlled for $M_1 = 0.87$, thinner and no separation, leading to the advantage of low overall losses at higher supercritical flow conditions.

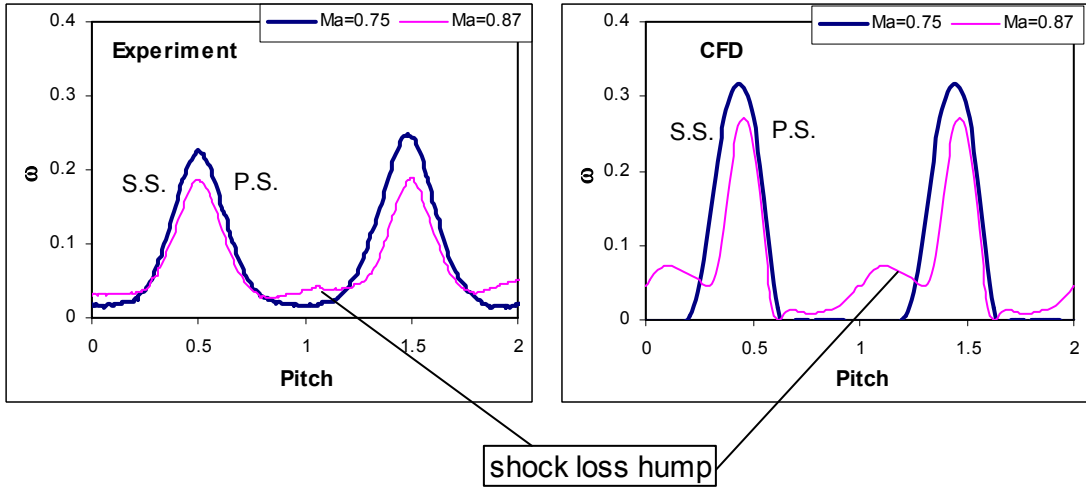


Figure 53 Double shock phenomenon of ES – wake profile

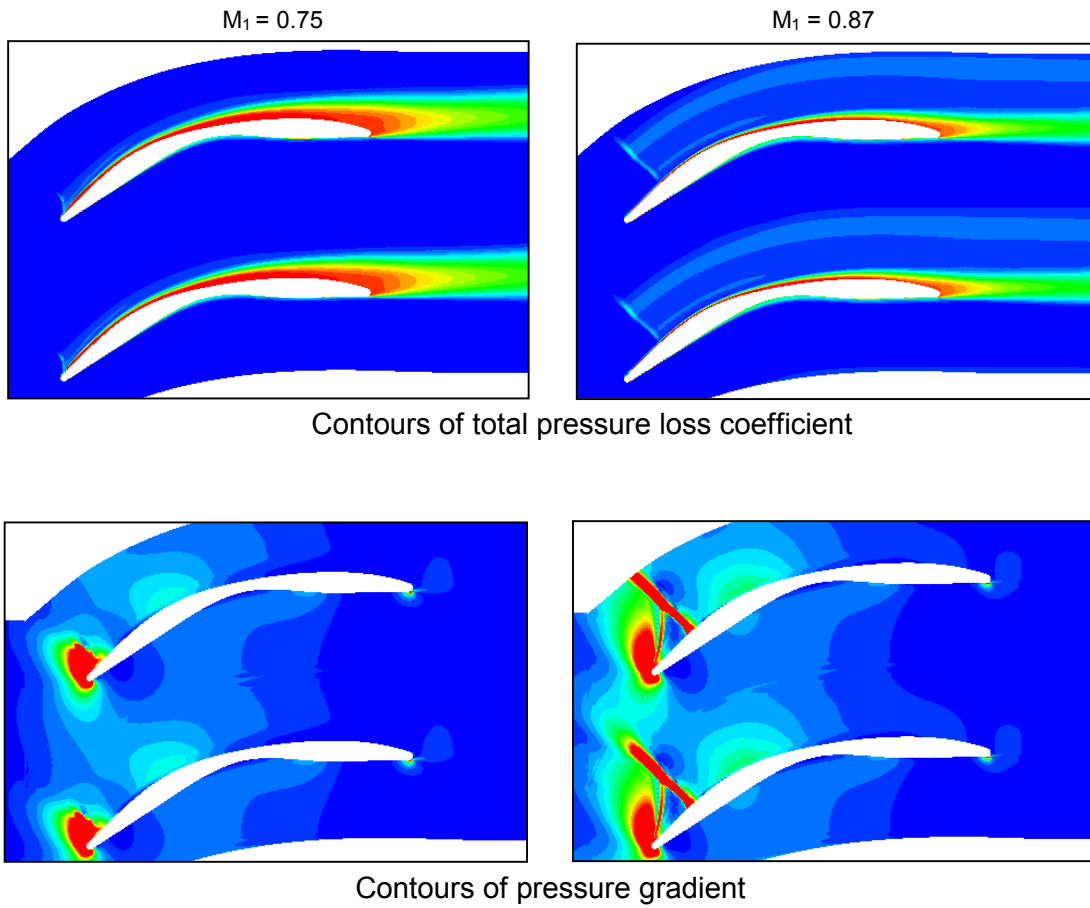


Figure 54 Double shock phenomenon of ES – loss mechanism

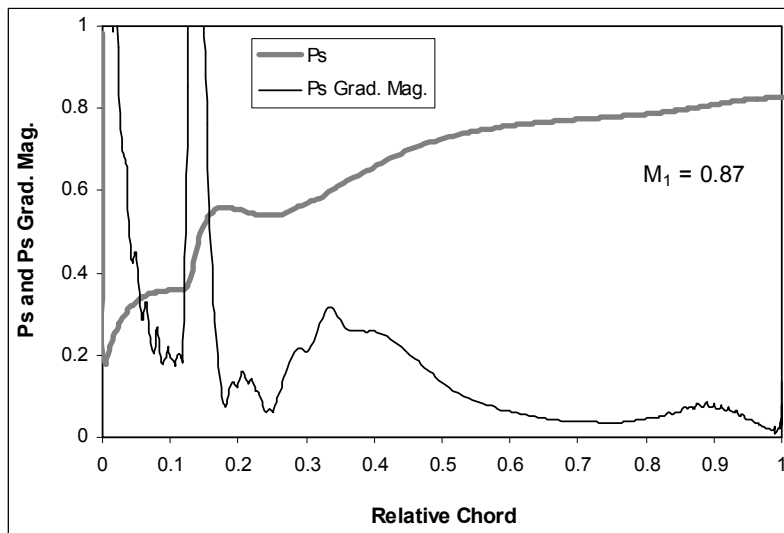
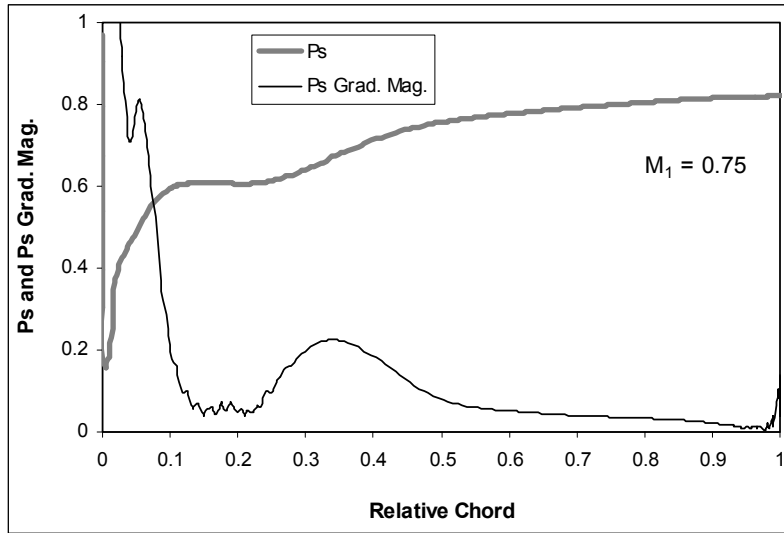


Figure 55 Double shock phenomenon of ES – pressure gradient

3.3 Loss Robustness and Flow Structures at Off-Design Inlet Flow Angles

To complete the characterization of the blade performance, CFD analysis was further conducted for a wide range of inlet flow angles to determine the “loss bucket” for each blade. At each inlet flow angle, the computation was conducted at three representative inlet Mach numbers (low, intermediate, high). The available experimental data at some of the flow conditions are also presented to support the CFD results. In addition to the important “loss vs. inlet flow angle” results, flowfield characterizations are also presented for selected flow conditions to show the associated flow physics.

3.3.1 Loss Robustness

CFD results of loss variation with inlet flow angle* for the three blades are presented in Figure 56. The inlet flow angle ranges were chosen wide enough to cover the choke and stall conditions, thus the “loss bucket” (blade effective operating incidence range) has been determined. The results are presented at three different inlet Mach numbers ($M_1 = 0.61, 0.78, \text{ and } 0.87$) and each Mach number corresponds to a curve in the plots. Choosing loss coefficient $\omega=0.1$ as the criterion to define blade effective operating incidence range, the incidence robustness can be evaluated for the three blades at different inlet Mach numbers, as summarized in Table 7.

For the three blades, the effective incidence ranges decrease with increasing inlet Mach number, indicating the increasing design challenge of maintaining low losses for high turning compressor blades at higher supercritical flow conditions (like $M_1 = 0.87$). At the design inlet Mach number ($M_1 = 0.87$), the optimized blades have achieved some effective incidence ranges (incidence robustness of 5°) while the baseline blade failed completely. Therefore, in addition to the significant loss reduction obtained for the design condition, the optimized blades also excel in incidence robustness at higher supercritical flow conditions. At off-design inlet Mach numbers ($M_1 = 0.61 \text{ and } 0.78$), the incidence robustness of the optimized blades only degrades slightly. In general, the optimized blades are superior to the baseline blade.

* Corresponding to incidence angle by a relation: $\beta_1=I+48.4^\circ$

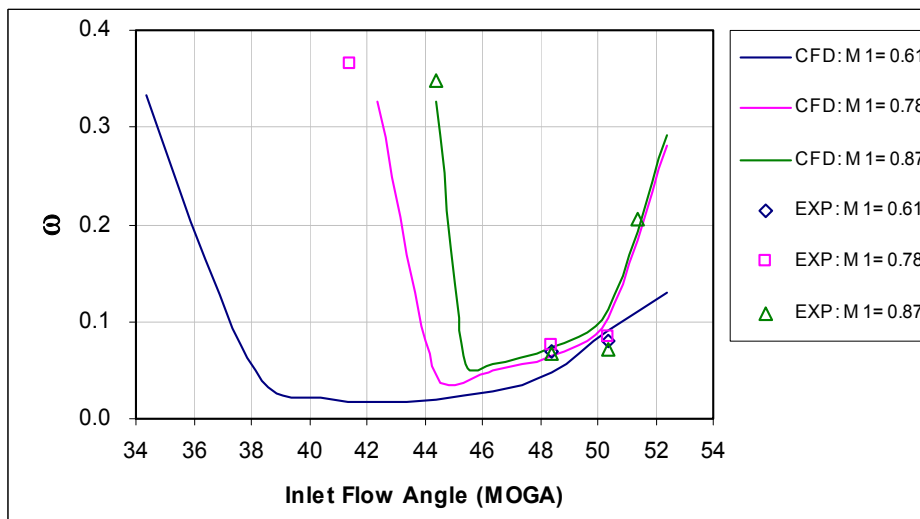
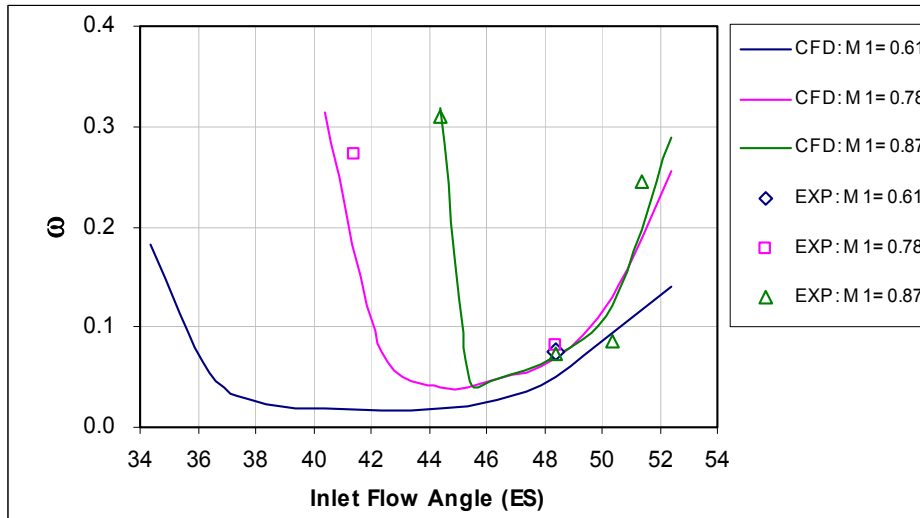
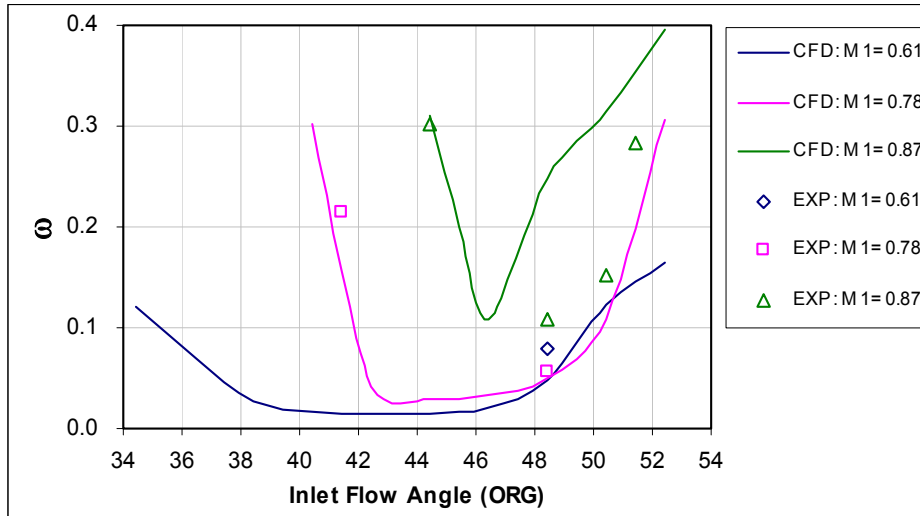


Figure 56 Loss variation with inlet Flow Angle

Table 7 Summary of incidence robustness

Blade	M₁	Effective Incidence Range	Incidence Robustness
ORG	0.61	35.2° – 49.8°	14.6°
	0.78	41.8° – 50.2°	8.4°
	0.87	None	0°
ES	0.61	35.6° – 50.4°	14.8°
	0.78	42.2° – 49.6°	7.4°
	0.87	45.0° – 50.0°	5.0°
MOGA	0.61	37.2° – 51.0°	13.8°
	0.78	43.8° – 50.4°	6.6°
	0.87	45.2° – 50.2°	5.0°

Although the cascade testing was originally intended to confirm the blade performances at the design incidence, it was extended to some selected off-design incidences in order to provide more experimental data for validating the CFD results. In addition to the design incidence, some experimental data for the choke and stall conditions of each blade are also included in Figure 56. It is seen that the agreement between CFD and experiment is generally good except for the ORG at the design and positive incidences at $M_1=0.87$, where the flow severely separated. CFD has qualitatively differentiated the loss levels and the associated flow behaviors between the baseline (separated flow) and optimized blades (no separation). Thus, the comparison of the loss robustness (loss vs. incidence) using CFD results should be acceptable in terms of relative evaluation of the three blades.

It should be pointed out that for the three M_1 curves in Figure 56, M_1 could not be achieved in some cases in the CFD computations and experiments at the choke flow conditions. To make the loss bucket curves look completed, the highest possible M_1 has been used. Those cases are listed in Table 8. Although there is some quantitative discrepancy between CFD and experiment for the achievable choke flow conditions, both

CFD and experiment found the same trend of the increasing difficulty from ORG, ES to MOGA in reaching the highest flow speeds at the choke conditions.

Table 8 Achieved inlet Mach numbers at the choke flow conditions

Blade	$\beta_1(^{\circ})$	Achieved M_1 / Supposed M_1	
		CFD	EXP
ORG	40.4	0.76 / 0.78	
	44.4	0.86 / 0.87	0.86 / 0.87
ES	40.4	0.72 / 0.78	
	41.4		0.75 / 0.78
	44.4	0.86 / 0.87	0.84 / 0.87
MOGA	41.4		0.74 / 0.78
	42.4	0.75 / 0.78	
	44.4	0.83 / 0.87	0.80 / 0.87

3.3.2 Blade Surface Mach Number at $\beta_1=45.4^{\circ}$

As above discussed, the flow is choked at $\beta_1=44.4^{\circ}$. The inlet flow angle of 45.4° represents near the most negative incidence condition where the flow is not choked yet. Thus, blade surface Mach number was measured at this flow angle to provide another set of experimental data to compare with CFD.

Figure 57 shows the experimental and CFD results for ORG at four inlet Mach numbers at the inlet flow angle of 45.4° . Comparing these results with those in Figure 41, it is seen that better agreement between experiment and CFD was obtained at $\beta_1=45.4^{\circ}$. Two reasons would account for this improvement in agreement. One is the well-known trend of AVDR decrease with decreasing inlet flow angle. Thus at this negative incidence angle, experimental AVDR is closer to unity than at the design incidence angle, leading to less AVDR effect. The other is the losses at this angle are lower than at the design angle, meaning thinner boundary layer or lessened boundary layer separation, making an easier case for the CFD prediction.

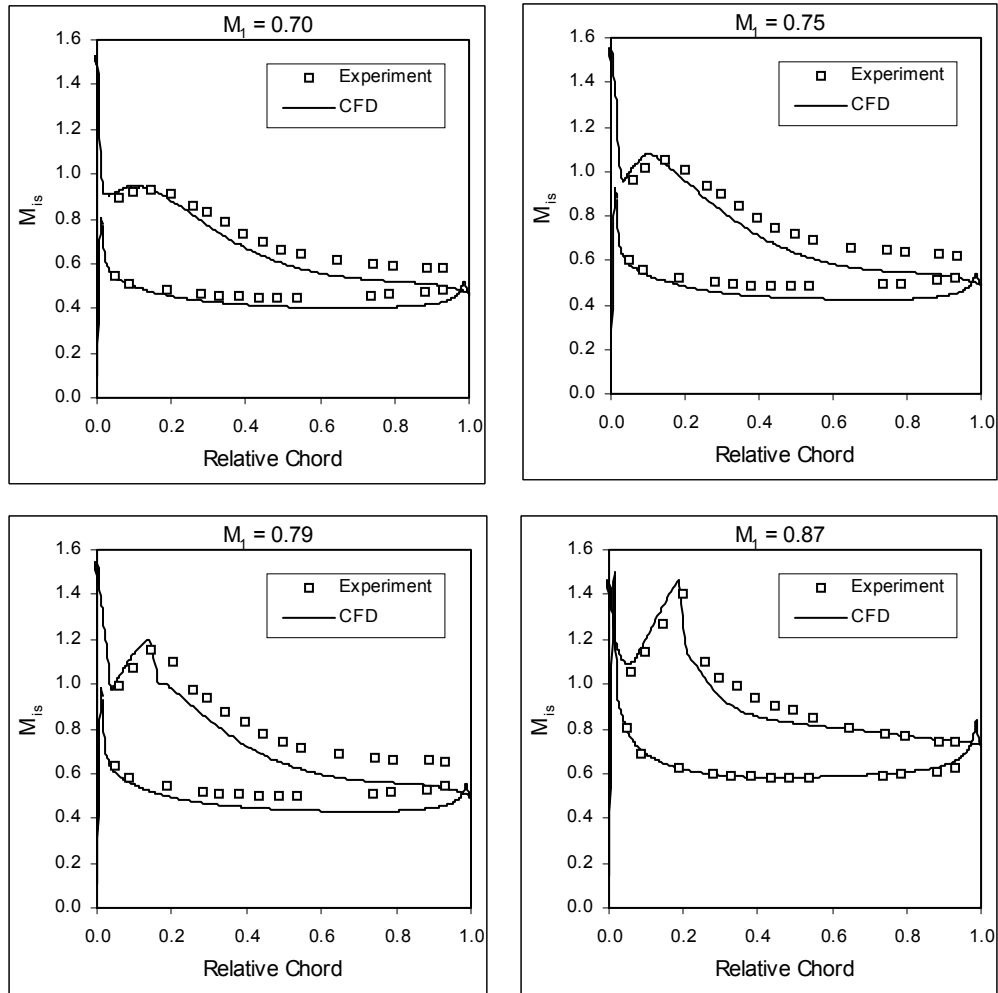


Figure 57 Blade surface Mach number at $\beta_1=45.4^\circ$ - ORG

Figure 58 shows the experimental and CFD results for ES at four inlet Mach numbers. Very good agreement was obtained at $M_1=0.75$ and 0.81 except for a little up-shifting of experimental results due to the slight effect of AVDR at rear part of the blade. Increasing M_1 to 0.87 and 0.93 , some discrepancy appeared within the supercritical patch at the blade front part, and the rear part up-shifting of experimental results is more distinct due to the increased AVDR effect. In general, CFD results represent the essential flow characteristics as revealed by experimental results, and can be used to characterize the flow within some quantitative uncertainty.

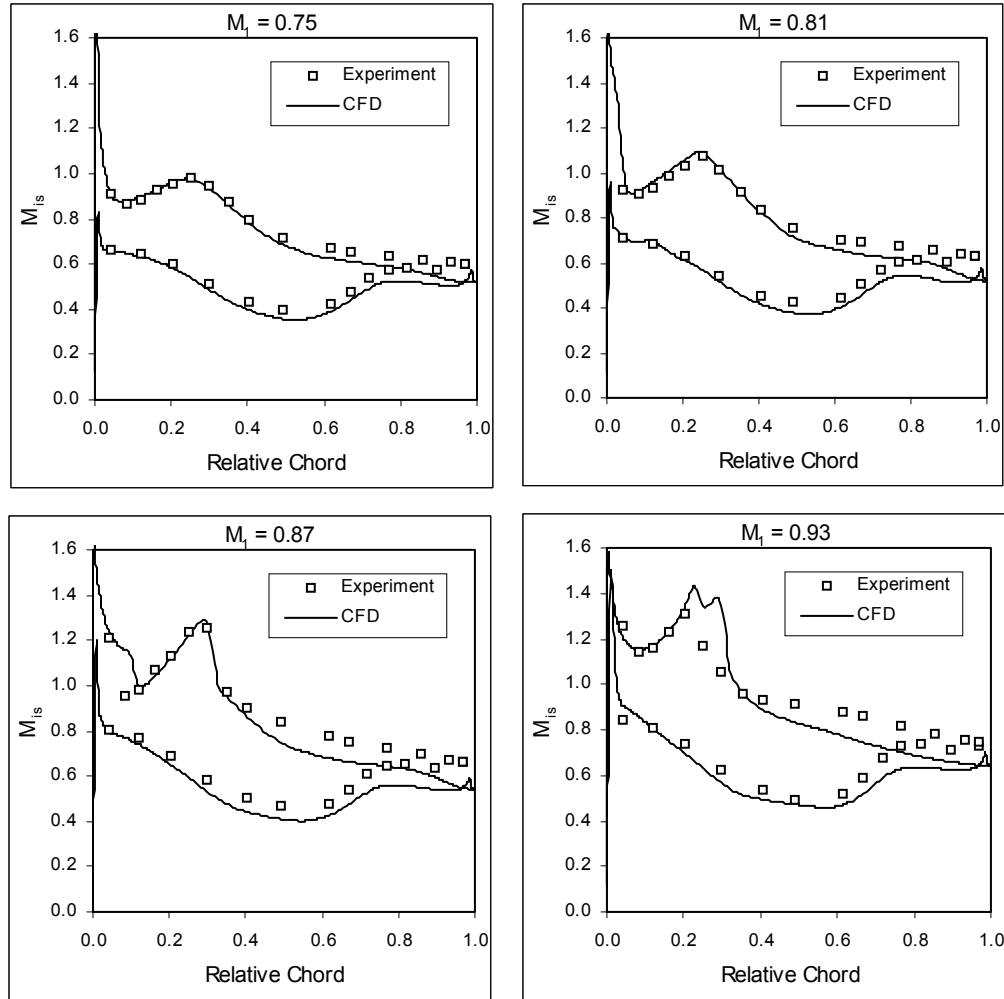


Figure 58 Blade surface Mach number at $\beta_1=45.4^\circ$ - ES

Figure 59 shows the experimental and CFD results for MOGA at four inlet Mach numbers. Similar to ES, very good agreement was obtained for low and intermediate inlet Mach numbers ($M_1=0.70, 76$ and 0.82) except for an up-shifting of experimental results due to the slight effect of AVDR at rear part of the blade. At higher $M_1=0.87$, the discrepancy is larger due to the strengthened shock at the blade front part and increased AVDR effect at the rear part. Nevertheless, CFD results did calculate the flow qualitatively well, such as the velocity pattern and blade loading distribution.

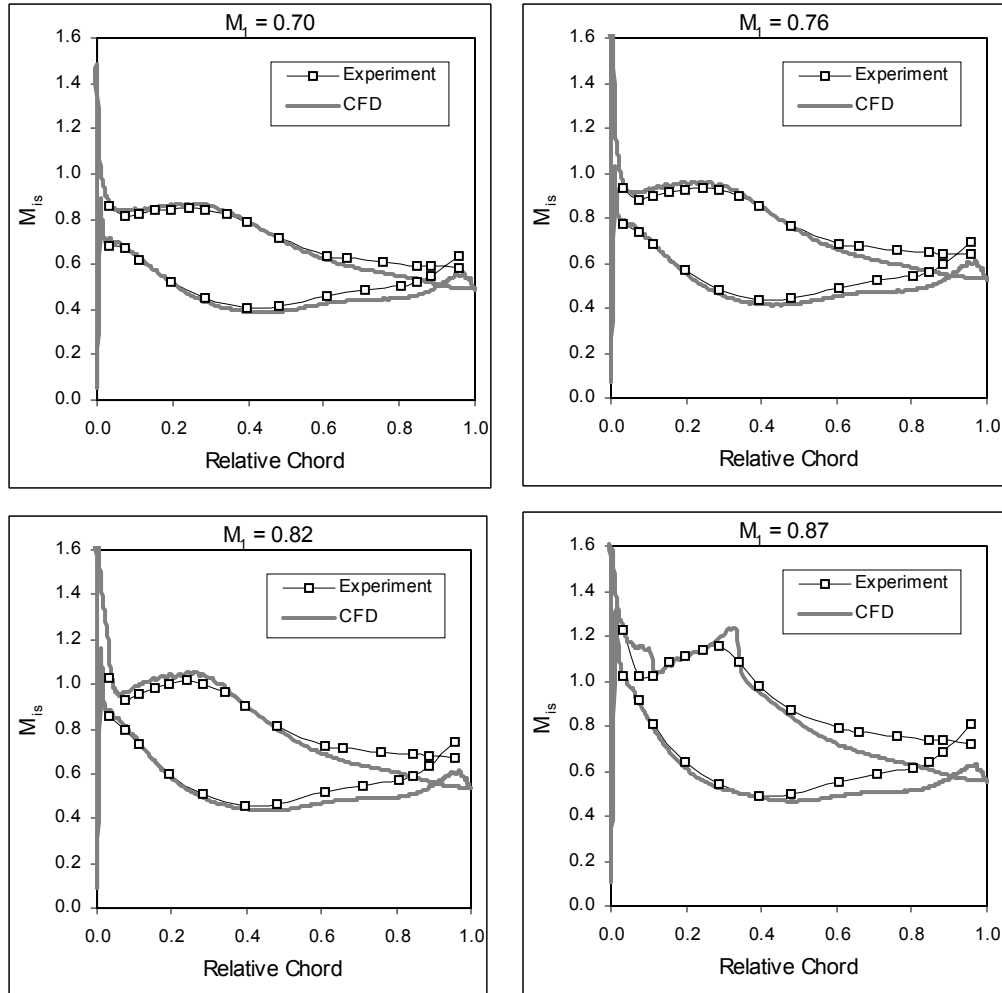


Figure 59 Blade surface Mach number at $\beta_1=45.4^\circ$ - MOGA

3.3.3 Flow Structures at Selected Off-Design Conditions

To better understand the loss variation with inlet flow angle shown in Figure 56 and the related flow physics, CFD flowfield characterizations for the choke and stall conditions of each blade are presented in Figure 60-65. The choke conditions are shown at the incidence of -4° for the highest inlet Mach number that can be reached, where ORG and ES reached $M_1=0.86$ while MOGA reached $M_1=0.83$. The stall conditions are shown at the incidence of 4° at the design inlet Mach number for the three blades.

The three blades share similar flow structure at the choke condition: a strong passage shock crossed the entire passage and the flow was choked. After the shock, severe boundary layer separation occurred on the suction surface, resulting in the loss cliff as seen in Figure 56. The difference between the three blades is the passage shock location. ES and MOGA have the shock generated more downstream than ORG. At lower Mach numbers ($M_1=0.61$ and 78), CFD flowfield characterizations revealed the choked flow and boundary layer separation at lower incidence angles for the three blades. Accordingly, the loss cliffs at these two Mach numbers shifted left, leading to a wider effective incidence range (see Figure 56).

The flow structures of the three blades at the stall condition are similar as well. At this positive incidence, the supersonic patch at the front blade part moved upstream close to the leading edge, ended with a strong passage shock. Unlike the case of the choke condition, the passage shock did not cross the entire passage, thus the flow could still be accelerated to the desire Mach number. Right after the passage shock, significant boundary layer separation was initiated, leading to the loss cliff at this positive incidence, as seen in Figure 56. At this incidence, the boundary layer separation is not only driven by the shock, but also resulted from the larger incidence. Particularly for lower Mach number case such as $M_1=0.61$, there is no shock generated, but losses climbed up as well (see Figure 56). This is due to the suction surface boundary layer separation, which is solely due to the increased incidence.

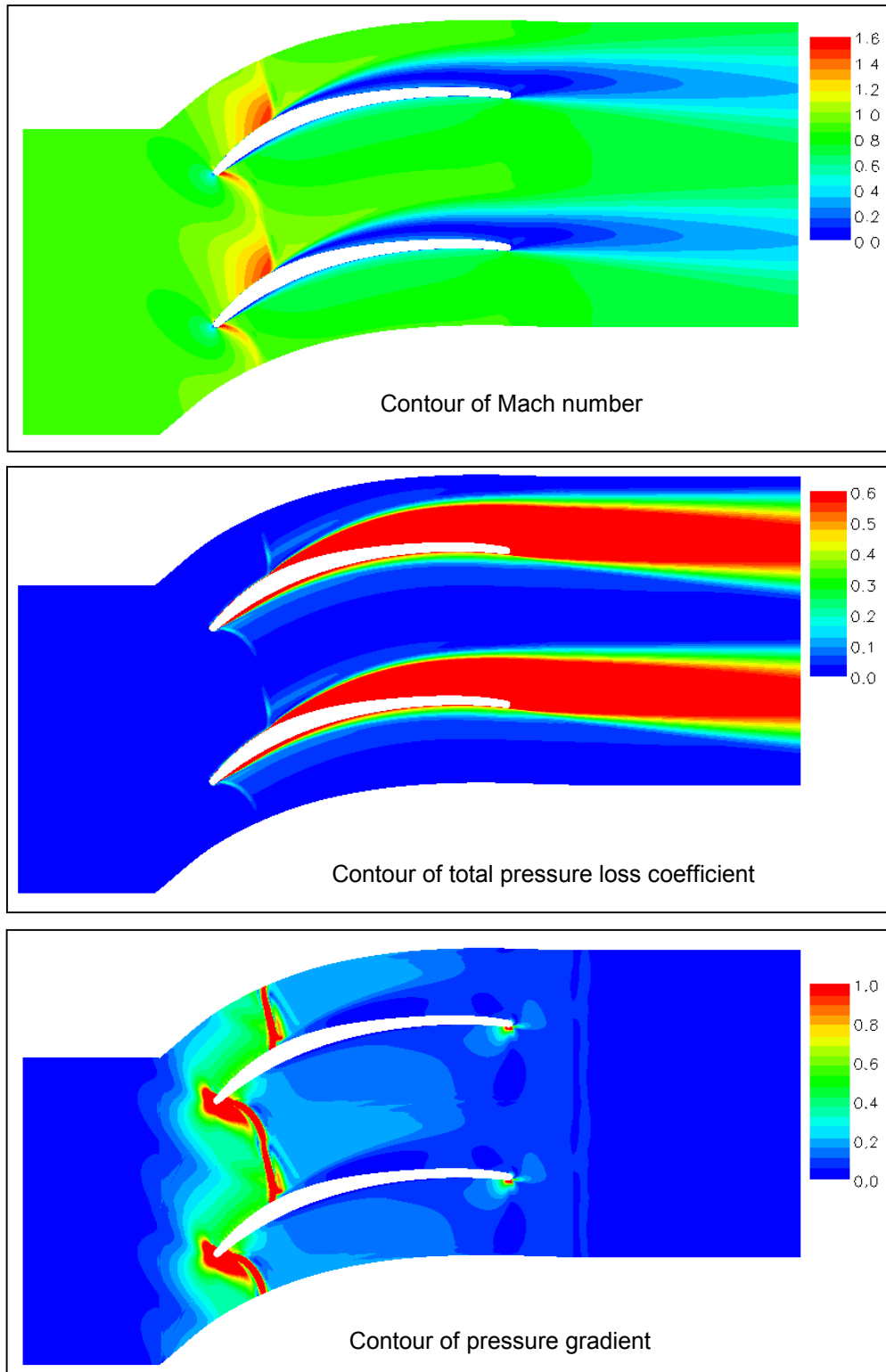


Figure 60 CFD flow structure at choke condition (ORG: $M_1=0.86$, $\beta_1=44.4^\circ$)

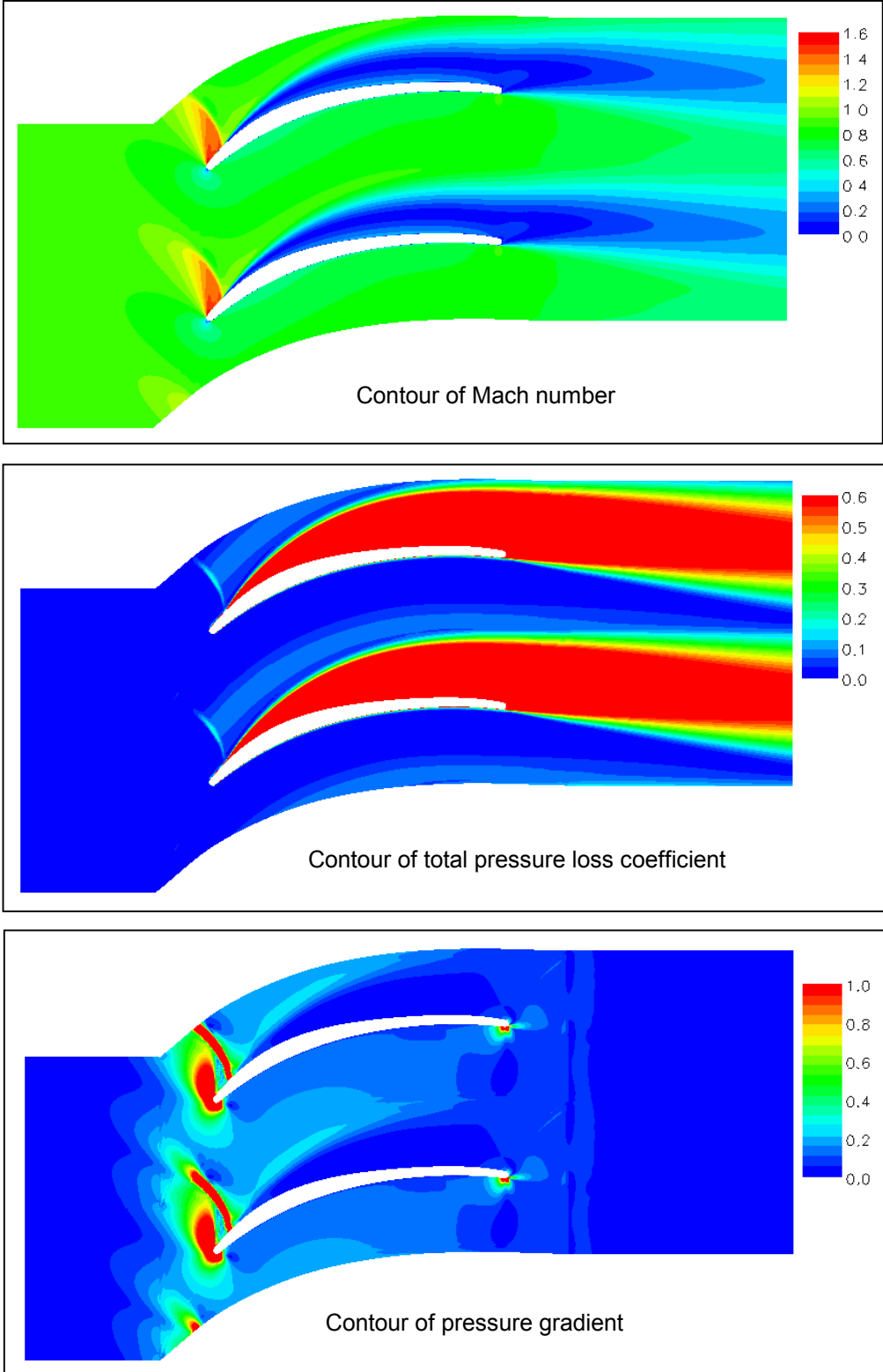


Figure 61 CFD flow structure at stall condition (ORG: $M_1=0.87$, $\beta_1=52.4^\circ$)

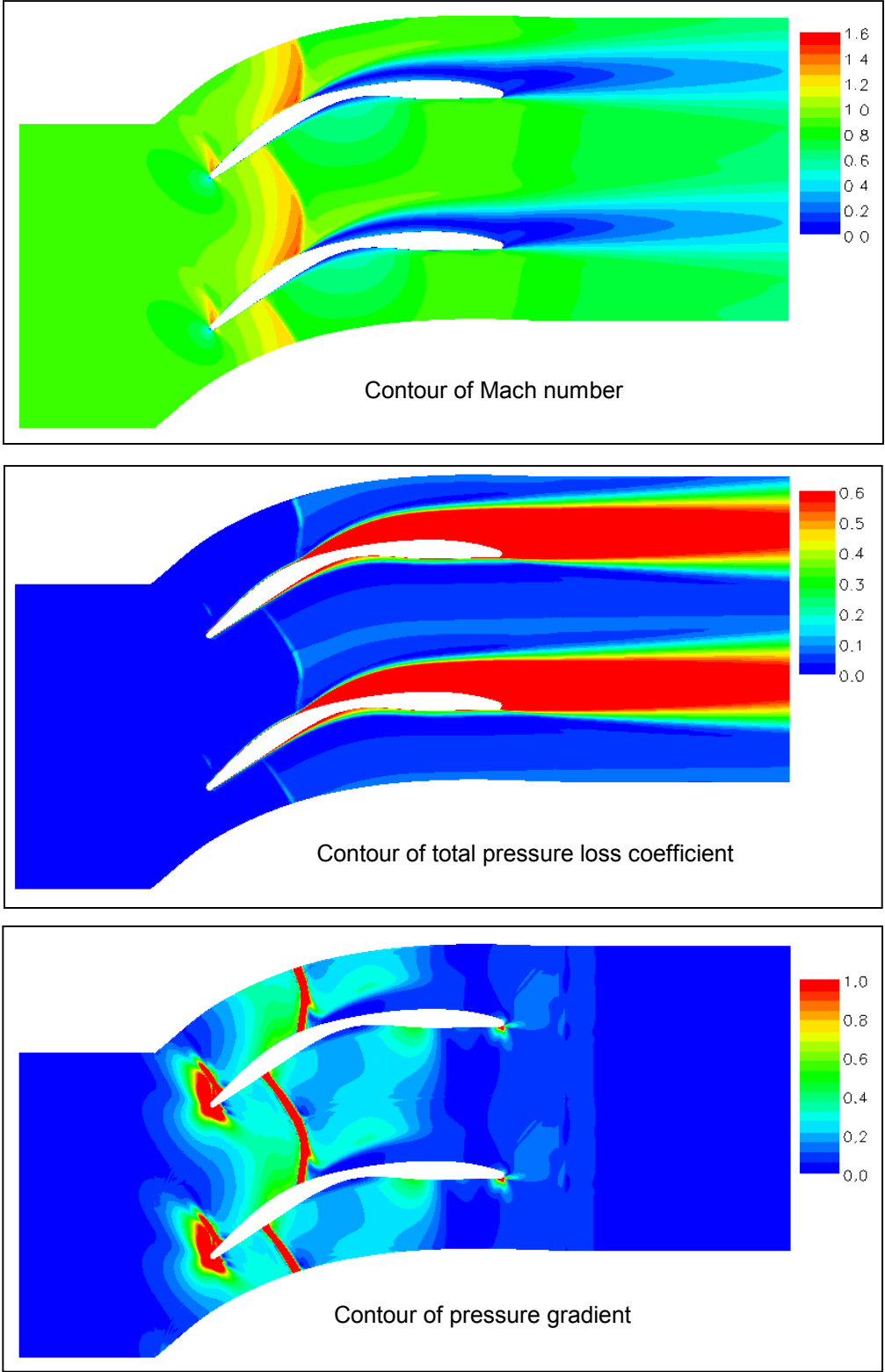


Figure 62 CFD flow structure at choke condition (ES: $M_1=0.86$, $\beta_1=44.4^\circ$)

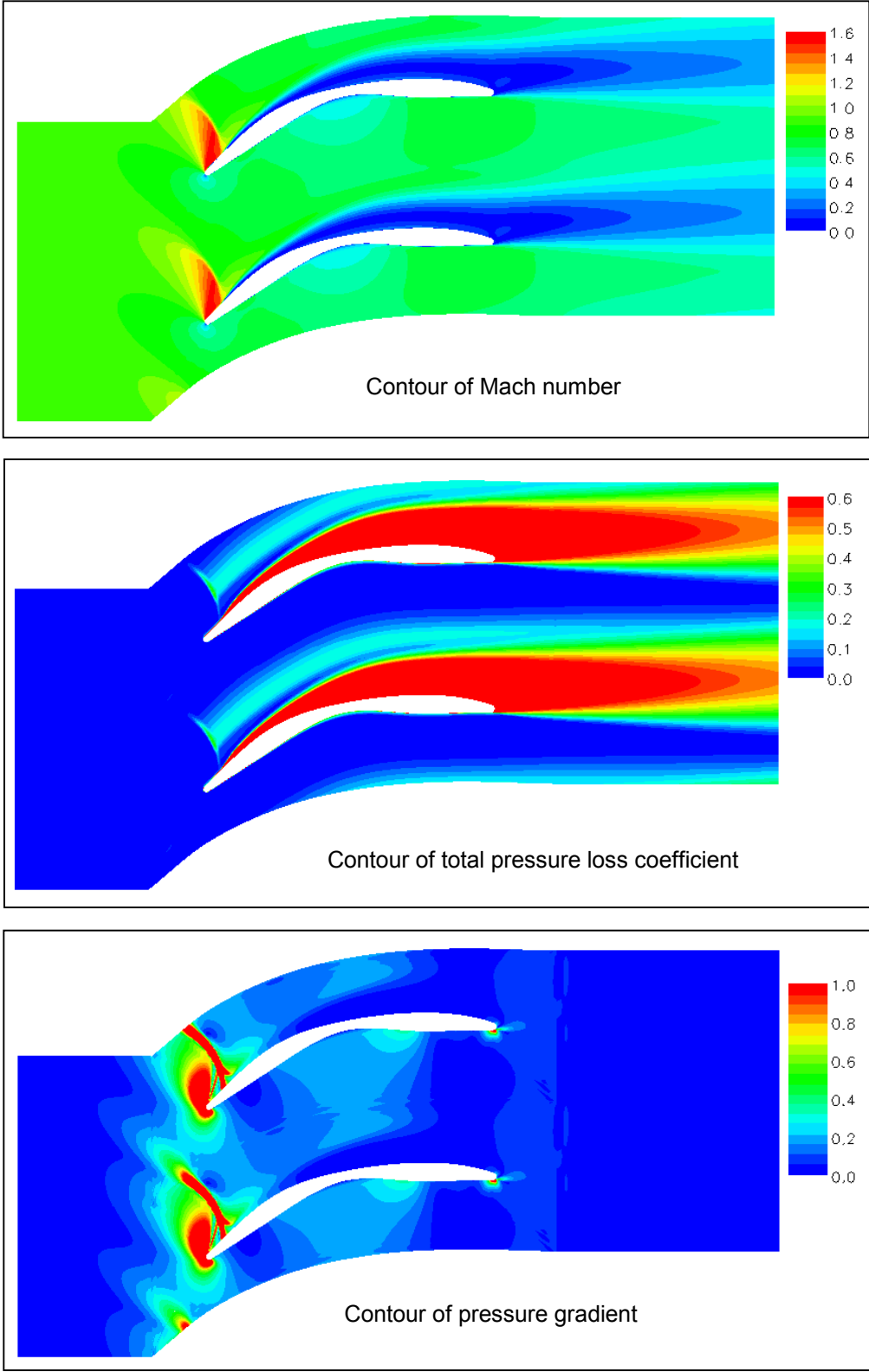


Figure 63 CFD flow structure at stall condition (ES: $M_1=0.87$, $\beta_1=52.4^\circ$)

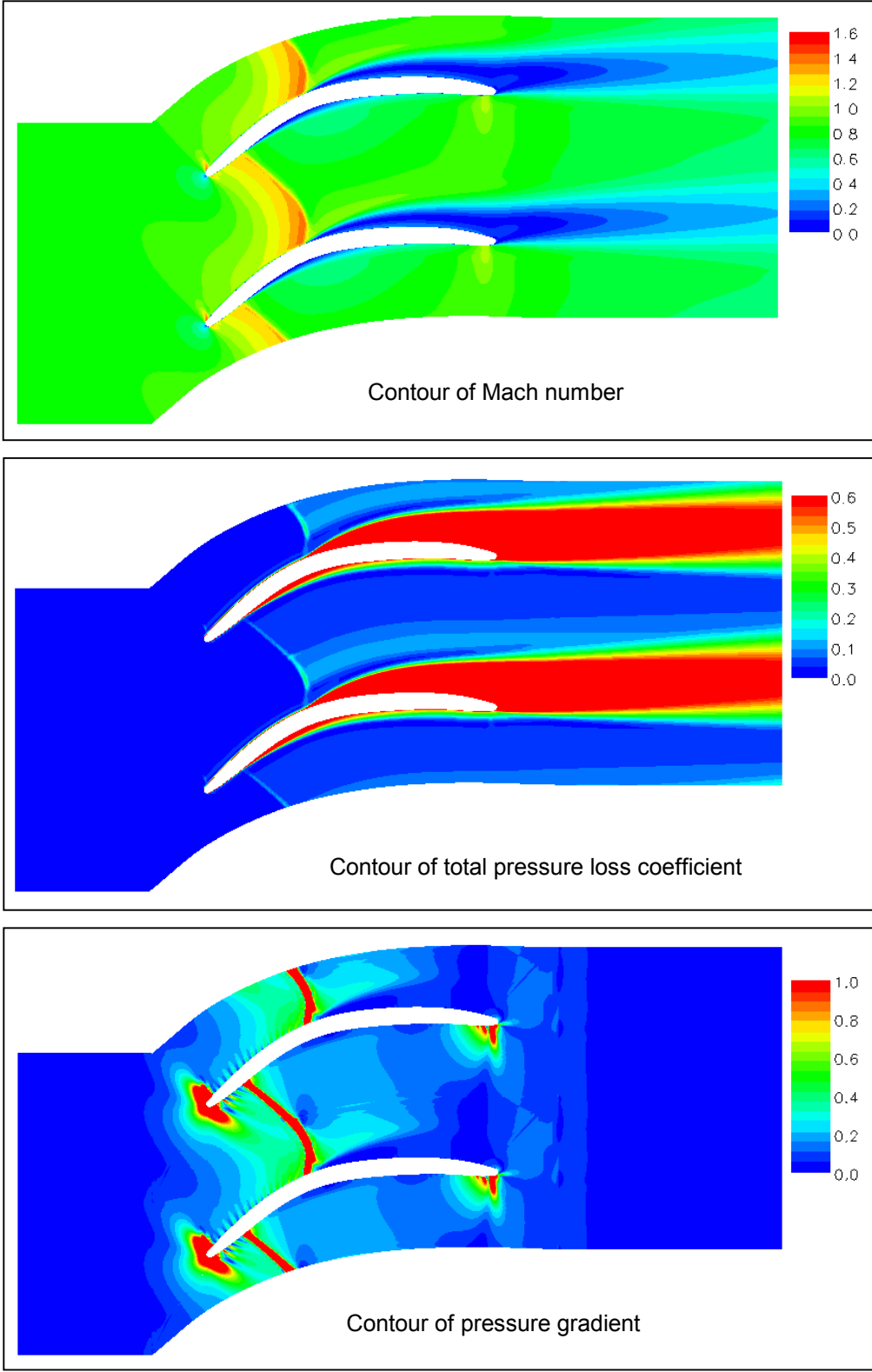


Figure 64 CFD flow structure at choke condition (MOGA: $M_1=0.83$, $\beta_1=44.4^\circ$)

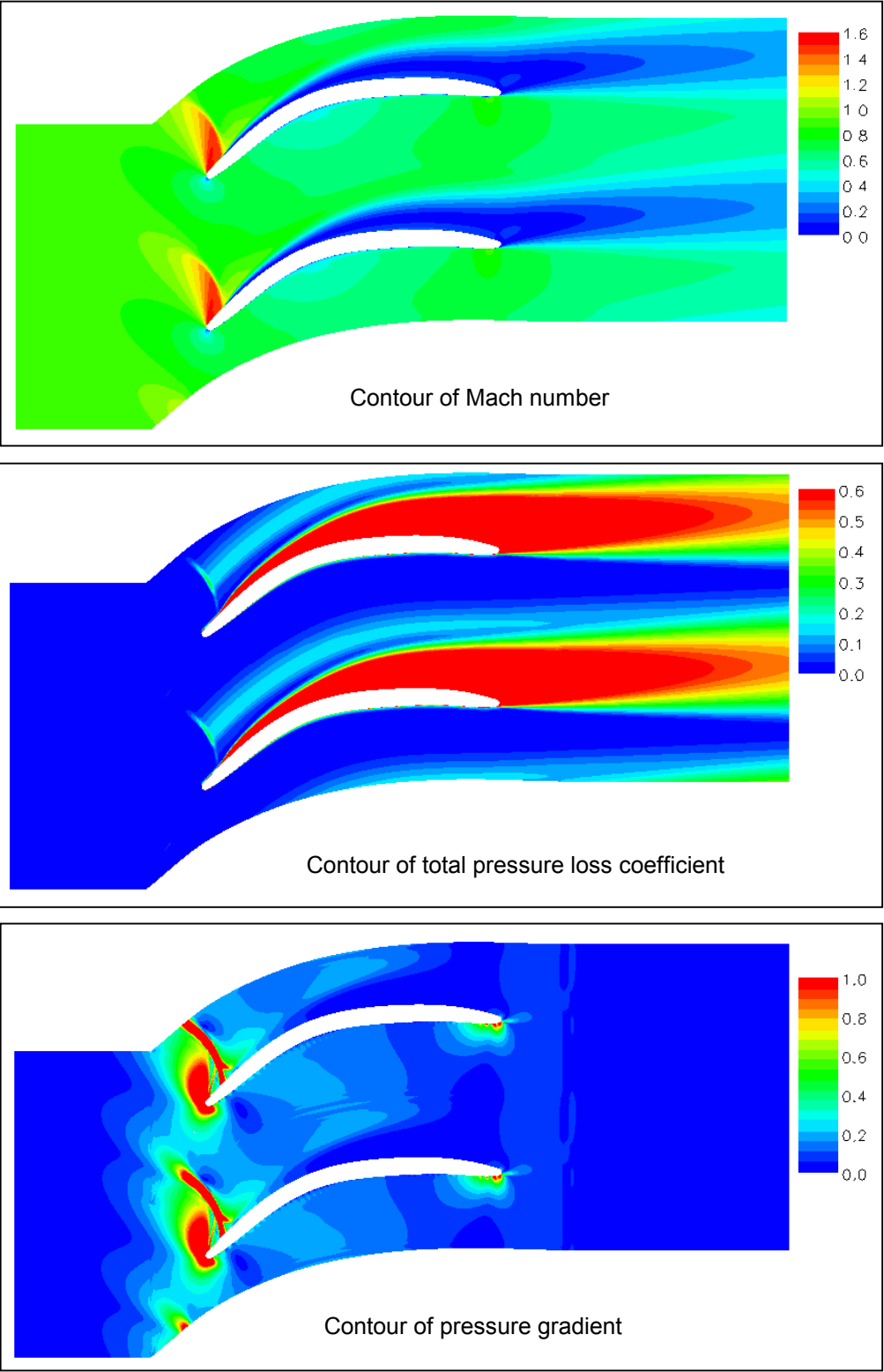


Figure 65 CFD flow structure at stall condition (MOGA: $M_1=0.87$, $\beta_1=52.4^\circ$)

4. Conclusions

Extensive experimental and numerical investigations were conducted for three compressor blades: ORG, ES and MOGA. The baseline ORG is a controlled diffusion airfoil (CDA). ES and MOGA are optimized blades. The following conclusions are drawn from the current work.

4.1 Cascade Performance Confirmation and Design Tool Validation

At the design condition ($M_1=0.87$, $\alpha_1=48.4^\circ$), cascade testing confirmed significant loss reduction (30%) from the baseline to the optimized blades. MOGA has slightly lower losses than ES. Corresponding to the lower losses, the optimized blades achieved higher static pressure ratio (more effective compression) than the baseline. As the primary objective of the blade optimization was to achieve lower losses, the blade design has been proven to be a success and the blade optimization tools have been validated. Meanwhile, experimental results showed under-turning of the flow for the optimized blades (ES under-turning of 2° and MOGA under-turning of 3° than the baseline). The flow turning experimental result is another important feedback to the blade design, suggesting either adjusting the velocity triangle for the compressor stage matching, or improving the design for higher flow turning.

Besides the design condition, the optimized blades have lower losses at higher supersonic flow conditions ($M_1>0.83$) at the design incidence angle. The optimized blades have also achieved a low-loss incidence range 5° compared to 0° of the baseline at $M_1=0.87$, indicating the superior incidence robustness of the optimized blades at higher supersonic flow conditions. Moreover, the optimized blades maintain the same excellent performance at normal supersonic flow conditions ($M_1=0.6-0.8$) as the baseline blade. As the baseline was a significant compressor blade design achievement using the Controlled Diffusion Airfoil concept, the low losses achieved by the optimized blades for a wider speed range marked the advancement of the blade design to a new generation, using the state-of-the-art blade shape optimization methods.

4.2 Flow Physics for High-Turning Supercritical Compressor Cascades

The current study has raised the level of understanding of compressor aerodynamics in high-turning cascade flow at higher supercritical flow conditions.

- The drastic performance degradation of a CDA blade at $M_1 > 0.83$ is due to severe boundary layer separation on the blade suction surface, which is in turn, resulted from the coincidence of the strong passage shock and adverse pressure gradient at the blade front part.
- For a CDA blade, $M_1 = 0.8$ probably corresponds to the blade suction surface Mach number peak of 1.3, as indicated by the conventional CDA design criteria as the upper velocity limit. Over this speed, the passage shock seems inevitable. Further increasing M_1 will strengthen the passage shock and nullify the conventional CDA design concept.
- At a higher supercritical flow condition range ($M_1 = 0.83-0.91$), the optimized blades showcased a superior flow pattern to achieve a no-separation and low-loss compression process: stronger leading edge acceleration, less passage shock strength near the blade surface, re-acceleration (favorable pressure gradient) right after the shock, then deceleration at more downstream. This flow process leads to a more even blade loading than the primarily front-loaded CDA. As such, the flow can overcome the adverse pressure gradient step by step and avoid separation.

4.3 Design Philosophy for High-Turning Supercritical Compressor Cascades

The current study has shed light on the design philosophy for high-turning compressor cascades at higher supercritical flow conditions.

- The key is to control boundary layer from separation. To achieve this goal, efforts should be directed to locate an advantageous acceleration-deceleration pattern to avoid the concentration of the adverse pressure gradients due to blade shape, blade curvature, and shocks.
- Although the optimized blade shape itself plays an important part in a successful design, and it may differ from design to design, setting the high blade camber more downstream than a conventional CDA, such as 30-50% chord, seems a common

criterion to follow in order to separate the adverse pressure gradients from the passage shock (around 20% chord) and the blade camber.

- With the same cascade geometry, the front highly cambered CDA seems to have higher flow turning capability than the mid-chord high camber design. In other words, it is more difficult for a mid-chord high camber design to achieve high flow tuning. To overcome this disadvantage, adjustment of the blade stagger angle and camber angle may be of help.

4.4 Recommendations for Future Work

Following the current work, future work can be directed for further understanding of the flow and better design.

- Experimental and/or numerical investigations of the boundary layer characteristics of the high turning compressor cascades at higher supercritical flow conditions, to clarify the transition behavior. The study for lower Reynolds number conditions (in the critical Reynolds number range of $1-3 \times 10^5$) will be of academic interest.
- Redesign the blade with the mid-chord high camber, but adjust the stagger angle and camber angle to seek for higher flow turning.
- At higher supercritical flow conditions, the compressor cascade has a supersonic patch at the blade front part. It is well known this supersonic flow is terminated by a passage shock, although the shock location and strength may vary with different blade designs. Therefore, the most interesting and most challenging future work will be to refine the blade shape, such that a family of compression waves is obtained to replace the passage shock. If this was achieved, it would eliminate the shock loss and avoid the likelihood of the shock-induced boundary layer separation. Consequently, the benefit is not only the reduction of the overall losses, but also leaving more freedom to the turning and loading arrangement.

Appendix A Effect of AVDR

A.1 Introduction

The important role of axial velocity density ratio (AVDR) in two-dimensional linear cascade testing was ascertained earlier in the 1960s [79] and has since then given sufficient attention. In cascade testing practice, endwall* air removal (suction or bleed) turns out to be a primary means to control AVDR and it has been widely adopted by researchers in the field. The idea is illustrated schematically in Figure A1. However, recent cascade testing of high-turning supercritical compressor blades by the current work suggested that the AVDR influence were more complicated than could be simply handled by the conventional method of endwall air removal. Therefore, this appendix presents an experimental and numerical study of the two high-turning supercritical compressor blades (ORG and ES) with the focus on this issue. In addition, with reference to previous related research, discussion is directed towards the strategy to deal with the AVDR influence in modern cascade wind tunnel testing.

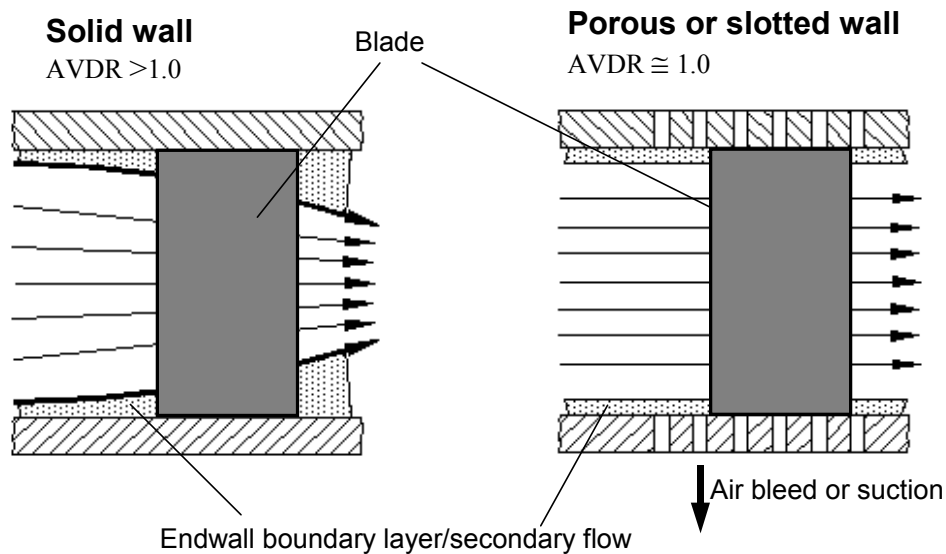


Figure A1 Flow contraction and AVDR control in cascade testing

* Also referred to as “sidewall” since the tested cascade is usually laid out in the vertical plane in most tunnel facilities.

A.1.1 Review of Previous Research

Earlier work had established a conventional viewpoint: AVDR had a large effect on the cascade flow and the cascade performance. In general, with increasing AVDR, the cascade will see an up-shifting of blade surface Mach number distribution and drop of losses. This AVDR effect is referred to as “the Normal AVDR Influence” in this appendix.

The experimental investigation conducted in a low speed cascade wind tunnel by Pollard and Gostelow [79] was one of the earliest efforts to ascertain the Normal AVDR Influence and reduce the influence by sidewall air removal. They found that the cascade flow with solid sidewalls was significantly twisted by the sidewall secondary flow for a low aspect ratio ($AR = 2$), but for high aspect ratios ($AR \geq 3.0$), a large part of the span was unaffected by the secondary flow although the blockage effect of the near-wall region was still appreciable ($AVDR > 1.1$). A low aspect ratio would give good two-dimensional results if porous sidewalls were used to remove the sidewall boundary layer. Nevertheless, even with sidewall suction in use, an area of low energy air was present near junction of the wall and the blade suction surface. Their attempts to remove it had failed. The complexity of the cascade flow under the influence of AVDR (three dimensional in essence) and the limitation of attaining the desired two-dimensional cascade flow by sidewall air removal could be realized from this earlier work. Later, in a review of the earlier cascade testing work, Gostelow [1] clarified that it was the influence of AVDR that caused the discrepancy between American and British test results, indicating that AVDR was an indispensable factor to be considered when comparing cascade test data obtained from one tunnel facility to another.

Besides the pioneering efforts of Gostelow, only a few studies focusing on the AVDR effect are found from open literature (Fottner [80], Stark [81], Heilmann [82], Starcken et al. [83], Stark and Hoheisel [84]). On one hand, the Normal AVDR Influence was observed in most cases of these studies, which backed the conventional viewpoint. On the other hand, some specific results from these studies suggested this issue was more complicated than could be simply concluded by the Normal AVDR Influence and solved by endwall air removal. Heilmann [82] investigated the influence of AVDR on the performance of compressor cascades for different boundary layers and found that the

change in cascade performance with AVDR substantially depended on the blade boundary layer behavior, i.e., the AVDR influence was coupled with the flow nature due to the blade. In testing a high turning compressor DCA cascade, Starken et al. [83] obtained three different loss variation trends with AVDR, given different flow speed, flow angle, and AVDR range: with increasing AVDR, (i) the normally encountered loss drop, (ii) parabolic loss variation, and (iii) nearly constant loss. They also tested with three different sidewall slot-opening configurations and found that the AVDR influence differed from one configuration to another. Stark and Hoheisel [84] investigated the combined effect of AVDR and AR (Aspect Ratio). They found that it was AR that defined the axial velocity distribution through the cascade at a given wall shape and contraction ratio, and it was the axial velocity distribution that decisively determined the local values of pressure distributions as well as the cascade overall parameters like turning angles and loss coefficients. This research provided another reminder that only AVDR is insufficient to fully define the cascade flow two-dimensionality, thus the control of AVDR to improve the cascade test quality helps in a relative sense.

The influence of AVDR was observed and taken into account in later cascade tests. The normal trend that higher AVDR causes the up-shifting of blade surface Mach number distribution was observed on CDA (controlled diffusion airfoil) compressor blades (Hobbs and Weingold [50], Weingold and Behlke [85]). Schreiber et al. [86] employed slotted sidewall suction to control AVDR in an experimental investigation of the effects of Reynolds number and free-stream turbulence on boundary layer transition in a compressor cascade. Hoheisel and Seyb [43] obtained different variation trends of losses with AVDR for a wide AVDR range of 0.9-1.3 and inlet Mach number range of 0.3-0.9 on a highly cambered DCA (Double Circular Airfoil) compressor blade (similar to what was found by Starken et al. [83]). Schreiber and Starken [39] and Steinert et al. [52] found that although the blade surface pressure distribution was considerably influenced by AVDR, the total pressure losses changed only very little. Thus, the loss development characteristics with inlet Mach number and incidence angle were tested with solid sidewalls without control of AVDR. Katoh and Hamatake [44] did not employ sidewall air removal either to control AVDR in their tests of two compressor cascades as AVDR hardly changed in the tested inlet Mach number range (0.60-0.87). Although

AVDR varied between 1.05 and 1.15 for different inlet flow angles, the two cascades had similar AVDR values at each inlet flow angle. Therefore, they claimed that the experimental evaluation of the performances of the two cascades was free of AVDR influence, and the performance change observed was due to the blade profile instead of being biased by the AVDR influence. Katoh's work showcased an example of the applicability of solid sidewall cascade testing.

Tweedt et al. [42] presented results of the influence of AVDR on shock locations in a supersonic compressor cascade. They found a lowering of Mach numbers in the passage with increasing AVDR, which was opposite to the results for subsonic flow. Similar conclusions were obtained by Küsters and Schreiber [45] and by Schreiber and Starcken [40] in investigations of strong shock boundary layer interaction of supersonic compressor cascades.

A.1.2 Motivations of the Study

The complexity of the AVDR influence and the difficulty of excluding it in cascade test practice can be substantially sensed from previous research. In the current cascade testing of the high-turning compressor blades, the same challenge was faced. A lot of efforts have been used to ensure the cascade performance evaluation not be biased by the existing AVDR influence and to better understand the associated flow physics. For this purpose, solid and slotted sidewalls were used in the tests, with the aid of flow diagnostic experiments and 2-D/3-D CFD investigations.

As shown from the above review of previous research, different cascades or different flow conditions could be associated with different AVDR influences. Meanwhile, there have been very few publications to elaborate on this issue. Particularly, there is not a dedicated study in recent years, to provide an updated view on this issue with incorporation of new cascade testing experience and results. The current experimental and numerical study, with the focus on the AVDR influence on high-turning, high solidity, low aspect ratio compressor cascades, at supercritical flow conditions, is intended to enrich the knowledge of this conventional topic.

Moreover, how to fulfill a successful cascade test under the complicated AVDR influence is probably of greater concern, as providing valid test data to confirm new

blade design is generally the major objective of cascade testing. Therefore, based on the current study and previous related research, this appendix summarizes the methodology to deal with the AVDR influence in modern cascade testing.

A.2 Experimental and Numerical Methods

The experimental apparatus and procedures employed for this study have been detailed in Chapter 2. All the numerical results used in this appendix are provided by Sonada and Arima [87] using the Honda in-house steady Navier-Stokes solver. 2-D CFD computation provided the ideal 2-D flow results (AVDR=1.0) while 3-D CFD characterized the essentially 3-D cascade flow in the test section with solid sidewalls. Thus, the sidewall secondary flow and the ensuing flow contraction across the blade passage were simulated (AVDR >1.0). Detailed analysis of the AVDR influence on the flow was performed through the comparison of experimental and numerical results, including losses, blade surface Mach number distribution, blade surface flow visualization and shadowgraph.

2-D CFD method was briefed in Section 1.1.3. 3-D CFD solved 3-D steady Reynolds-Averaged Navier-Stokes (RANS) equations, with matching the experimental conditions (inlet Mach number, inlet freestream turbulence level, and inlet flow sidewall boundary layer thickness) by iteration. The inlet boundary layer thickness was set using $1/7^{\text{th}}$ law by assumption of a full turbulent boundary layer at the inlet. For additional information about the Navier-Stokes solver, refer to Arima et al [14].

A.3 Results Discussion

The following presents the results for the two blades, the baseline (ORG) and the optimized (ES). As already shown before, cascade test results have confirmed significant loss reduction from the baseline to the optimized blade at higher supercritical flow conditions, well covering the design condition ($M_1 = 0.87$, $\alpha_1 = 48.4^\circ$). With presenting the solid/slotted sidewall experimental results and 2-D/3-D CFD results, the focus of this appendix is placed on the AVDR effect and how it influences the performance evaluation for the two blades. As the other optimized blade MOGA shares similar flow

characteristics and performance as the blade ES, the discussion and conclusion in this appendix apply to MOGA as well.

A.3.1 Solid Sidewall Test

Solid sidewall test results are given in Figure A2 along with the 2-D CFD results, to show loss development with inlet Mach number at the design inlet flow angle (48.4°). The AVDR calculated from the measured parameters in the experiment varied with M_1 while the AVDR of 2-D CFD was unity. EXP AVDR variation is 1.03 – 1.14 for the baseline blade and 1.05 – 1.13 for the optimized blade. It is seen that not only the AVDR range of the two blades are almost the same, but also the variation trends are similar. At the same inlet Mach number, AVDRs of the two blades are close. Therefore, relative evaluation of the blade performance can be fulfilled by back-to-back comparison of solid sidewall test data.

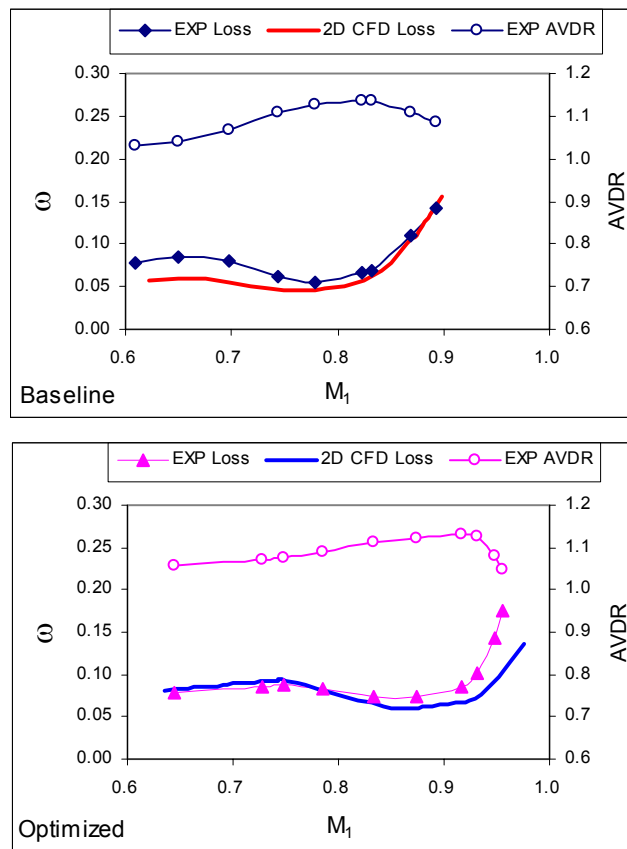


Figure A2 Loss and AVDR development with inlet Mach number at the design inlet flow angle (48.4°)

Both experimental and 2-D CFD results indicate the superiority of the optimized blade, i.e., the optimized blade remains low losses up to a much higher inlet Mach number of 0.93, well covering the design inlet Mach number of 0.87. In contrast, the baseline has low losses only up to inlet Mach number of 0.83. Both experimental and 2-D CFD results also exhibit the same loss- M_1 trend, although the quantitative comparison is not good for the baseline blade at low M_1 or for the optimized blade at high M_1 . The general agreement between experimental and 2-D CFD results suggests the AVDR influence in solid sidewall testing might not be the decisive factor in the loss evaluation of the two blades. The clarification of this will be seen in the following discussion.

A.3.2 Slotted Sidewall Tests

At the design condition, the effect of AVDR on losses was examined by slotted sidewall tests. 2-D and 3-D CFD results are also provided for comparison. Figure A3 shows the experimental and CFD results of losses at different AVDRs. For experimental results, the lowest AVDR data point of each blade was obtained with the maximum sidewall air bleed that the facility allowed, while the highest AVDR data point corresponded to solid sidewall condition. In spite of the same slot opening configuration and similar air bleed rate, different AVDR range and effect of AVDR on losses are noticed for the two blades, due to different blade profiles and different interactions between the mid-span flow and sidewall secondary flow of the two blades. As such, both experiment and 3-D CFD had higher AVDR values for the optimized blade. With the AVDR effect taken into account, both experiment and CFD still showed loss reduction from the baseline to the optimized blade, the same conclusion as drawn based on solid sidewall tests. The higher losses of 2-D CFD than 3-D CFD accord with the Normal AVDR Influence, since 2-D CFD has lower AVDR. The quantitative disagreement between experiment and CFD results will be explained in the later discussion.

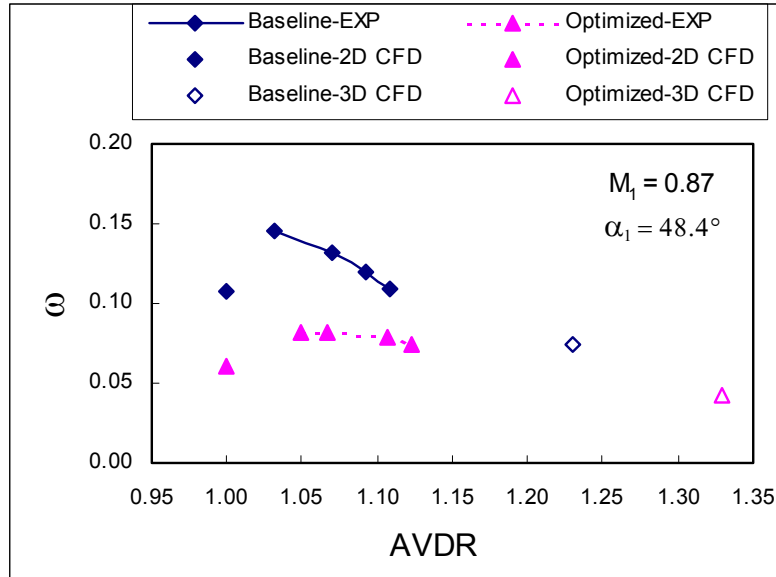


Figure A3 Loss variation with AVDR at the design condition

A.3.3 Flow Behavior with the AVDR Effect

Solid and slotted sidewall test data, as well as 2-D and 3-D CFD results agreeably indicated the superiority of the optimized blade to the baseline blade, even with the AVDR influence. Nonetheless, more flow analysis is necessary for better understanding of the existing quantitative discrepancy.

Strong three-dimensionality of the cascade flow for the two blades under solid sidewall condition has been exhibited by blade surface flow visualization and 3-D CFD flowfield simulation. Figure A4 shows the experimental and 3-D CFD blade suction surface flow visualization at the design condition. General agreement is observed between experimental and CFD results. The streaky patterns left on the blade suction surface show strong sidewall secondary flow and overall flow contraction across the blade. The optimized blade has stronger flow contraction than the baseline blade, thus its AVDR is higher correspondingly. Reverse flow was observed on the baseline blade suction surface during the tunnel run and predicted by 2-D and 3-D CFD as well, confirming the boundary layer separation and accounting for the much higher losses. No

reverse flow occurred for the optimized blade according to the experimental blade surface flow visualization and 2-D/3-D CFD calculations.

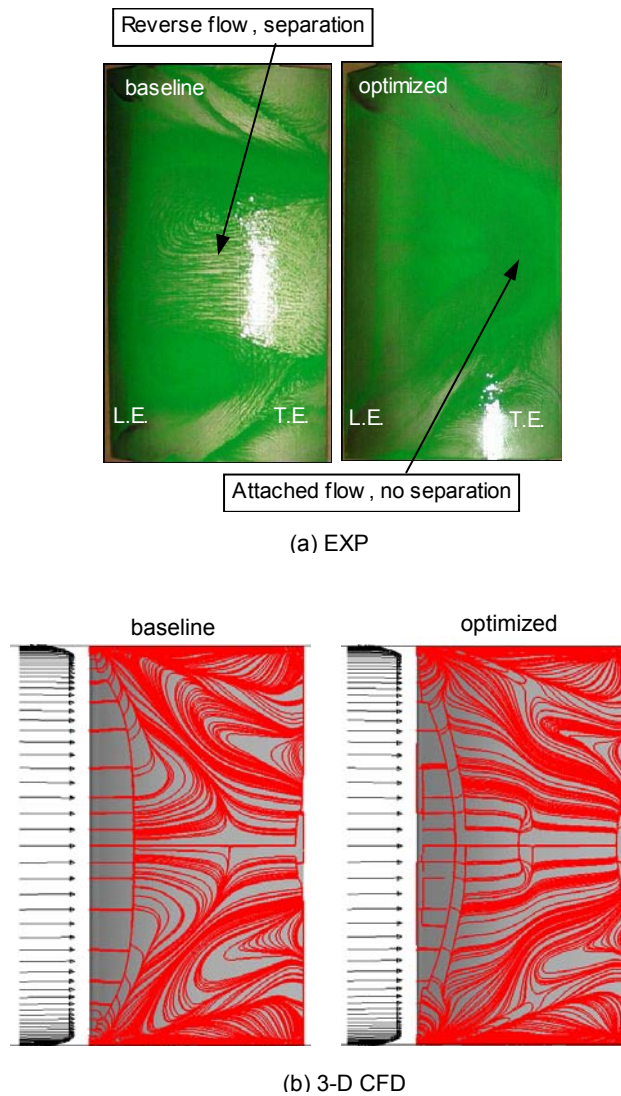


Figure A4 Blade suction surface flow visualization at the design condition

Figure A5 is the 3-D CFD results to visualize the three-dimensional flow across the passage. The yellow surface in the figure is the computed iso-surface where the axial velocity is equal to zero, thus it illustrates the reverse flow region. It is seen that even with endwall effects and the consequent overall flow contraction ($AVDR > 1.0$) cross the passage, uniform flow could be still present in the mid-span flow tube. Similar results

were published by Weber et al. [88] in a low turning transonic compressor cascade and Cyrus [89] in a subsonic compressor cascade.

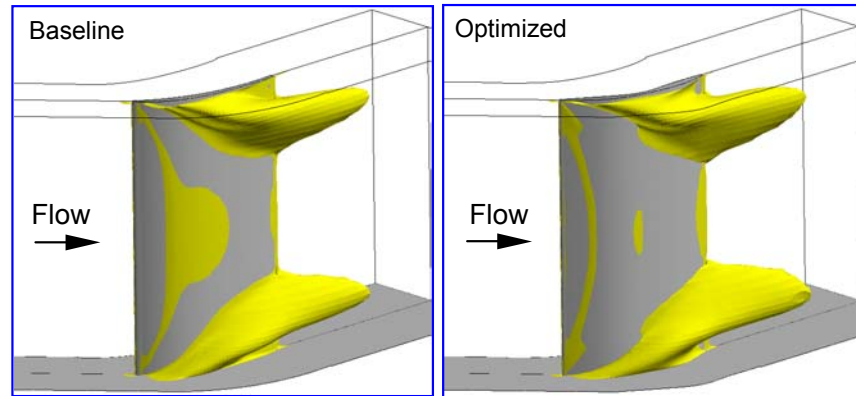


Figure A5 3-D CFD flow visualization at the design condition

CFD Mach number contours of the two blades at the design condition are given in Figure A6. The contours of 3-D CFD are at the mid-span plane. It should be noted the AVDRs of the solid sidewall test results lie between those of the 2-D and 3-D CFD. Therefore, the conclusion based on Figure A6 should be on the conservative side when it is applied to the effect of AVDR on the experimental results with solid sidewalls. As seen in Figure A6, the essential flow difference between the two blades was predicted by both 2-D and 3-D CFD. For the baseline blade, both 2-D and 3-D CFD revealed the strong passage shock and the shock-induced boundary layer separation on the suction surface. For the optimized blade, both 2-D and 3-D CFD revealed the leading edge shock/passage shock interaction and attached flow on the suction surface. It can be reasonably speculated the Mach number contours of the flow in the mid-span of solid sidewall test case would lie between the 2-D and 3-D CFD results. Therefore, to compare the performances and of the two blades, solid sidewall testing would be acceptable, as it captured the flow characteristics of first-order importance. The results shown in Figure A6 also suggest the Normal AVDR Influence. For the baseline blade, due to the flow contraction, 3-D CFD has less degree of separation on the blade suction surface, thus lower losses than 2-D CFD. For the optimized blade, 3-D CFD has the thinner boundary layer on the blade suction surface, thus lower losses than 2-D CFD.

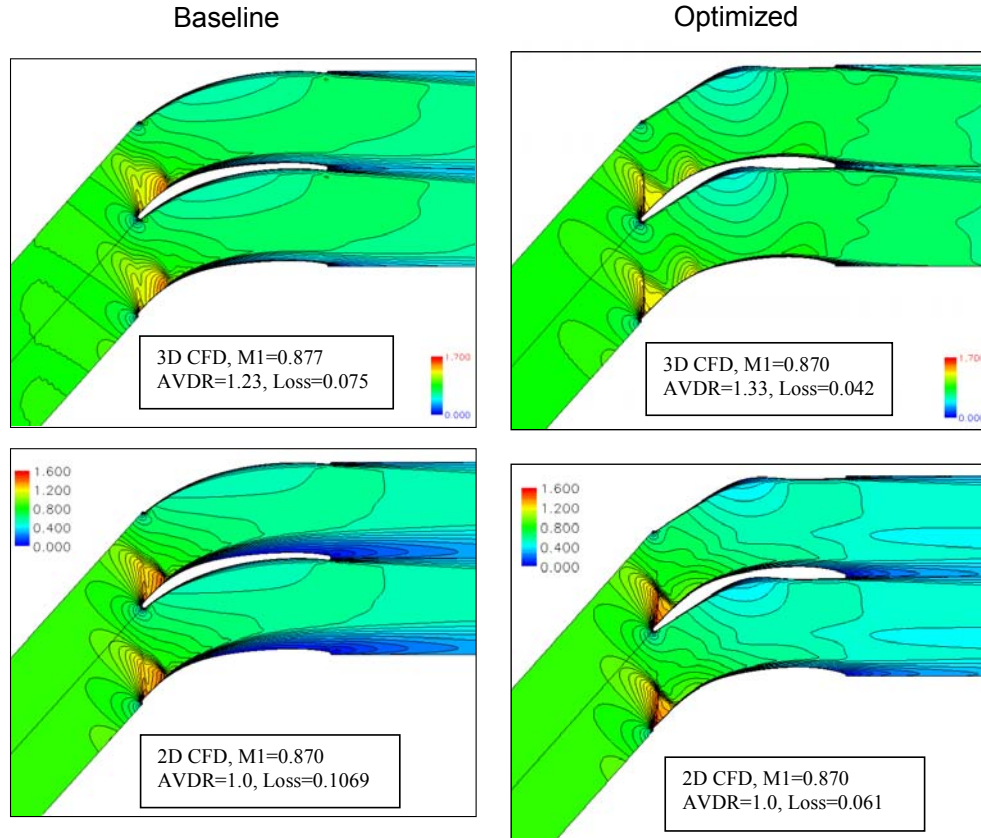


Figure A6 Mach number contours at the design condition

Another examination of the flow with the AVDR effect is fulfilled by shadowgraph technique. As shown in Figure A7, 2-D CFD, 3-D CFD and EXP give similar shock patterns for both blades at the design condition, although AVDRs are different in the three cases. The shadowgraphs provide strong evidence that the AVDR effect has little influence on the shock patterns. For a supercritical cascade, the shock pattern at front part of the blade is an essential factor affecting the flow behavior (boundary layer development and losses). Thus, similar shock patterns of each blade at the three cases suggest that the AVDR influence on the flow is of second-order importance from this perspective.

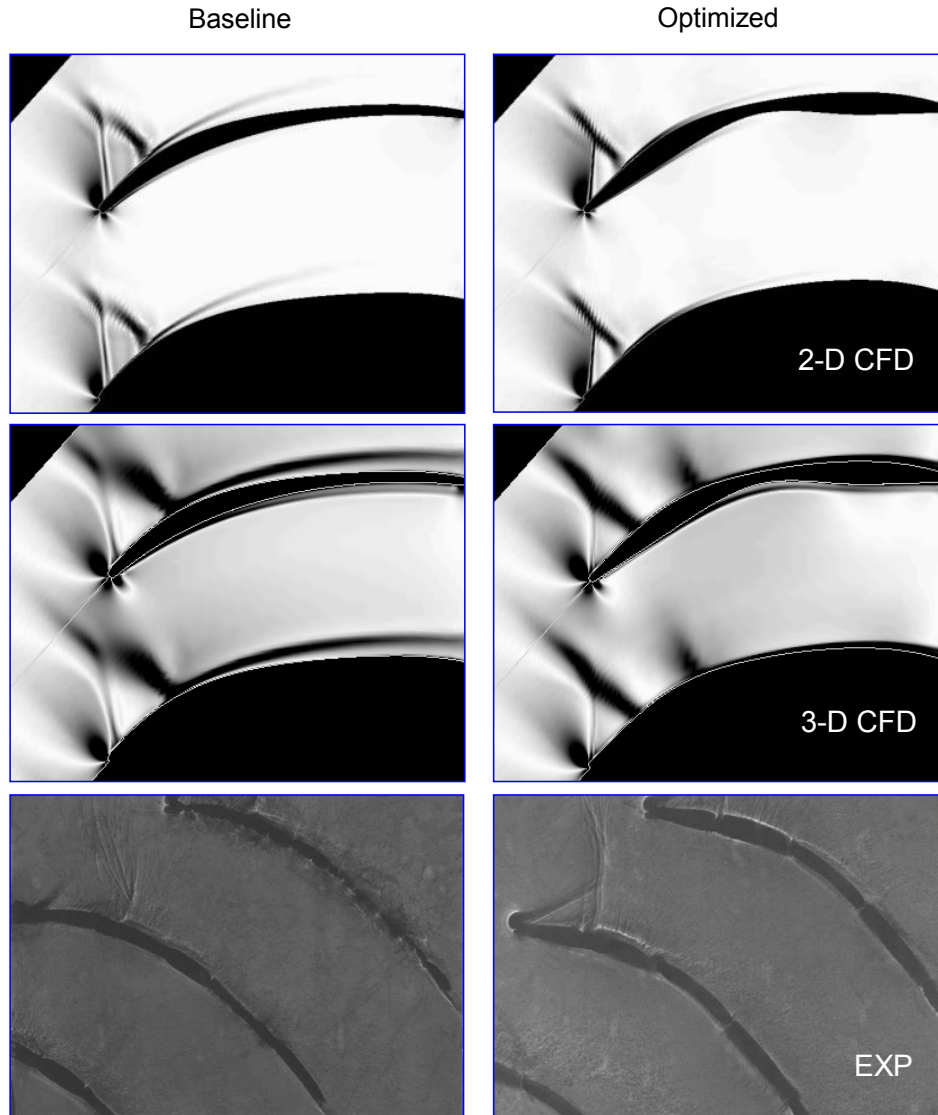


Figure A7 Shadowgraphs at the design condition

Summarizing the results shown in Figure A4, A5, A6, and A7, it can be concluded that the three-dimensionality of the flow at the design condition with solid sidewalls is strong and the AVDR influence is observable. However, the existing AVDR influence does not seriously trouble the relative performance evaluation for the two blades, as the essential flow characteristics due to blade profiles, such as boundary layer separation or not, and shock pattern are conserved in the mid-span, where the measurements are taken. This flow nature conservation makes the seemingly doubtful

solid sidewall testing to be actually acceptable in the current work. It is worth further pointing out that, more generally, this point is the key criterion for inspecting the validity of a cascade test, regardless of what sidewall conditions involved. In fact, Schreiber and Starcken [40] once claimed that manipulating the cascade flow by different sidewall openings was no problem if the endwall effects were of minor influence on the mid-span flow region.

A.3.4 Blade Surface Mach Number

Blade surface Mach number is generally used as the key criteria in the blade design process. It can be also used to provide most important information of cascade flow and can be measured with relative ease. As such, it has been used as a flow diagnostic tool in cascade testing. Two application examples were from Weingold and Behlke [90] and Steinert et al. [91]. Similarly, it is used in the current study to further inspect the AVDR influence.

Figure A8 shows experimental (with solid sidewall condition) and CFD results of blade surface isentropic Mach number distribution at the design condition. The Normal AVDR Influence is clearly seen, i.e., higher AVDR corresponds to the up-shifted blade surface Mach number. It should be emphasized that this AVDR influence on blade surface Mach number distribution has been unanimously seen from previous research, indicating the suitability of blade surface Mach number distribution to characterize the flow with the AVDR influence.

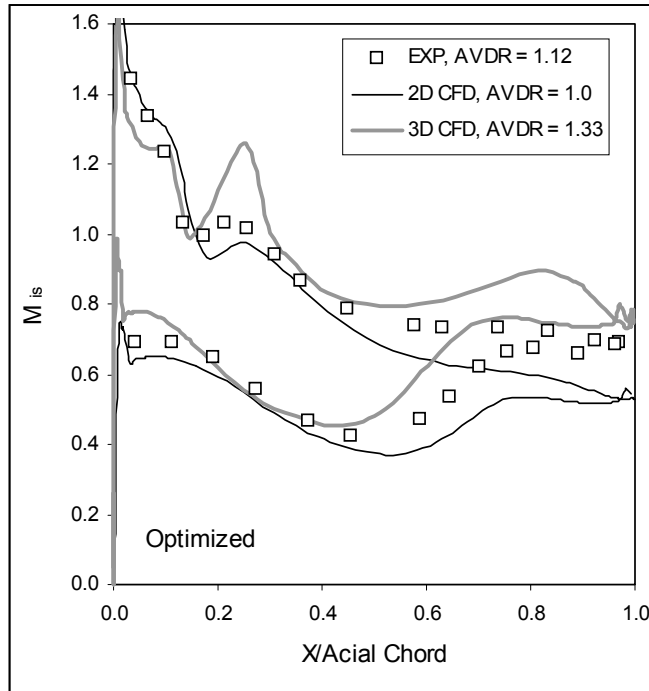
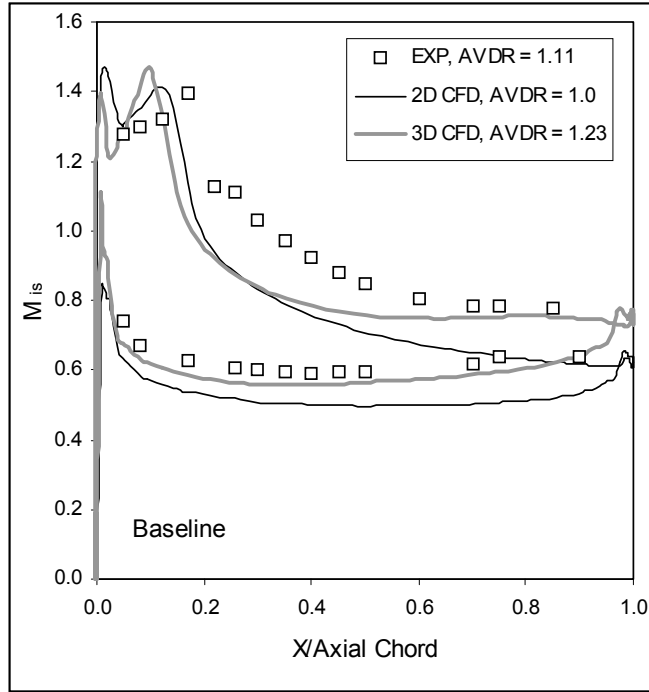


Figure A8 Blade surface Mach number at design condition

Baseline Blade Case

Experiment agrees better with 3-D CFD than 2-D CFD, which is accordant to the Normal AVDR Influence. However, 3-D CFD has still lower surface Mach number although its AVDR is higher than experiment. This trend is opposite to the Normal AVDR Influence. The reason is perhaps due to the under-prediction of the boundary layer separation by 3-D CFD. It should be pointed out that in addition to the AVDR influence, boundary layer separation is another factor that affects blade surface Mach distribution. As normally seen, from the separation onset, surface Mach number up-shifts, and the stronger separation (less diffusion), the more up-shifting. In the current case, severe boundary layer separation happened on the baseline blade suction surface, a great challenge for accurate CFD calculation. The difficulty lies in the limitation of contemporary CFD in terms of imperfect turbulence models and inaccuracy of computing the flow in the strong mixing regions, such as in separated boundary layers and wakes. In the CFD computation of the thesis work, the separation and losses were over-predicted using ADPAC, leading to higher predicted blade surface Mach number. The inaccuracy of the Honda CFD calculation is also seen from the passage shock location, which was predicted more upstream than the measured location. It is worth mention, however, that at lower speeds or without boundary layer separation, the two CFD codes have much better prediction of the flow. Therefore, care should be exercised when inspecting the AVDR effect using 2-D and 3-D CFD results of blade surface Mach number at critical flow conditions (such as with strong separation), as the possible under-prediction or over-prediction, if not perceived, would cause misunderstanding.

Based on the above discussion, the baseline blade surface Mach results shown in Figure A8 and the loss results shown in Figure A2 and A3 could be explained. First, both 2-D and 3-D CFD under-predicted the boundary layer separation and hence the losses. Second, AVDR still applies the normal influence on the losses and blade surface Mach number distribution. Thus, the obtained results seen in Figure A2, A3 and A8 are the combined effect of AVDR and the CFD under-prediction. The under-prediction seems to dominate such that the 2-D and 3-D CFD have lower losses and lower surface Mach number (more diffusion) than experimental results. Nonetheless, the Normal AVDR

Influence can be still seen, i.e., 3-D CFD has lower losses and up-shifted blade surface Mach number distribution in comparison with 2-D CFD results.

Optimized Blade Case

The Normal AVDR Influence is better shown in this case. The optimized blade has been confirmed of no boundary layer separation at the design condition. The flow was predicted with higher accuracy, either by the Honda CFD or ADPAC. As such, the AVDR influence in this case has been less clouded by the under-prediction. Experimental results reasonably lie between the 2-D and 3-D CFD curves as experiment has an intermediate AVDR value. For 3-D CFD, blade surface Mach number distribution has significant up-shifting, and the re-acceleration after the passage shock was exaggerated (the peak at about 30% chord), as can be also noticed in Figure A6. This is due to the much higher AVDR (1.33) of the simulated 3-D flow. It can be reasonably speculated that if 3-D CFD could obtain a lower AVDR solution, a better agreement between CFD and experiment should be obtained. For 2-D CFD, loss is lower than experimental value (see Figure A3), and this is due to the CFD under-prediction, but in less degree such that the loss difference between 2-D CFD and experiment is not as large as for the baseline case. The under-prediction and the Normal AVDR Influence caused 2-D CFD blade surface Mach number to be lower than experiment.

A.3.5 Summary with Additional Notes

The cascade flow contraction due to the blockage of the endwall boundary layer and/or secondary flow can be sufficiently appreciated from previous research and the current study. The AVDR influence in the sense of making the cascade flow deviate from the ideal 2-D flow is incontrovertible. Removing some amount of air through the endwalls (slotted or porous) by suction or bleed, employing divergent test section, or choosing high aspect ratio of the blade all seem to be appropriate measures to manipulate the flow towards closer to the 2-D nature in most cases. However, this goal cannot be perfectly achieved due to the complexity of the AVDR influence and the facility limitation in obtaining ideal 2-D flow in cascade test practice. The control of AVDR helps only in a relative sense.

Different AVDR influence, i.e., different flow behavior and blade performance under the three-dimensional effect from sidewalls could result, given different blades, flow conditions, facilities and sidewall air removal procedures. This was seen from previous research as well as the current work. As shown in Figure A3, the two blades had different AVDR values although the same slot opening configuration and air bleed rate were used. Extra efforts were used to force the AVDR to be equal for the two cascades, i.e., enlarging the slots or increasing air removal amount, but were proved to be unsuccessful. For example, when the sidewall slot opening was enlarged more than 50% chord in length, air was sucked in the passage at upstream location while bled out at downstream location, causing flow circulation across sidewalls. This was neither good for the desired 2-D uniformity nor helpful for improving the comparability of the tested blades. Similar results were found by Starken et al. [83]. The AVDR influence was also found to be sensitive to the flow incidence. At negative incidences, the flow contraction over the blade passage decreases; thus AVDR reduces accordingly (even smaller than unity in some cases). This trend was seen from experimental and 3-D CFD results in the current work. Recently, Jouini et al. [92] published the same AVDR variation trend for transonic turbine cascades. Apparently, sidewall air removal is unnecessary in this kind of negative incidence case.

Based on the current study and previous research, three typical cases regarding the AVDR influence can be summarized. Case I: with the variation of AVDR, both losses and blades surface Mach number are significantly influenced. This is the most frequently encountered case, as seen in most of the previous research and for the baseline blade of the current work at the design condition. In this case, controlling AVDR is necessary and helpful. Case II: a limited AVDR variation causes distinct blade surface Mach number shifting but slight influence on losses [39, 52, 83]. This also applies on the optimized blade ES of the current work at the design condition. In this case, controlling AVDR is desirable but not a necessity. Case III: a limited variation of AVDR has such a small influence on both blade surface Mach number and losses that the influence can be neglected. This case would happen for native incidences and/or low Mach number numbers. Controlling AVDR is unnecessary and solid sidewall testing would give satisfying results. One example is given in Figure A9, the blade surface Mach number

distribution of ES at $M_1 = 0.75$. Experimental data obtained with solid sidewall condition (AVDR=1.07) agrees with 2-D CFD (AVDR=1.0) very well except for a slight up-shifting at the aft part of the blade, which is due to the insignificant flow contraction in the experiment. The correspondingly good agreement of the losses between experiment and 2-D CFD can be seen from Figure A2.

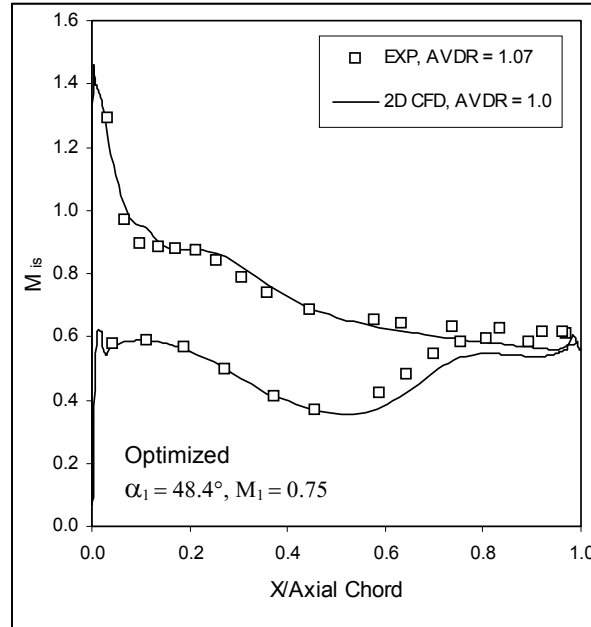


Figure A9 Blade surface Mach number at lower inlet Mach number

Facing the complexity of the AVDR influence in cascade testing and the difficulty to manipulate the flow free of the influence, this topic could be better summarized as one point: to deal with the AVDR influence in two-dimensional linear cascade testing, the key is to check out if the intrinsic flow nature due to the tested blade profile is conserved in the mid-span flow tube, where measurements are taken. If it is, the test should be free of AVDR influence (at least of first-order importance), regardless of solid or slotted sidewalls used. In some cases, solid sidewalls without controlling AVDR do meet this criterion, thus making an economical and acceptable test, as showcased by the current work. To ensure the key point, experimental flow diagnosis such as blade surface flow visualization, Schlieren/Shadowgraph, and blade surface Mach number, with comparison to 2-D and 3-D CFD results, would help.

There are other occasions to use solid sidewall testing. When a cascade test program is intended to evaluate the relative performances of different blade profiles, solid sidewall test data would qualify if the tested blades had similar AVDR at the same flow condition (speed and incidence), although AVDR might vary with the flow speed or incidence. The application examples are from Katoh and Hamatake [44] as well as the current work (see Figure A2). Moreover, testing blades with AVDR greater than unity is desired sometime when the tested blade profile is for application in the near hub or tip region of the turbomachine.

In general, in dealing with the AVDR influence in cascade testing, how to choose an appropriate strategy depends upon many factors, such as the test objective, facility capacity, and available resources. Usually, comparing cascade data from one tunnel facility to another requires more rigorous test conditions and necessitates the expensive tests with AVDR well controlled. However, not all cascade wind tunnel facilities in service have sidewall air removal capability. Even for those with the capability, sufficient air removal (either by suction or bleed) for a wide range of AVDR control or for high flow speeds seems to be a problem due to the limited air removal capacity. Therefore, the following strategy is recommended: For low flow speeds or negative incidences, AVDR could be close to unity thus no need for sidewall air removal. Or if AVDR is similar at each specific flow condition, relative evaluation of the blades using solid sidewall tests is still doable. Even at critical flow conditions coupled with strong three-dimensional effect, solid sidewall testing is applicable if the key criterion as addressed above is met. For this purpose, conducting additional flow diagnostic measurements plus the aid of CFD flow analysis should be a practical and affordable means to be taken.

A.4 Closure

An experimental and numerical study of the effect of AVDR in cascade testing of two high-turning compressor blades ORG and ES was conducted at supercritical flow conditions. Different AVDR influences were found on the two blades due to their different aerodynamic performances and different interactions between the mid-span main flow and the sidewall secondary flow. At the critical design condition at which strong three-dimensional effect exists, the essential flow characteristics, such as whether of not the boundary layer separated and the shock pattern, are conserved in the mid-span flow tube in spite of the AVDR influence. In addition, the range and trend of AVDR variation with inlet Mach number of the two blades are similar. At lower speeds or negative incidences, AVDR is closer to unity (less three-dimensional effect). Therefore, solid sidewall testing is acceptable to evaluate the performances of the two blades in the current work.

The AVDR influence in cascade testing is complicated and case-dependent with many affecting factors, such as tunnel facility, test section configuration, sidewall air removal configuration and procedure, cascade/blade geometry, and flow conditions (velocity and flow angle). There is never an all-purpose method or procedure to follow. The appropriate strategy taken to successfully achieve the test objective should be based on the case study and resource availability. Sidewall air removal, an effective method as conventionally ascertained, can be used if it is available. But this does not exclude the applicability of solid sidewall testing. As demonstrated by the current work, when the key criterion (flow nature conservation in the mid-span despite 3-D endwall effect) is satisfied, solid sidewall testing would be adequate. Additional flow diagnostic measurements with the aid of 2-D and 3-D CFD flow simulation are necessary to establish more confidence in the test. This methodology, when used properly, should be favored in cascade testing due to its cost-effectiveness and feasibility. Its application will become more promising with the increasing progress of modern CFD techniques.

Appendix B Angle Probe Design and Calibration

Two angle probes were used in the experiments to measure the cascade inlet and outlet flow angle respectively. One is a commercial prism three-hole probe, used to measure the inlet flow. The other is a specially designed conical three-hole probe, with the desired geometry for the outlet traverse measurement. The two probes were calibrated in a high speed nozzle setup, as shown in Figure B1. The angle probe was placed in the middle of the nozzle. A standard Pitot-static probe was placed beside the angle probe to measure the total and static pressure for reference. Before the calibration, the flow was checked to be uniform in the middle area of the nozzle. Different setting angles of the angle probe to the flow (i.e., different flow angles if fixing the coordinate with the angle probe) were obtained using an angular traverse that has the accuracy of $\pm 0.1^\circ$. At each flow angle, different Mach numbers were tested which cover the Mach number ranges involved in the experiments.

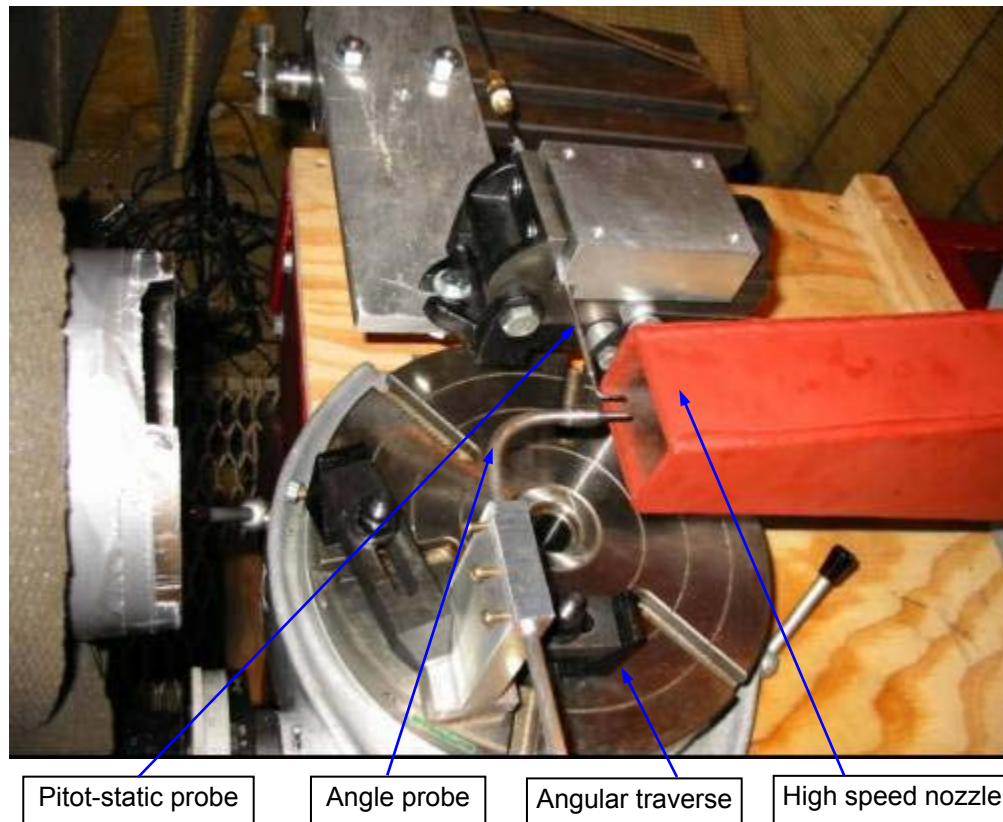


Figure B1 Angle probe calibration setup

The conical angle probe design is shown in Figure B2. The probe head was made with a diameter of 1/8" with the trade-off consideration of the flow interference and machining difficulty. The center hole was made with a divergent opening good for Pt measurement) while the two side holes were made with sharp openings (good for flow angle measurement).

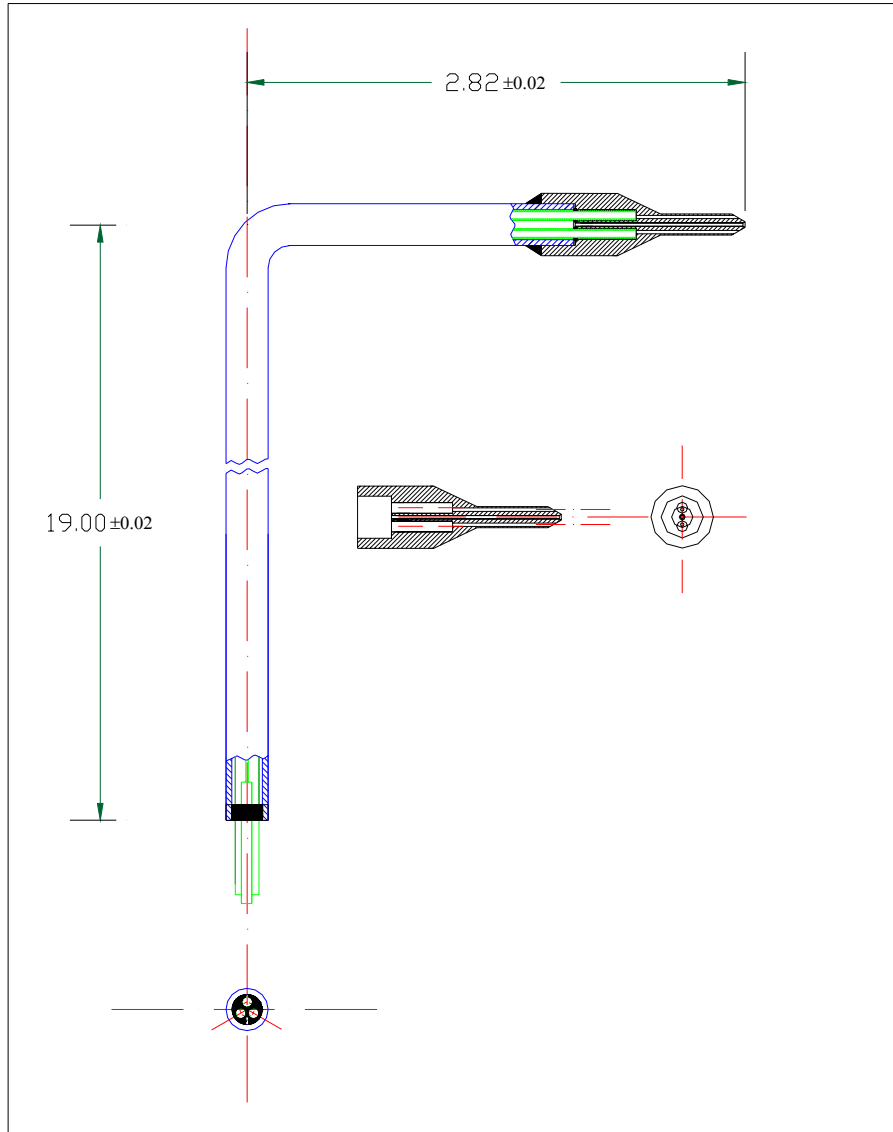


Figure B2 Conical angle probe design for outlet traverse measurement

The measured data from the calibration test was reduced into correlations to calculate the flow total pressure, static pressure and flow angle, based on the three pressure readouts from the three holes. The parameter definitions used in the calibration correlations are listed in the following:

Pitot-static probe

Pt – total pressure

Ps – static pressure

Prism angle probe

P2 – left-side-hole pressure readout

P3 – right-side-hole pressure readout

P1 – center-hole pressure readout

$P_m = 0.5(P_2 + P_3)$ – nominal mean pressure head

$Q = P_1 - P_m$ – nominal dynamic pressure head

$f_1 = (P_2 - P_3)/Q$ – angle parameter

$f_2 = (P_t - P_1)/Q$ – total pressure parameter

$f_3 = (P_s - P_m)/Q$ – static pressure parameter

Conical angle probe

Pu – upper-side-hole pressure readout

Pd – down-side-hole pressure readout

Po – center-hole pressure readout

$P_m = 0.5(P_u + P_d)$ – nominal mean pressure head

$Q = P_o - P_m$ – nominal dynamic pressure head

$f_1 = (P_u - P_d)/Q$ – angle parameter

$f_2 = (P_t - P_o)/Q$ – total pressure parameter

$f_3 = (P_s - P_m)/Q$ – static pressure parameter

The correlations for the two probes are obtained based on the calibration data from the reference Pitot-static probe and the angle probe. Figure B3 and B4 show the correlations of the two probes respectively. In application, based on the three pressure readouts from the angle probe, the desired total pressure, static pressure, Mach number and flow angle can be calculated out using the correlations. A Matlab program for each probe was prepared to do the calculations, in which numerical iteration and three-order spline interpolation were adopted to get the convergent solutions. The programs are attached.

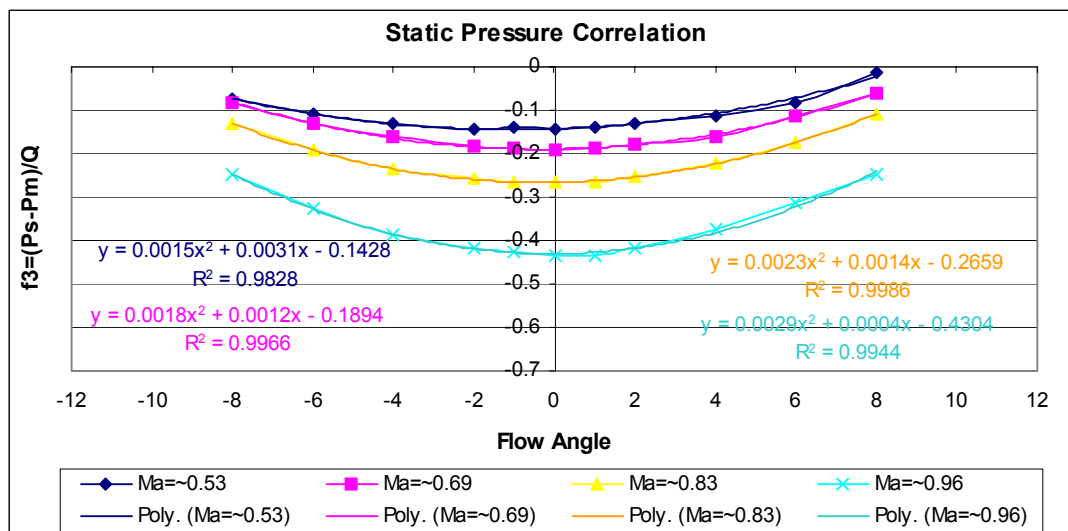
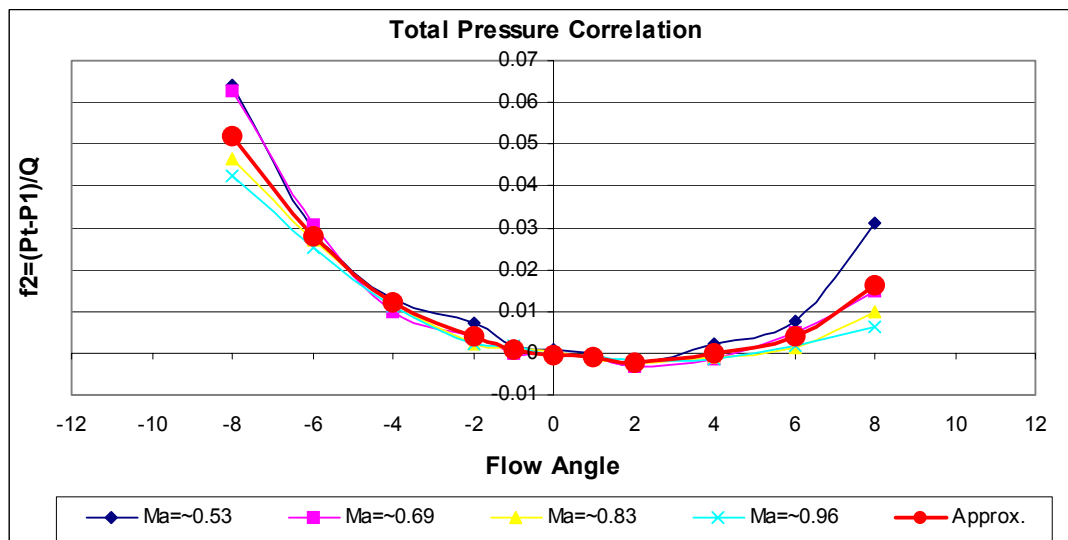
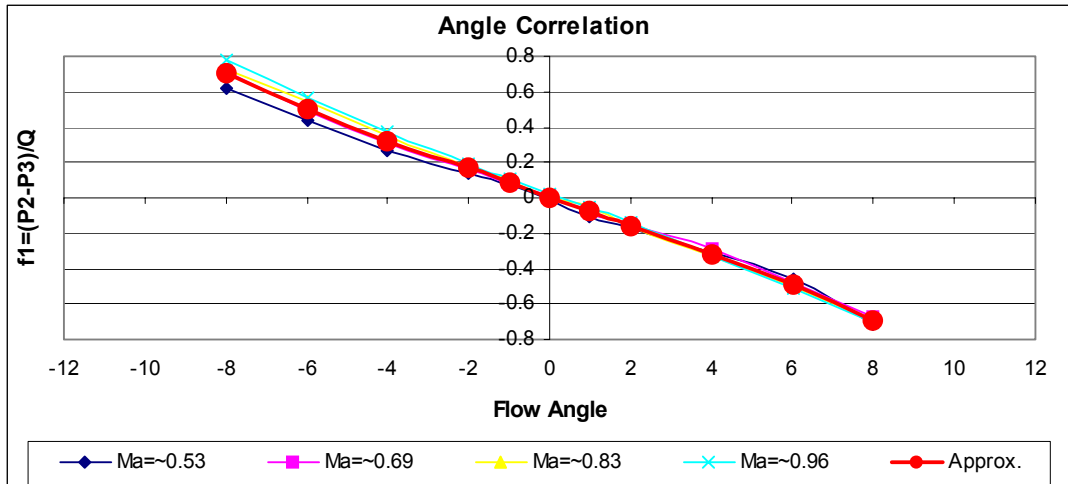


Figure B3 Correlations for the prism probe

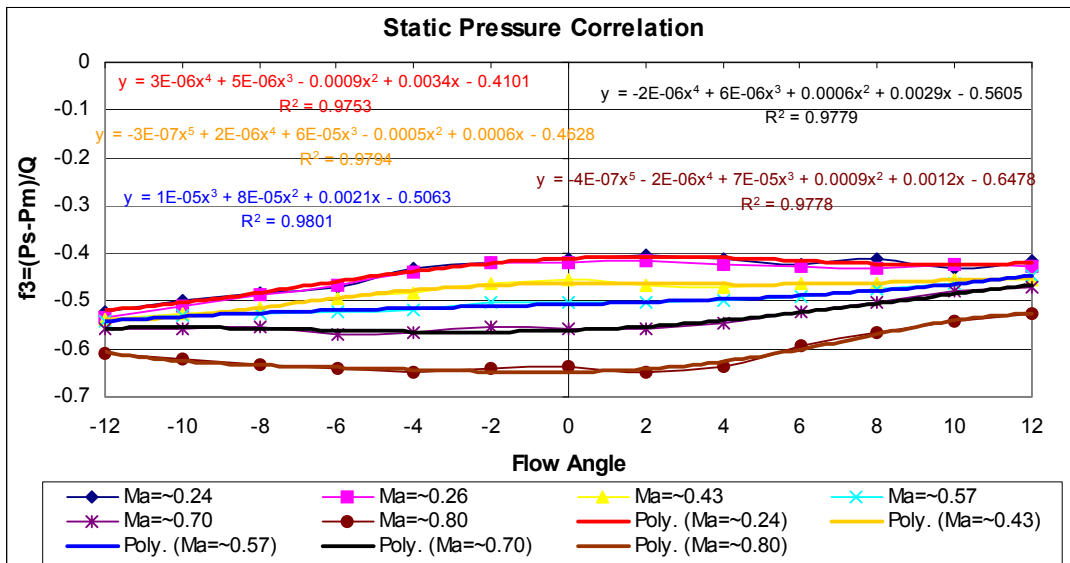
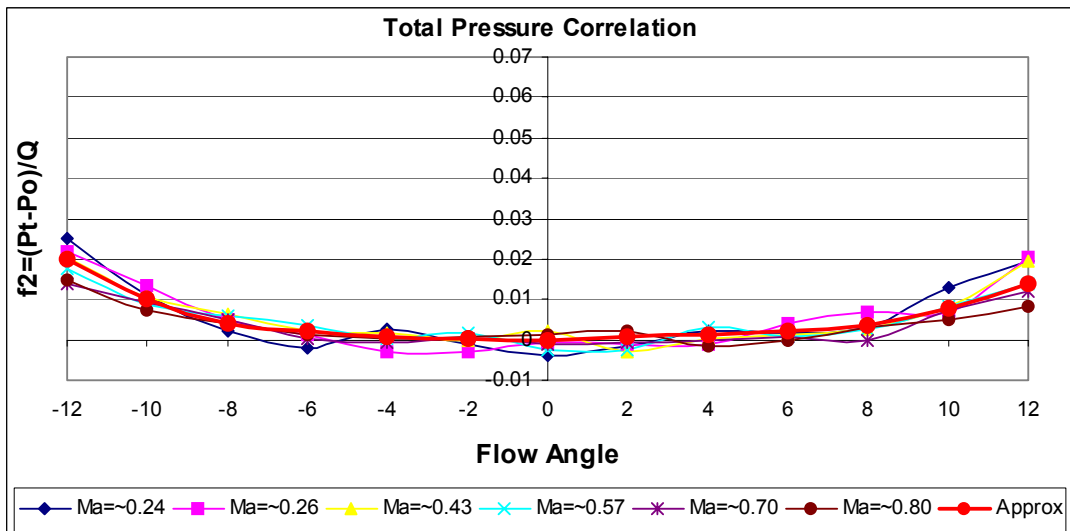
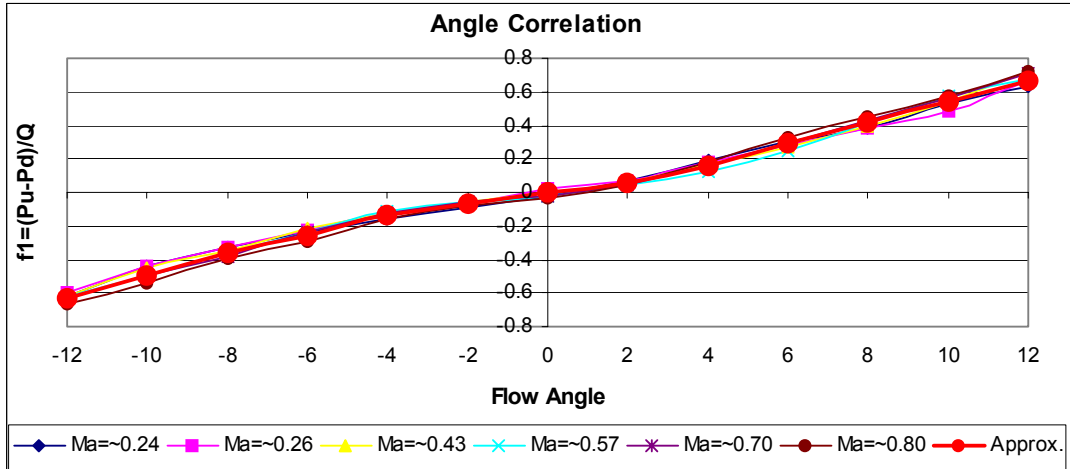


Figure B4 Correlations for the conical probe

Matlab program for data reduction for the prism angle probe

```
-----  
% Prism Angle Probe data reduction  
% Input: P1,P2,P3 from load file a.txt  
% Output: Pt, Ps, Ma, Angle(Ang)  
  
I=1000;  
J=100;  
Delta=0.001;  
Patm=13.786;  
load a.txt;  
P1=a(:,1);  
P2=a(:,2);  
P3=a(:,3);  
Ma=[0.53,0.69,0.83,0.96];  
  
Pm=(P2+P3)/2;  
Q=P1-Pm;  
  
f1=(P2-P3)./Q;  
Ang=-11.822*f1+0.043;  
f2=3e-6*Ang.^4-1e-5*Ang.^3+4e-4*Ang.^2-1.4e-3*Ang-5e-4;  
Pt=f2.*Q+P1;  
  
f3(:,1)=1.5e-3*Ang.^2+0.0031*Ang-0.1428;  
f3(:,2)=1.8e-3*Ang.^2+1.2e-3*Ang-0.1894;  
f3(:,3)=2.3e-3*Ang.^2+1.4e-3*Ang-0.2659;  
f3(:,4)=2.9e-3*Ang.^2+4e-4*Ang-0.4304;  
  
Maini=sqrt(5*((Patm+Pt)./(Patm+Pm)).^(1/3.5)-1));  
ma1=Maini;  
ma2=Maini+0.1;  
  
for i=1:I,  
    i  
    for j=1:J,  
        if abs(ma2(i)-ma1(i))<Delta,  
            j  
            break  
        end  
        ma1(i)=ma2(i);  
        ff3(i)=spline(Ma,f3(i,:),ma1(i));  
        Ps(i)=ff3(i)*Q(i)+Pm(i);  
        ma2(i)=sqrt(5*((Patm+Pt(i))./(Patm+Ps(i))).^(1/3.5)-1));  
    end  
end  
  
Ps1=Ps';  
output(:,1)=Pt;  
output(:,2)=Ps1;  
output(:,3)=ma2;  
output(:,4)=Ang;  
save output output -ascii  
-----
```

Matlab program for data reduction for the conical angle probe

```
-----  
% Conical Angle Probe data reduction  
% Input: Po,Pu,Pd from load file a.txt  
% Output: Pt, Ps, Ma, Angle(Ang)  
  
I=1000;  
J=100;  
Delta=0.001;  
Patm=13.7335;  
load a.txt;  
Po=a(:,1);  
Pu=a(:,2);  
Pd=a(:,3);  
Ma=[0.24,0.43,0.57,0.7,0.8];  
  
Pm=(Pu+Pd)/2;  
Q=Po-Pm;  
  
f1=(Pu-Pd)./Q;  
Ang=50.641*f1.^5+4.6878*f1.^4-38.275*f1.^3-2.8969*f1.^2+25.572*f1-  
0.004;  
f2=7e-7*Ang.^4-2e-6*Ang.^3+1e-5*Ang.^2+1e-4*Ang+4e-4;  
Pt=f2.*Q+Po;  
f3(:,1)=3e-6*Ang.^4+5e-6*Ang.^3-9e-4*Ang.^2+0.0034*Ang-0.4101;  
f3(:,2)=-3e-7*Ang.^5+2e-6*Ang.^4+6e-5*Ang.^3-5e-4*Ang.^2+6e-4*Ang-  
0.4628;  
f3(:,3)=1e-5*Ang.^3+8e-5*Ang.^2+0.0021*Ang-0.5063;  
f3(:,4)=-2e-6*Ang.^4+6e-6*Ang.^3+6e-4*Ang.^2+0.0029*Ang-0.5605;  
f3(:,5)=-4e-7*Ang.^5-2e-6*Ang.^4+7e-5*Ang.^3+9e-4*Ang.^2+0.0012*Ang-  
0.6478;  
  
Maini=sqrt(5*((Patm+Pt)./(Patm+Pm)).^(1/3.5)-1));  
ma1=Maini;  
ma2=Maini+0.1;  
  
for i=1:I,  
    for j=1:J,  
        if abs(ma2(i)-ma1(i))<Delta,  
            break;  
        end  
        ma1(i)=ma2(i);  
        ff3(i)=spline(Ma,f3(i,:),ma1(i));  
        Ps(i)=ff3(i)*Q(i)+Pm(i);  
        ma2(i)=sqrt(5*((Patm+Pt(i))./(Patm+Ps(i))).^(1/3.5)-1));  
    end  
end  
Ps1=Ps';  
  
output(:,1)=Pt;  
output(:,2)=Ps1;  
output(:,3)=ma2;  
output(:,4)=Ang;  
save output output -ascii  
-----
```

Appendix C Uncertainty Analysis

Throughout the experiment and data acquisition, errors were induced from different aspects involving instrument, cascade flow aperiodicity, tunnel facility unsteadiness. The following is an uncertainty analysis of the major parameters and variables measured and used in this research.

Inaccuracies due to instrument precision errors propagated and compounded in the calculations of the final parameters. The original uncertainty range of the instrument and equipment is summarized Table C1. For a certain final parameter, all the related uncertainty terms were summed up by root-mean-square error propagating algorithm to account for the total instrument uncertainty.

Table C1 Uncertainty of instruments and equipments

Measurement	Instrument or equipment	Uncertainty
Pt, Ps, $\Delta Pt(Ptd)$	MKS pressure transducer 20 Psig range	± 0.005 psig
	MKS pressure transducer 3 Psig range	± 0.002 psig
P_{amb}	Kahlsico Precision, Aneroid Barometer MK2	± 0.01 psi
P_{S_s}	PSI 32 Channel Pressure System	± 0.002 psi
T_t	Type K Thermocouple	± 2 K
Setting Angle	Digital Protractor	$\pm 0.02^\circ$
Inlet flow angle	Inlet Angle Probe	$\pm 0.5^\circ$
Outlet flow angle	Traverse Probe	$\pm 0.5^\circ$

Equation 1, 2, 3 given in Chapter 2 define the formula for AVDR, M and ω , of which only AVDR needs to be derived with the measured quantities.

Because

$$\rho = \frac{Pt}{RTt (1 + 0.2 M^2)^{2.5}} \quad (\text{Equation C1})$$

Substituting it into Equation 1

$$AVDR = \frac{\int_0^{2 \text{ pitch}} \frac{Pt_2 M_2 \cos \beta_2}{(1 + 0.2 M_2^2)^3 \sqrt{Tt_2}} ds_2}{\int_0^{2 \text{ pitch}} \frac{Pt_1 M_1 \cos \beta_1}{(1 + 0.2 M_1^2)^3 \sqrt{Tt_1}} ds_1} \quad (\text{Equation C2})$$

Given the assumption of adiabatic flow, Equation C2 is simplified into

$$AVDR = \frac{\int_0^{2 \text{ pitch}} \frac{Pt_2 M_2 \cos \beta_2}{(1 + 0.2 M_2^2)^3} ds_2}{\int_0^{2 \text{ pitch}} \frac{Pt_1 M_1 \cos \beta_1}{(1 + 0.2 M_1^2)^3} ds_1} \quad (\text{Equation C3})$$

This is the final expression used for AVDR calculation.

The uncertainty of total pressure loss coefficient, Mach number, and AVDR are derived from Equation 2, 3, C3, as shown below.

$$\delta\omega = F1 (\delta Pt_1, \delta Ptd, \delta Ps_1) \quad (\text{Equation C4})$$

$$\delta M = F2 (\delta Pt, \delta Ps) \quad (\text{Equation C5})$$

$$\delta(AVDR) = F3 (\delta Pt_1, \delta Pt_2, \delta M_1, \delta M_2, \delta \beta_1, \delta \beta_2) \quad (\text{Equation C6})$$

Equations (C4-6) can be further expressed as

$$\delta\omega = \sqrt{\left[\left(\frac{\partial\omega}{\partial Pt_1} \right) \delta Pt_1 \right]^2 + \left[\left(\frac{\partial\omega}{\partial Ptd} \right) \delta Ptd \right]^2 + \left[\left(\frac{\partial\omega}{\partial Ps_1} \right) \delta Ps_1 \right]^2} \quad (\text{Equation C7})$$

$$\delta M_1 = \sqrt{\left[\left(\frac{\partial M_1}{\partial Pt_1} \right) \delta Pt_1 \right]^2 + \left[\left(\frac{\partial M_1}{\partial Ps_1} \right) \delta Ps_1 \right]^2} \quad (\text{Equation C8})$$

$$\delta(AVDR) = \sqrt{\left[\left(\frac{\partial AVDR}{\partial Pt_1} \right) \delta Pt_1 \right]^2 + \left(\frac{\partial AVDR}{\partial M_1} \delta M_1 \right)^2 + \left(\frac{\partial AVDR}{\partial Pt_2} \delta Pt_2 \right)^2 + \left(\frac{\partial AVDR}{\partial M_2} \delta M_2 \right)^2 + \left(\frac{\partial AVDR}{\partial \beta_1} \delta \beta_1 \right)^2 + \left(\frac{\partial AVDR}{\partial \beta_2} \delta \beta_2 \right)^2} \quad (\text{Equation C9})$$

Substituting the derivative terms, the uncertainty can be obtained

$$\delta\omega = \frac{\omega}{Pt_1 - Ps_1} \sqrt{[\delta Pt_1]^2 + \left[\left(\frac{1}{\omega} \right) \delta Ptd \right]^2 + [\delta Ps_1]^2} \quad (\text{Equation C10})$$

$$\delta M = \frac{5.0}{7.0} \frac{1}{MP_s} \cdot \left(\frac{Pt}{Ps} \right)^{\left(-\frac{2.5}{3.5} \right)} \sqrt{[\delta Pt]^2 + \left[\left(\frac{Pt}{Ps} \right) \delta Ps \right]^2} \quad (\text{Equation C11})$$

$$\frac{\partial AVDR}{\partial Pt_1} = \frac{\int_0^{2 \text{ pitch}} \frac{Pt_2 M_2 \cos \beta_2}{(1 + 0.2 M_2^2)^3} dS_2 \cdot \int_0^{2 \text{ pitch}} \frac{M_1 \cos \beta_1}{(1 + 0.2 M_1^2)^3} dS_1}{- \left[\int_0^{2 \text{ pitch}} \frac{Pt_1 M_1 \cos \beta_1}{(1 + 0.2 M_1^2)^3} dS_1 \right]^2}$$

(Equation C12)

$$\frac{\partial AVDR}{\partial Pt_2} = \frac{\int_0^{2 \text{ pitch}} \frac{M_2 \cos \beta_2}{(1 + 0.2 M_2^2)^3} dS_2}{\int_0^{2 \text{ pitch}} \frac{Pt_1 M_1 \cos \beta_1}{(1 + 0.2 M_1^2)^3} dS_1}$$

(Equation C13)

$$\frac{\partial AVDR}{\partial M_1} = \frac{\int_0^{2 \text{ pitch}} \frac{Pt_2 M_2 \cos \beta_2}{(1 + 0.2 M_2^2)^3} dS_2 \cdot \int_0^{2 \text{ pitch}} \frac{Pt_1 \cos \beta_1 (1 - 3M_1 + 0.2 M_1^2)}{(1 + 0.2 M_1^2)^4} dS_1}{- \left[\int_0^{2 \text{ pitch}} \frac{Pt_1 M_1 \cos \beta_1}{(1 + 0.2 M_1^2)^3} dS_1 \right]^2}$$

(Equation C14)

$$\frac{\partial AVDR}{\partial M_2} = \frac{\int_0^{2 \text{ pitch}} \frac{Pt_2 \cos \beta_2 (1 - 3M_2 + 0.2 M_2^2)}{(1 + 0.2 M_2^2)^4} dS_2}{\int_0^{2 \text{ pitch}} \frac{Pt_1 M_1 \cos \beta_1}{(1 + 0.2 M_1^2)^3} dS_1}$$

(Equation C15)

$$\frac{\partial AVDR}{\partial \beta_1} = \frac{\int_0^{2 \text{ pitch}} \frac{Pt_2 M_2 \cos \beta_2}{(1 + 0.2 M_2^2)^3} dS_2 \cdot \int_0^{2 \text{ pitch}} \frac{Pt_1 M_1 \sin \beta_1}{(1 + 0.2 M_1^2)^3} dS_1}{\left[\int_0^{2 \text{ pitch}} \frac{Pt_1 M_1 \cos \beta_1}{(1 + 0.2 M_1^2)^3} dS_1 \right]^2}$$

(Equation C16)

$$\frac{\partial AVDR}{\partial \beta_2} = \frac{- \int_0^{2 \text{ pitch}} \frac{Pt_2 M_2 \sin \beta_2}{(1 + 0.2 M_2^2)^3} dS_2}{\int_0^{2 \text{ pitch}} \frac{Pt_1 M_1 \cos \beta_1}{(1 + 0.2 M_1^2)^3} dS_1}$$

(Equation C17)

Using the above uncertainty propagating equations, the instrument uncertainty for all the experimental data was calculated. Table C2 listed the ranges of the main parameters in this research.

Table C2 Instrumentation uncertainty range

Parameter	Uncertainty (% of value)	
	Minimum	Maximum
M ₁	0.3	0.7
M ₂	0.8	1.7
Loss (ω)	1.0	7.3
AVDR	1.1	1.4

The flow aperiodicity uncertainty is defined as the ratio of the difference between the one-passage-averaged value and the two-passage-averaged value over the two-passage-averaged value. It should be pointed out that the aperiodicity uncertainty calculation inevitably counted the inlet flow unsteadiness (due to blowdown tunnel facility) in because the traverse-measured spatial distribution of the parameter was coupled with time history of the flow. Table C3 listed the ranges of the aperiodicity uncertainty in this research. It is seen the aperiodicity uncertainty range is larger than instrument uncertainty.

Table C3 Aperiodicity uncertainty range

Parameter	Uncertainty (% of value)	
	Minimum	Maximum
M ₁	0.02	1.7
M ₂	0.07	2.6
Loss (ω)	0.4	11.0
AVDR	0.02	2.5

To quantify inlet flow unsteadiness, the variation of inlet Mach number within the traverse time was estimated, which showed the range of approximately 1.5%.

In summary, the experimental data uncertainty is found mostly from flow aperiodicity. Both aperiodicity and flow unsteadiness are random in effect. The instrument uncertainty is smaller and more consistent. However, examination of the experimental data with uncertainty shows only few data points have high uncertainty due to the two random source and they are disregarded. Therefore, a final estimation of the overall uncertainty is obtained, as shown in Table 2.

References

1. Gostelow, J. P., *Cascade Aerodynamics*, Pergamon Press, 1984.
2. Turton, R. K., *Principles of Turbomachinery*, Second Edition, Chapman & Hall, 1995.
3. Dixon, S. L., *Fluid Mechanics, Thermodynamics of Turbomachinery*, Pergamon Press, Second Edition, 1975.
4. "Aerodynamic Design of Axial-Flow Compressors", revised, NASA SP-36, 1965.
5. "Special Course on Inverse Methods for Airfoil Design for Aeronautical and Turbomachinery Applications," AGARD Report No. 780, 1990.
6. Denton, J.D., "Loss Mechanism in Turbomachines," *Journal of Turbomachinery*, Vol. 115, pp. 621-656, 1993.
7. Dunham, J., "Aerodynamic Losses in Turbomachines," AGARD-CP-571, *Loss Mechanism and Unsteady Flows in Turbomachines*, K1-K13, 1996.
8. Starken, H. and Lichtfuss, H. J., "Cascade Flow adjustment," *Modern Methods of Testing Rotating Components of Turbomachines (Instrumentation)*, AGARD-AG-207, 1975.
9. Starken, H. "Basic Fluid Dynamic Boundary Conditions of Cascade Wind Tunnels", Chapter 2 Linear cascades, *Advanced Methods for Cascade Testing*, AGARD-AG-328, pp. 11, 1993.
10. Wennerstrom, A. J., "Highly Loaded Axial Flow Compressors: History and Current Developments," *Journal of Turbomachinery*, Vol. 112, pp. 567-578, 1990.
11. Dunker, R. J., "A Shock Loss Model for Supercritical Subsonic Flows in Transonic Axial Flow Compressors," *Transonic and Supersonic Phenomena in Turbomachines*, pp. 27.1-27.15, AGARD-CP-401, 1987.
12. Carter, J. C., "Aerodynamic Performance of a Flow Controlled Compressor Stator Using an Imbedded Ejector Pump," M.S. Thesis, Virginia Polytechnic Institute and State University, 2001.
13. Olhofer, M., Arima, T., Sonoda T., and Sendhoff, B., "Optimization of a stator blade used in a transonic compressor cascade with evolution strategies," *Adaptive Computation in Design and Manufacture (ACDM)*, editor: Ian Parmee, pp. 45-54, Springer Verlag, 2000.

14. Arima, T., Sonoda, T., Shirotori, M., Tamura, A., and Kikuchi, K., "A Numerical Investigation of Transonic Axial Compressor Rotor Flow Using a Low-Reynolds Number κ - ϵ Turbulence Model," *Journal of Turbomachinery*, Vol. 121, pp. 44-58, 1999.
15. Yamaguchi, Y. and Arima, T., "Multi-Objective Optimization for the Transonic Compressor Stator Blade," 8th AIAA/USAF/NASA/ISSMO Symposium on Multidisciplinary Analysis and Optimization, Long Beach, CA, AIAA-2000-4909, 2000.
16. Benini, E., and Toffolo, A., "Development of High-Performance Airfoils for Axial Flow Compressors Using Evolutionary Computation," *Journal of Propulsion and Power*, Vol. 18, No. 3, pp. 544-554, 2002.
17. Xu, C. and Amano, R. S., "A Turbomachinery Blade Design and Optimization Procedure," ASME TURBO EXPO 2002, Amsterdam, Netherlands, GT-2002-30541, 2002.
18. Rai, M., and Madavan, N., "Application of Artificial Neural Networks to Design of Turbomachinery Airfoils," *Journal of Propulsion and Power*, Vol. 17, No. 1, pp. 176-183, 2001.
19. Yiu, K.F.C., and Zangeneh, M., "Three-Dimensional Automatic Optimization Method for Turbomachinery Blade Design," *Journal of Propulsion and Power*, Vol. 16, No. 6, pp. 1174-1181, 2000.
20. Oksuz, O., Akmandor, I., and Kavsaoglu, M., "Aerodynamic Optimization of Turbomachinery Cascades Using Euler/Boundary-Layer Coupled Genetic Algorithms," *Journal of Propulsion and Power*, Vol. 18, No. 3, pp. 652-657, 2002.
21. Manna, M. and Tuccillo, R., "Improving the Aero-Thermal Characteristics of Turbomachinery Cascades," ASME TURBO EXPO 2002, Amsterdam, Netherlands, GT-2002-30596, 2002.
22. Papila, N. and Shyy, W., "Shape Optimization of Supersonic Turbines Using Global Approximation Methods," *Journal of Propulsion and Power*, Vol. 18, No. 3, pp. 509-518, 2002.

23. Dennis, B. H., Dulikravich, G. S., and Han, Z.-X., "Optimization of Turbomachinery Airfoils with a Genetic/Sequential-Quadratic-Programming Algorithm," *Journal of Propulsion and Power*, Vol. 17, No. 5, pp. 1123-1128, 2001.
24. Catalano, L. A. and Dadone, A., "Progressive Optimization for the Inverse Design of 2D Cascades," 36th AIAA/ASME/SAE/ASEE Joint Propulsion, Huntsville, Alabama, AIAA 2000-3204, 2000.
25. Catalano, L. A. and Dadone, A., "Progressive Optimization for the Efficient Design of 3D Cascades," 15th AIAA CFD Conference, Anaheim, California, AIAA 2001-2578, 2001.
26. Shahpar, S., "A Comparative Study of Optimization Methods for Aerodynamic design of Turbomachinery Blades," ASME TURBO EXPO 2000, Munich, Germany, 2000-GT-523, 2000.
27. Manna, M. and Tuccillo, R., "The Combined Use of Navier-Stokes Solvers and Optimization Methods for Decelerating Cascade Design," ASME TURBO EXPO 2000, Munich, Germany, 2000-GT-523, 2000.
28. Lee, S.-Y. and Kim, K.-Y., "Design Optimization of Axial Flow Compressor Blades with Three-Dimensional Navier-Stokes Solver," ASME TURBO EXPO 2000, Munich, Germany, 2000-GT-0488, 2000.
29. Li, J., Tsukamoto, H., and Satofuka, N., "Optimization of Aerodynamic Design for Cascade Airfoil by Means of Boltzmann Selection Genetic Algorithms," AIAA 2000-4521, 2000.
30. Horibata, Y., "Transonic Cascade Design Using the Implicit Function Theorem," 38th Aerospace Sciences Meeting & Exhibit, Reno, Nevada, AIAA 2000-0786, 2000.
31. Medic, G., Mohammadi, B., Petruzzelli, N., Stanciu, M., and Hecht, F., "3D Optimal Shape Design for Complex Flows: Application to Turbomachinery," 37th Aerospace Sciences Meeting & Exhibit, Reno, Nevada, AIAA 99-0833, 1999.
32. Jha, R., Chattopadhyay, A., and Rajadas, J. N., "Optimization of Turbomachinery Airfoil Shape for Improved Performance," AIAA-98-1917, 1998.
33. Nerurkar, A. C., Dang, T. Q., Reddy, E. S., and Reddy, D. R., "Design Study of Turbomachinery Blades by Optimization and Inverse Techniques," 32nd

- AIAA/ASME/SAE/ASEE Joint Propulsion Conference and Exhibit, Lake Buena Vista, Florida, AIAA 96-2555, 1996.
34. Köller, U., Mönig, R., Küsters, B., and Schreiber, H., "Development of Advanced Compressor Airfoils for Heavy-Duty Gas Turbines - Part I: Design and Optimization," *Journal of Turbomachinery*, Vol. 122, pp 397-405, 2000.
 35. Küsters, B., Schreiber, H., Köller, U., and Mönig, R., "Development of Advanced Compressor Airfoils for Heavy-Duty Gas Turbines - Part II: Experimental and Theoretical Analysis," *Journal of Turbomachinery*, Vol. 122, pp. 406-415, 2000.
 36. Sonada, T., Yamaguchi, Y., Arima, T., Olhofer, M., Sendhoff, B., and Schreiber, H., "Advanced High Turning Compressor Airfoils for Low Reynolds Number Condition - Part I: Design and Optimization," ASME/IGTI Turbo Expo 2003, Atlanta, GA, GT2003-38458.
 37. Schreiber, H., Steinert, W., Sonada, T., and Arima, T., "Advanced High Turning Compressor Airfoils for Low Reynolds Number Condition - Part II: Experimental and Numerical Analysis," ASME/IGTI Turbo Expo 2003, Atlanta, GA, GT2003-38477.
 38. Weber, A., Faden, M., Starcken, H., and Jawtusch, V., "Theoretical and Experimental Analysis of a Compressor Cascade at Supercritical Flow Conditions," ASME paper 87-GT-256, 1987.
 39. Schreiber, H. A. and Starcken, H., "Experimental Cascade Analysis of a Transonic Compressor Rotor Blade Section," *Journal of Engineering for Gas Turbine and Power*, Vol. 106, pp. 288-294, 1984.
 40. Schreiber, H. A. and Starcken, H., "An Investigation of a Strong Shock-Wave Turbulent Boundary Layer Interaction in a Supersonic Compressor Cascade," *Journal of Turbomachinery*, Vol. 114, pp 494-503, 1992.
 41. Schreiber, H. A., "Experimental Investigations on Shock Losses of Transonic and Supersonic Compressor Cascades," *Transonic and Supersonic Phenomena in Turbomachines*, pp. 11.1-11.15, AGARD-CP-401, 1987.
 42. Tweedt, T. L., Schreiber, H. A., and Starcken, H., "Experimental Investigation of the Performance of a Supersonic Compressor Cascade," ASME Paper 88-GT-306, 1988.

43. Hoheisel, H. and Seyb, N. J., "The Boundary Layer Behavior of Highly Loaded Compressor Cascade at Transonic Flow Conditions," *Transonic and Supersonic Phenomena in Turbomachines*, pp. 4.1-4.17, AGARD-CP-401, 1987.
44. Katoh, Y., Hamatake, H., and kashiwabara, Y., "Investigation of The Aerodynamic Performance of a Transonic Inlet Stage of an Axial Flow Compressor," AIAA 98-3415, 1998.
45. Küsters, B. and Schreiber, H. A., "Compressor Cascade Flow with Strong Shock-Wave/Boundary-Layer Interaction," *AIAA Journal*, Vol. 36, No. 11, 1998.
46. Shamroth, S. J., McDonald, H., and Briley, W. R., "Prediction of Cascade Flow Fields Using the Averaged Navier-Stokes Equations," *Journal of Engineering for Gas Turbine and Power*, Vol. 106, pp. 383-390, 1984.
47. Calvert, W. J., "An Inviscid-Viscous Interaction Treatment to Predict the Blade-to-Blade Performance of Axial Compressors with Leading Edge Normal Shock Waves," ASME 82-GT-135, 1982.
48. König, W. M., Hennecke, D. K., and Fottner, L., "Improved Blade Profile Loss and deviation Angle Models for Advance Transonic Compressor Bladings: Part I – A Model for Subsonic Flow," *Journal of Turbomachinery*, Vol. 118, pp. 73-80, 1996.
49. König, W. M., Hennecke, D. K., and Fottner, L., "Improved Blade Profile Loss and deviation Angle Models for Advance Transonic Compressor Bladings: Part II – A Model for Supersonic Flow," *Journal of Turbomachinery*, Vol. 118, pp. 81-87, 1996.
50. Hobbs, D. E., and Weingold, H. D., "Development of Controlled Diffusion Airfoils for Multistage Compressor Application," *Journal of Engineering for Gas Turbines and Power*, Vol. 106, pp. 271-278, 1984.
51. Behlke, R.F., "The development of a Second Generation of Controlled Diffusion Airfoils for Multistage Compressors," *Journal of Turbomachinery*, Vol. 108, pp. 32-41, 1986.
52. Steinert, W., Eisenberg, B., and Starcken, H., "Design and Testing of a Controlled Diffusion Airfoil Cascade for Industrial Axial Flow Compressor Application," *Journal of Turbomachinery*, Vol. 113, pp. 583-590, 1991.

53. Steinert, W. and Starcken, H., "Off-Design Transition and Separation Behavior of a CDA Cascade," ASME Paper 94-GT-214, 1994.
54. Dunker, R., Rechter, H., Starcken, H., and Weyer, H., "Redesign and Performance Analysis of a Transonic Axial Compressor Stator and Equivalent Plane Cascades with Subsonic Controlled Diffusion Blades," *Journal of Engineering for Gas Turbines and Power*, Vol. 106, pp. 279-287, 1984.
55. Sanger, N. L., "The Use of Optimization Techniques to Design Controlled-Diffusion Compressor Blading," *Journal of Engineering for Power*, Vol. 105, pp. 256-264, 1983.
56. Sanger, N.L., and Shreeve, R. P., "Comparison of Calculated and Experimental Cascade Performance for Controlled-Diffusion Compressor Stator Blading," *Journal of Turbomachinery*, Vol. 108, pp. 42-50, 1986.
57. Elazar, Y., and Shreeve, R. P., "Viscous Flow in a Controlled Diffusion Compressor Cascade with Increasing Incidence," *Journal of Turbomachinery*, Vol. 112, pp. 256-266, 1990.
58. Shreeve, R. P., Elazar, Y., Dreon, J. W., and Baydar, A., "Wake Measurements and Loss Evaluation in a Controlled Diffusion Compressor Cascade," *Journal of Turbomachinery*, Vol. 113, pp. 591-599, 1991.
59. Douglas, J. W., "Effects of Free Stream Turbulence on Compressor Cascade Performance," M.S. Thesis, Virginia Polytechnic Institute and State University, 2001.
60. Douglas, J. W., Li, S.-M., Song, B., Ng, W. F., Sonoda, T., and Arima, T., "Effects of Freestream Turbulence on the Losses of a Highly-Loaded Compressor Stator Blade," ASME TURBO EXPO 2002, Atlanta, Georgia, GT-2003-38604, 2003.
61. Starcken, H., Fottner, L., Sieverding, C. H., Schreiber, H. A., Steinert, W., Hoorelbeke, M. M., Gaillard, and Losfeld, Chapter 2 Linear cascades, *Advanced Methods for Cascade Testing*, AGARD-AG-328, 1993.
62. Steinert, W., Fuchs, R. and Starcken, H., "Inlet Flow Angle Determination of Transonic Compressor Cascades," *Journal of Turbomachinery*, Vol. 114, pp. 487-493, 1992.

63. Deutsch, S. and Zierke, W. C., "The Measurement of Boundary Layers on a Compressor Blade in Cascade: Part 1-A Unique Experimental Facility," *Journal of Turbomachinery*, Vol. 109, pp.520-526, 1987.
64. Lepicovskey, J., Chima, R. V., McFarland, E. R. and Wood, J. R., "On Flowfield Periodicity in the NASA Transonic Flutter Cascade," *Journal of Turbomachinery*, Vol. 123, pp.501-509, 2001.
65. Song, B., Gui, X., Li, S.-M., Douglas, J., and Ng, W., "Flow periodicity improvement in a High Speed Compressor Cascade with a Large Turning-Angle," 38th AIAA/ASME/SAE/ASEE Joint Propulsion Conference & Exhibit, Indianapolis, Indiana, AIAA 2002-3539, 2002.
66. Goldstein, R. J., *Fluid Mechanics Measurements*, second edition, Taylor & Francis, 1996.
67. Merzkirch, W., *Techniques of Flow Visualization*, AGARD-AG-302, 1987.
68. Hall, E. J., Heidegger, N. J., and Delaney, R. A., *ADPAC v1.0 – User's Manual*, NASA/CR-1999-206600, February, 1999.
69. *Gridgen User Manual*, Version 13.3, Pointwise, Inc., 1999.
70. *FIELDVIEW for Windows User's guide*, version 8.0, Intelligent Light, 2001.
71. *FIELDVIEW for Windows Reference Manual*, version 8.0, Intelligent Light, 2001.
72. Schlichting, H., *Boundary-Layer Theory*, translated by Kestin, J., Six Edition, McGraw-Hill, 1968.
73. Baldwin, B. S. and Lomax, H., "Thin Layer Approximation and Algebraic Model for Separated Turbulent Flows," AIAA 16th Aerospace Sciences Meeting, Huntsville, AL, AIAA-78-257, 1978.
74. Spalart, P. R. and Allmaras, S. R., "A One-Equation Turbulence Model for Aerodynamic Flows," AIAA 30th Aerospace Sciences Meeting & Exhibit, Reno, NV, AIAA-92-0439, 1992.
75. Goldberg, U. C., "Towards a Pointwise Turbulence Model for Wall-Bounded and Free Shear Flows," *Boundary Layer and Free Shear Flows*, ASME FED-Vol. 184, pp. 113-118, 1994.
76. Stitzel, S., Personal Communication, Blacksburg, VA, 2002.

77. Cumpsty, N.A., *Compressor aerodynamics*, Longman Scientific & Technical, 1989.
78. Kunz, R. F. and Lakshminarayana, B., "Explicit Navier-Stokes Computation of Cascade Flows Using the κ - ϵ Turbulence Model," *AIAA Journal*, Vol. 30, No. 1, pp. 13-22, 1992.
79. Pollard, D. and Gostelow, J. P., "Some Experiments at Low Speed on Compressor Cascades," *ASME Journal of Engineering for Power*, Vol. 89, pp. 427-436, 1967.
80. Fottner, L., "Analytical Approach for the Loss and Deflection Behavior of Cascades in Transonic Flow Including Axial Mass Flow Variation," AGARG-AG-164, Paper I-7, pp. 119-139, 1972.
81. Stark, U., "The Effect of Axial Velocity Density Ratio on the Aerodynamic Coefficients of a Compressor Cascade in Viscous Flow," AGARG-AG-164, Paper I-12, pp. 205-220, 1972.
82. Heilmann, W., "The Influence of Axial Velocity Density Ratio on Compressor Cascade Performance in Compressible Flow," AGARG-AG-164, Paper I-13, pp. 221-240, 1972.
83. Starcken, H., Breugelmans, F. A. E., and Schimming, P., "Investigation of the Axial Velocity Density Ratio in a High Turning Cascade," ASME Paper 75-GT-25, 1975.
84. Stark, U. and Hoheisel, H., "The Combined Effect of Axial Velocity Density Ratio and Aspect Ratio on Compressor Cascade Performance," *ASME Journal of Engineering for Power*, Vol. 103, pp. 247-255, 1981.
85. Weingold, H. D. and Behlke, R. F., "The Use of Surface Static Pressure Data as a Diagnostic Tool in Multistage Compressor Development," *Journal of Turbomachinery*, Vol. 109, pp. 123-129, 1987.
86. Schreiber, H. A., Steinert, W., and Küsters, B. "Effects of Reynolds Number and Free-Stream Turbulence on Boundary Layer Transition in a Compressor Cascade," *Journal of Turbomachinery*, Vol. 124, pp. 1-9, 2002.
87. Sonada, T. and Arima, T., Personal Communication, 2002, 2003.
88. Weber, A., Schreiber, H. A., Fuchs, R., and Steinert, W., "3-D Transonic Flow in a Compressor Cascade With Shock-Induced Corner Stall," *Journal of Turbomachinery*, Vol. 124, pp 358-366, 2002. (Also published: 2001-GT-345)

89. Cyrus, V., "The Effect of the Reynolds Number on the Three-Dimensional Flow in a straight Compressor Cascade," ASME 88-GT-269, 1988.
90. Weingold, H. D. and Behlke, R. F., "The Use of Surface Static Pressure Data as a Diagnostic Tool in Multistage Compressor Development," *Journal of Turbomachinery*, Vol. 109, pp. 123-129, 1987.
91. Steinert, W., Fuchs, R. and Starcken, H. " Inlet Flow Angle Determination of Transonic Compressor Cascades," *Journal of Turbomachinery*, Vol. 114, pp. 487-493, 1992.
92. Jouini, D. B. M. and Sjolander, S. A., Moustapha, S. H., "Midspan Flow-Field Measurements for Two Transonic Linear Turbine Cascades at Off-Design Conditions," Proceedings of ASME Turbo Expo 2001, New Orleans, USA, 2001-GT-0493.

Vita

Bo Song

Bo Song was born in Zigong, Sichuan Province, China on June 26, 1970. He grew up and attended Shuguang High School in his hometown. In 1988, he entered Beijing University of Aeronautics and Astronautics (BUAA), where he received his Bachelor of Science and Master of Science in Thermal Power Engineering in 1992 and 1995 respectively, from the Department of Power Engineering. Upon completion of his Master's degree, he worked as an assistant professor for four years in the same department of BUAA, conducting research and teaching in the field of thermal/fluid science and turbine engine technology, with the focus on combustor/combustion technology. In 1999, he went to Virginia Tech pursuing his Ph.D. in Mechanical Engineering under the guidance of Prof. Wing F. Ng. There he undertook research as a Graduate Research Assistant and later as a Research Associate in the same field, with his focus shifting to turbomachinery. The author defended his Ph.D. work in November 2003. Upon graduation, he will continue his research in the same field at the Mechanical Engineering Department of Virginia Tech as a Postdoctoral Research Scientist.